Density Functional Theory Studies on Zeolite Encapsulated Transition Metal Complexes

A Thesis submitted to Bharathidasan University

for the award of the Degree of

Doctor of Philosophy

by

S. TAMILMANI

Research Supervisors:

Prof. R. Renganathan

Prof. S. Arumugam

School of Chemistry

Bharathidasan University

Tiruchirappalli – 620 024

October 2018

BHARATHIDASAN UNIVERSITY
School of Chemistry
Tiruchirappalli – 620 024
Tamil Nadu, India

Dr. R.Renganathan
UGC-Emeritus Fellow

Date:

CERTIFICATE

This is certify that the thesis entitled **"Density Functional Theory Studies on Zeolite Encapsulated Transition Metal Complexes"** submitted by Ms. S.Tamilmani is a bonafide record of research work done by her under my guidance in the School of Chemistry, Bharathidasan University, Tiruchirappalli-620 024, India and it has not previously formed the basis for the award of any degree, diploma, associateship, fellowship or other similar title of Bharathidasan University or any other university.

(S.ARUMUGAM)
Co-Guide

(R.RENGANATHAN)
Research Supervisor

BHARATHIDASAN UNIVERSITY
School of Chemistry
Tiruchirappallli – 620 024
Tamil Nadu, India

S. Tamilmani
Research Scholar

Date:

DECLARATION

I hereby declare that the thesis entitled **"Density Functional Theory Studies on Zeolite Encapsulated Transition Metal Complexes"** has been originally carried out by me at School of Chemistry, Tiruchirappalli-620 024, India under the guidance of **Prof. R. Renganathan**, UGC-Emeritus Fellow, School of Chemistry, Bharathidasan University, Tiruchirappalli-620 024, India. This work has not previously formed the basis for the award of any degree, diploma, associateship, fellowship or other similar title of Bharathidasan University or any other university.

(S.TAMILMANI)

ACKNOWLEDGEMENT

I sincerely express my grateful thanks to my guide **Dr. R. Renganathan**, UGC-Emeritus Fellow, School of Chemistry, Bharathidasan University, Tiruchirappalli, for his guidance and continuous encouragement throughout my research period. His mentorship provided me with the perfect balance of research independence and support. I would like to acknowledge the efforts taken and moral support rendered during this research tenure.

I owe my grateful thanks to my beloved supervisor **Prof. B. Viswanathan**, National Centre for Catalysis Research (NCCR), IIT Madras, Chennai-36, who was a source of inspiration and ceaseless encouragement to me during every stage of my work. His inspiring guidance, understanding, novel ideas, constructive suggestions and patience made the completion of this work possible.

It is a great pleasure to express my heartfelt thanks to my Co-guide, **Dr. S. Arumugam,** Professor, Centre for High Pressure Research, School of Physics, Bharathidasan University, for his productive criticism, endless support and encouragement throughout my research work.

My heartfelt thanks to all the faculty members in the school of chemistry, for their help to widen my knowledge in Science.

I am always thankful to my lab mates, for their timely help and their friendship during my research.

I thank all the non-teaching staff of our department who offered their help whenever needed.

I am thankful to the Department of Science & Technology, Government of India, New Delhi, for setting up NCCR. NCCR allowed me to carry out the research work by extending all infrastructure facilities. I take this opportunity to acknowledge HPCE, IIT-Madras for providing computational facilities.

I have a great pleasure to express my wholehearted thanks to my parents for sacrificing their lives to give me a good education, constant motivation and being a great source of inspiration. They are the driving force that pushed me to better myself as a person.

Above all, I thank the **LORD ALMIGHTY** for giving me the courage, strength and patience to complete this work successfully.

S.TAMILMANI

CONTENTS

ABBREVIATIONS

SBU	Secondary Building Units
FAU	Faujasite
LTL	Linde type L
1D	one-dimensional
CAN	Cancrinite cage
D6R	Double hexagonal Ring
MCM-22	Mobil Composition of Matter No. 22
MWW	M-tWenty-tWo type Framework
10R	10-membered ring
ZSM-5	Zeolite Socony Mobil–5
H_2O_2	Hydrogen Peroxide
TBHP	t-Butylhydroperoxide
SEM	Scanning Electron Microscopy
XRD	X-Ray Diffraction
FTIR	Fourier Transform Infrared
UV−Vis	Ultraviolet and Visible
ESR	Electron Spin Resonance
DFT	Density Functional Theory
TD-DFT	Time Dependent Density Functional Theory
C-PCM	Conductor-like Polarizable Continuum Model
HOMO	Highest Occupied Molecular Orbital
LUMO	Lowest Unoccupied Molecular Orbital
HF	Hartree-Fock
E_{xc}	Exchange-Correlation Functional
LDA	Local Density Approximation
GGA	Generalized Gradient Approximation

MGGA	Meta Generalized Gradient Approximation
STOs	Slater Type Orbitals
GTOs	Gaussian Type Orbitals
FMO	Frontier Molecular Orbital
NBO	Natural Bond Orbital
NPA	Natural Population Analysis
NHOs	Natural Hybrid Orbitals
NAOs	Natural Atomic Orbitals
NLMOs	Natural Localized Molecular Orbitals
NOs	Natural Orbitals
MOs	Molecular Orbitals
NMB	Natural Minimal Basis
B3LYP	Becke-3-Lee-Yang-Parr
LANL2DZ	Los Alamos National Laboratory 2-Double-Z
IP	Ionization Potential
EA	Electron Affinity
FFs	Fukui Functions
LMCT	Ligand-to-Metal Charge Transfer
MPc	Metallophthalocyanine
DMF	N,N-Dimethylformamide
DMSO	Dimethylsulphoxide
MHP	Maximum Hardness Principle
HPA	Hirschfeld Population Analysis
Bzl	Benzimidazole
2-EtBzl	2-Ethylbenzimidazole

1. Introduction

1.0 Abstract

Zeolites and their structures are briefly discussed, followed by illustrations of some general concepts in computational chemistry. The scope of the present investigation is described at the end of this chapter.

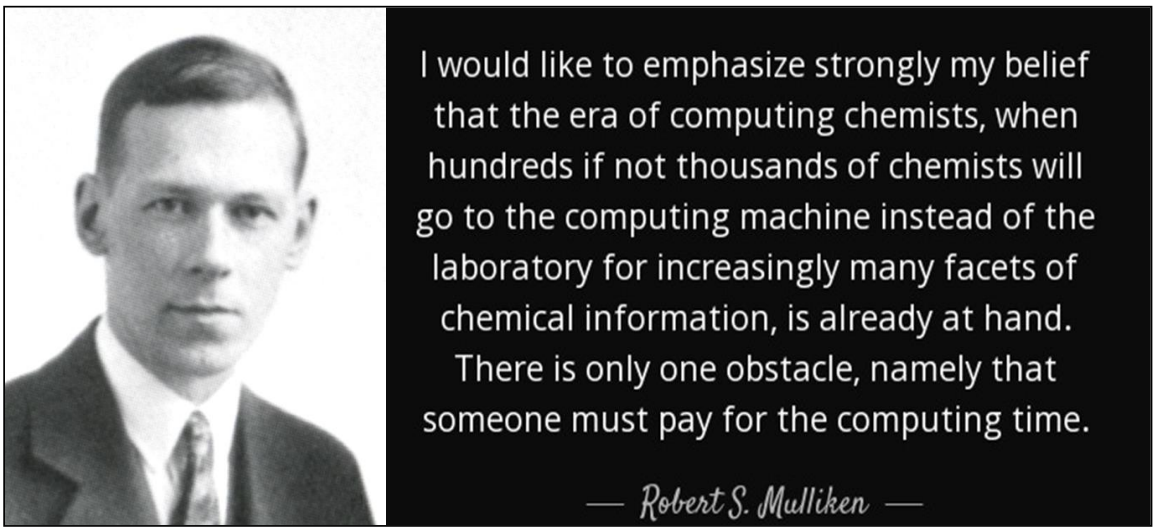

-Robert S. Mulliken,
(Nobel prize in Chemistry, 1966)

1.1 Catalysis

Catalysis is one of the key technologies for speeding up the challenges regarding limited resources, growing population and environmental problems for the future developments. Essential features for the successful application of catalysts are activity, selectivity and recycling ability. Catalysis is a kinetic phenomenon which increases the rate of reactions. It involves in the many fields such as chemical kinetics, thermodynamics, solid state physics, organic chemistry, surface chemistry, ceramics and metallurgy. As more and more catalysts and catalytic processes are available, the emphasis of research in this field has shifted to achieve more selectivity.

Catalytic processes have the capability of utilization of the raw materials and give more product selectivity. These processes produce lesser inorganic effluents which are easier to dispose of, unlike the stoichiometric oxidations which produce larger inorganic effluents. Chemical industries are forced to adopt exhaust catalysts due to the concerns of environmental problems. There are three different fields of catalysis: homogeneous, heterogeneous and biological (enzymatic) catalysis. These three areas have been generally developed as virtually separate disciplines with research in one area having little apparent relevance to that in the other two. As a result, greater emphasis must be placed on the development of new and improved catalytic processes.

Nearly 90% of the products manufactured today require processes with at least one catalytic step. As chemical processes always hold a potential threat to the environment, the nature of the catalyst used assumes special importance in relation to environmental protection. Metal complexes play a vital role as homogeneous catalysts for various reactions. The search for efficient catalytic processes having high activity and selectivity is of great importance. The need for environmental protection has added a new dimension to the search for new catalysts which are regenerable and safe.

1.2 Transition Metal Complexes

Transition metal complexes are good catalysts for many reactions including oxidation. However, they have certain disadvantages because of their homogeneous nature. In organic chemistry, metal complexes are used as the catalyst for the selective oxidation reactions to transform the functional groups. Oxidation reactions convert the primary oxo product into secondary products like acids, diols, amines or esters which are the preferred processes in chemical synthesis.[1,2] By selecting the appropriate catalyst and reaction conditions, it is possible to direct the reaction along one selected pathway (lower energy pathway) to obtain the desired product. The existence of

different oxidation states of transition metals makes them excellent catalysts for many reactions.[3,4]

1.3 Homogeneous Catalysis by Metal Complexes

The most impressive examples of catalysts can be found in the area of homogeneous catalysis by metal complexes. An important role in catalysis by the metal complex is played by elementary reactions such as an oxidative addition of reactants, reductive elimination of products, as well as by numerous but well-classified rearrangements of atom and chemical bonds in the coordination sphere of metal atoms. Thus all reactions catalyzed by metal complexes proceed through a sequence of some simple transformation catalyzed by metal complexes and is associated with the changes in oxidation state of the central metal atom, its coordination number and the nature of the ligands surroundings.[5]

Homogeneous catalysis is attractive and it is performed under mild conditions. These reactions give desired products with higher selectivity. It creates problem while coming to the large-scale industrial processes due to the difficulties in the catalyst separation from the reaction medium, the possible corrosive effect of catalyst solutions and instability of homogeneous catalytic systems. The instability and low thermal characteristics of such systems lead to slow decomposition. Due to this recycling ability and process lacking technology, it has limited commercial applications in bulk preparation. Product contamination occurs when the catalyst is not separated from the product and also causes loss of catalysts. The cost of catalyst separation is high. Even though it has advantages due to the above problems, it could not be used on an industrial scale. These problems also restrict the usage of metal complexes as catalyst in spite of their highly selective nature.

Technological point of view, the application of heterogeneous catalyst is more practical. Heterogeneous catalysts prove to be insufficiently selective and active for many processes for which effective homogeneous systems exist. They often possess high stability and are therefore easily recoverable from the reaction medium. Most of these processes are energy consuming as they require high temperature and often high pressure. To design more efficient catalysts, chemists have to develop a hybrid or heterogenized homogenous systems which combines the advantages of both the homogeneous and heterogeneous systems. This leads to the higher chemical and thermal stabilities. The separation of catalyst from the support becomes easier when compared to their homogeneous counterparts.

1.4 Heterogenisation of Homogeneous Systems

The heterogenisation of the homogeneous system refers the immobilization on or anchoring of transition metal complex to the inorganic support. It combines the advantages of both homogeneous and heterogeneous systems and also minimizes the demerits. It can be achieved by immobilization of metal complexes on various inorganic and organic supports such as silica, alumina, zeolites, MOFs and clays. These supports have the ability to alter the catalyst structure to increase the selectivity and activity.

1.5 Zeolites

Zeolite was discovered by Swedish scientist Axel Frederick Cronstedt. When he heated the new mineral, gas bubbles were released and he named it as zeolite (meaning boiling stone). The zeolites have intracrystalline space. These spaces are occupied by water molecules which can be removed by heating. These are microporous crystalline solids with well-defined pore structures. It is composed of SiO_4 and AlO_4 tetrahedral units shared by oxygen between two tetrahedral units. To balance negative charges in

the framework caused by the presence of AlO_4^{-1} units some cations are loosely bound inside the cavity in the framework. Zeolites are thus a class of crystalline aluminosilicates containing silica and alumina tetrahedra joined through oxygen bridges.

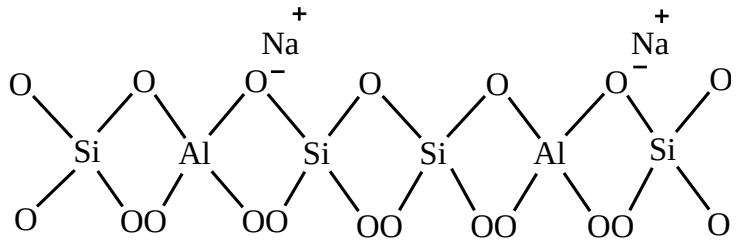

Figure 1.1 Schematic representations of SiO_4 and AlO_4 tetrahedra units in zeolites

Zeolites exist in nature and have been known since almost 250 years as aluminosilicate minerals. Most common examples are clinoptilolite, faujasite, mordenite, ferrierite and chabazite. Today most of zeolites are of great importance in many fields. These aluminosilicate minerals have been used as heterogeneous catalysts for their four main properties.

1. They have exchangeable cations allowing the introduction of cations with various catalytic properties.
2. If these cationic sites are exchanged to H^+, a large number of very strong acid sites are created.
3. Their pore diameters are less than 10Å. They have pores with one or more discrete sizes. Zeolites have porous crystal structures made up of channels and cages.
4. They have large surface area resulting in large number of catalytic sites.

Zeolites can accommodate as many as 100 times more molecules than the equivalent amount of amorphous catalyst. Zeolites are strong acid catalysts due to a large proportion of Bronsted acid sites scattered throughout their porous structure. Since they are solids, they can be easily removed from products and therefore they are

environmentally benign. Their molecular sieve action can be exploited to control the molecules which have access to or can depart from active sites.

1.5.1 Structural Features of Zeolite

Zeolite comprises of three-dimensional crystal networks of Si and Al ion present in the form of SiO_4 and AlO_4^{-1} tetrahedra. The silica and alumina tetrahedra which constitute the basic building units of zeolites can be arranged in different ways to form different porous crystal structures. In zeolites, twenty-four tetrahedra constitute a sodalite unit, which is a three dimensional array of SiO_4 and AlO_4 tetrahedra in the form of a truncated octahedron with 24 vertices and six four-membered rings and eight six-membered rings. The basic building units of sodalite have an internal diameter of 6.6 Å and the enclosed void space is called sodalite cage. These units are connected by hexagonal prisms constituting a larger void space called supercage. The cavity of the sodalite unit is known as the β-cage while the cavity of the supercage is the α-cage. These sodalite units are the basic building blocks for A, X and Y type zeolites. When the sodalite units are linked to one another at their hexagonal faces through hexagonal prisms of six oxygen atoms, the X and Y zeolite structures are formed. This structure has two types of pores or cavities in it. The sodalite cages enclose a supercage or α-cage with diameter 13 Å and a cage mouth opening of ~ 8Å. Because of these large spatially accessible pores, the X and Y type zeolites are suitable candidates for encapsulating transition metal complexes.

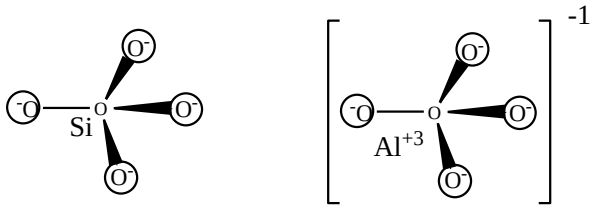

Silica Tetrahedron Alumina Tetrahedron

Figure 1.2 Schematic representations of silica and alumina tetrahedra

The primary building unit of zeolite structure is the individual tetrahedral building units (TO_4), where the central tetrahedrally bonded T atoms are usually either Si or Al; these are surrounded by four oxygen atoms. Linking these tetrahedral building units in certain ways will produce infinite framework structures of zeolites. Secondary building units (SBU) which are a combination of tetrahedrons are used to describe to zeolite infinite framework structures.

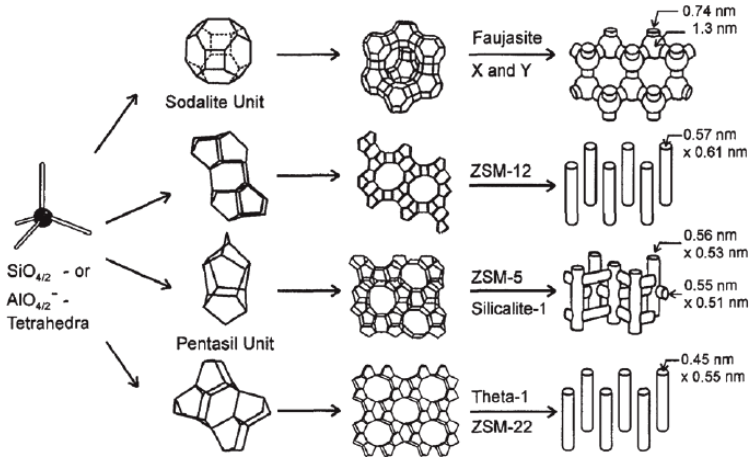

Figure 1.3 SiO_4 and AlO_4 building blocks of zeolites

Only one type of SBU used to make the zeolite framework. But few zeolites are made up of the combination of different SBUs. These SBU units can be used to describe all of the known zeolite structures. These secondary building units consist of 4, 6 and 8-membered single rings, 4-4, 6-6 and 8-8 member double rings, and 4-1, 5-1 and 4-4-1 branched rings etc. The topologies of these units are shown in Figure 1.4.

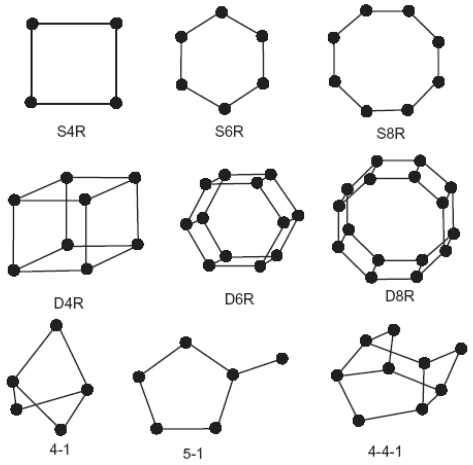

Figure 1.4 Secondary building units (SBU) found in zeolite structures

1.5.2 Classification of Zeolites

According to the morphology, crystal structure, chemical composition, effective pore diameter [6-13] and natural zeolites have been classified. Based on the morphology Bragg classified the zeolite which was further modified by Meier and Barrer. This classification was done by the secondary building units. According to their chemical composition zeolites classification has been made on the ratio of silica to alumina. From low silica zeolites to high silica zeolites, the thermal stability increases from 700 ºC to 1300 ºC.

Table 1.1 Classification of zeolites according to the chemical composition

Class	Si/Al ratio	Examples
Low silica zeolites	1-1.5	A, X
Intermediate silica zeolites	2-5	(a) Natural zeolites: erionite, chabazite, clinoptilite and mordanite. (b) L,Y, omega, large pore mordenite.
High silica zeolites	10-several thousands	(a) By direct synthesis: ZSM-4, ZSM-11, EU- 1, EU-2, Beta. (b) By thermo chemical framework modification: mordanite, erionite, highly silicious variant of Y.
Silica molecular sieves	Several thousand - ∞	Silicate

During the period 1930-1932 Mc. Bain in his studies on zeolites observed their capacity to absorb small molecules from large ones, just like a sieve. So it has been named as 'molecular sieves'. Due to microporous and crystalline nature, this sieving activity is possible. To absorb the species, the internal structure of zeolites has been modified. Two types of pore structures are available in zeolites framework. One of them provides an internal pore system comprised of interconnected cage-like voids, e.g. Zeolite –A and Zeolite –Y. The other one provides a three-dimensional system of uniform channels, e.g. ZSM-5 has a set of straight parallel pores as in ZSM-22. The zeolites are classified according to their pore sizes. Zeolites can be classified into small pore (pore size < 5Å, 8- membered ring), medium pore (pore size 5-6Å, 10- membered ring), and large pore (pore size 7-8Å, 12- membered ring) zeolites.[14] Some typical zeolites are listed in Table 1.2.

Table 1.2 Classification of zeolites according to the pore openings

Pore size	**Code**	**Abbreviated name**	**Pore diameter (Å)**
Small	LTA	Zeolite A	4.1
Medium	MFI	ZSM-5	5.3x5.6
	MEL	ZSM-11	5.3x5.6
	MTT	ZSM-33	4.5x5.2
	EUO	EU-1	4.1x5.7
	AEL	$AlPO_4$-11	3.9x6.3
Large	MOR	Mordenite	6.5x7.0
	BEA	Zeolite-β	7.6x6.4
	AFI	$AlPO_4$-5	7.3
	EMT	Hexagonal faujasite	7.4x6.4
	FAU	Zeolite X or Y	7.4

For encapsulating a metal complex within the cage of a zeolite, the zeolite must possess an optimum cage size. Due to this reason, only some of the zeolites can function as supports for metal complexes.

1.5.3 Zeolite-Y

Zeolite Y is one of the important zeolites in heterogeneous catalysis and belongs to the faujasite type of zeolites. It is spacious and consists of supercages. It is formed by 12 TO_4 tetrahedra connected tetrahedrally with four neighboring cages. It is formed by joining of the hexagonal six-membered faces of the sodalite units. The diameter of α-cage and β-cage are approximately 13Å and 6.6Å respectively. All these structural aspects have resulted in an interesting behavior of zeolite-Y which includes high catalytic activity, ion exchange capacity, shape selectivity, specific adsorption behavior and good flexibility.

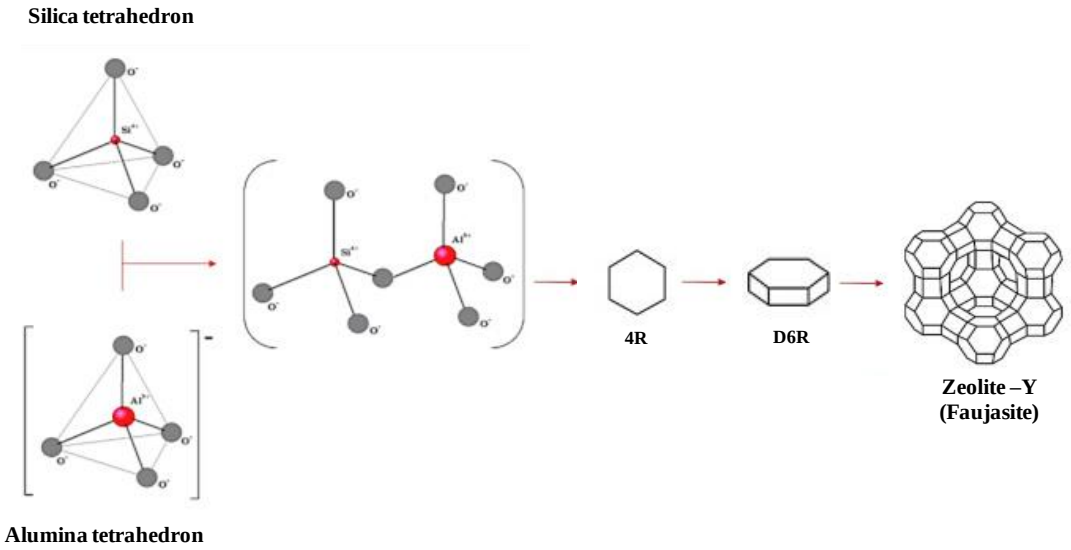

Figure 1.5 Construction of Zeolite -Y

A large-pore zeolite such as zeolite-Y whose structure consists of supercages interconnected tetrahedrally through smaller apertures of 7.4Å in diameter. Zeolite comprises a three-dimensional crystal network of Si and Al atoms, which are present in the form of SiO_4 and AlO_4^{-1} tetrahedra. Tetrahedrons join together by shared oxygen atoms with various regular arrangements, to form hundreds of different three-dimensional crystal frameworks.[15,16] The framework structure encloses cavities containing pores of molecular dimensions.

Zeolite-Y has a faujasite-type framework structure, with three different cavities of cages which are the large supercage, the sodalite cage and the double 6-ring. The structural formula can be expressed as $M_{x/n}\{(Al_2O_3)_x(SO_2)_y\}.wH_2O$, where M is the cation of the valence of n, w is the number of water molecules. Depends upon the structure, y/x (Si/Al) ratio will be 1-5. The sum $\{(Al_2O_3)_x(SiO_2)_y\}$ represents framework composition.

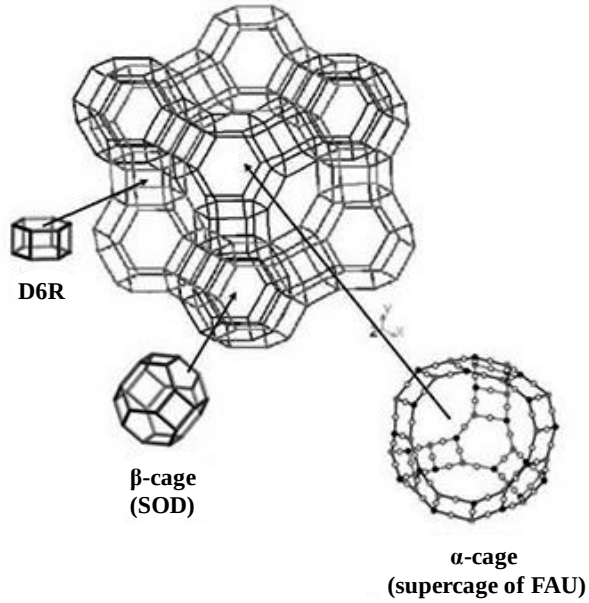

Figure 1.6 Schematic representation of the cage system of zeolite-Y

1.5.4 LTL Zeolite

Breck and Flanigen synthesized the first Linde type L framework (LTL) and Barrer and Marshall noted that to be a "large-pore" zeolite by the structure analysis and showed it has 12-ring channels and the natural mineral perlialite was later shown to be isostructural with LTL.[17-19]

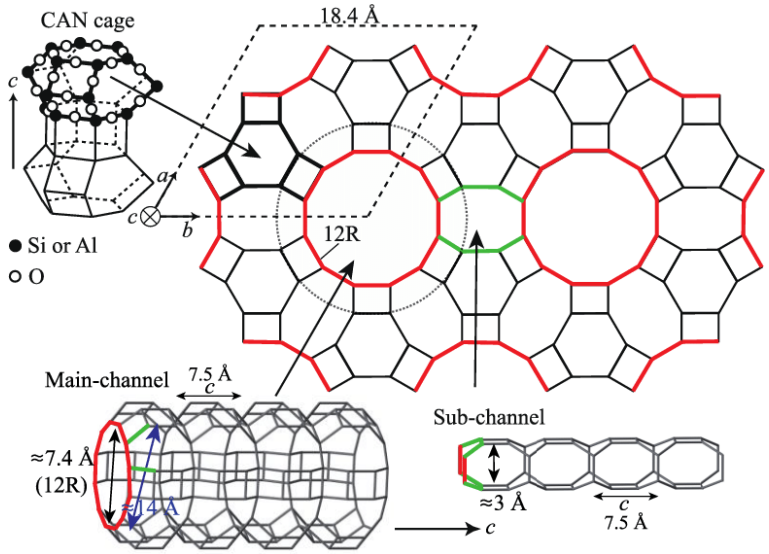

Figure 1.7 Schematic representation of the cage system of LTL zeolite

Zeolite LTL has a one-dimensional (1D) channel with 12-ring undulating channels. The structure contains two important secondary building units of cancrinite (CAN) cage and double hexagonal ring (D6R), alternating to form a column. The columnar structure can be considered to form from CAN cages fusing, giving a D6R between the CAN cages or more complex growth mechanisms involving D6R and subunits of a CAN structure.

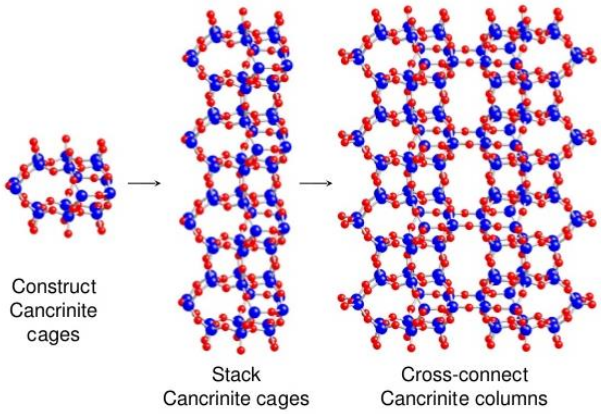

Figure 1.8 Construction of LTL zeolite model

1.5.5. MCM-22 Zeolite

MCM-22 (Mobil Composition of Matter No. 22) belongs to MWW (M-tWenty-tWo) type Framework. It is a mesoporous material from silicate and alumosilicate family with a hierarchical structure. It can be used as catalysts or catalysts support and first developed by researchers at Mobil Oil Corporation.[20] To produce selective bulk petrochemicals (e.g., alkylation reactions) in industries MCM-22 has been used. In its silicate framework, there are two independent pore systems, one of which can be defined as an intersecting sinusoidal channel system extending in two dimensions, whereas the other consists of a large supercage with an inner diameter of ~7.1 Å and height of ~18.2 Å. Both pores are accessible through 10-membered ring (10R) openings.

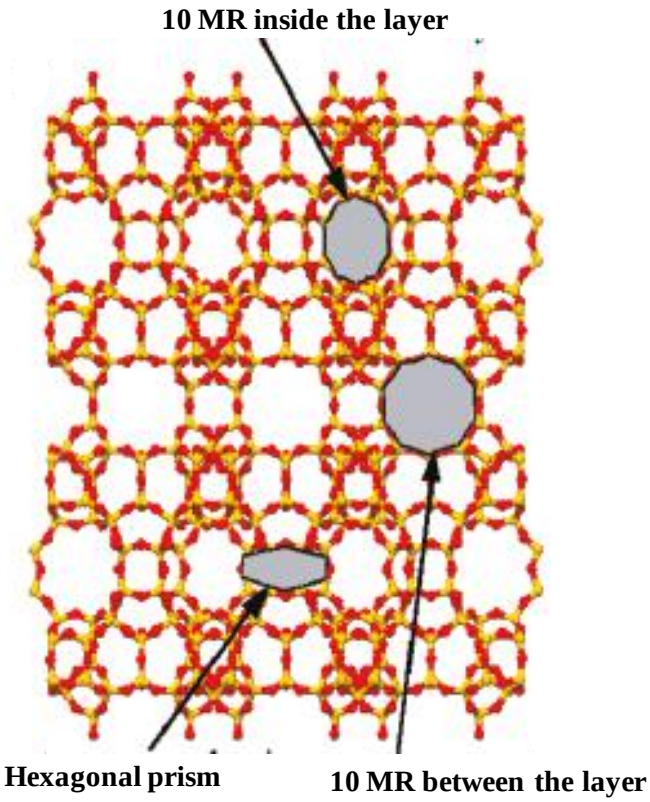

Figure 1.9 Schematic representation of MWW-type zeolite MCM-22

1.5.6 ZSM-5 Zeolite

ZSM-5, Zeolite Socony Mobil–5 (framework type MFI from ZSM-5), is an aluminosilicate zeolite belonging to the pentasil family of zeolites. Its chemical formula is $Na_nAl_nSi_{96-n}O_{192}\cdot 16H_2O$ ($0<n<27$). It is used as catalysts for hydrocarbon isomerization reactions.

ZSM-5 is composed of pentasil chains which are made up of several pentasil units (consists of eight five-membered rings) and linked together by oxygen bridges. Corrugated sheets with 10-ring holes were formed by pentasil chains. To form a structure all the corrugated sheet is connected by oxygen bridges.[21] An inversion point relates the adjacent layers of the sheets. The estimated pore size of the channel running parallel with the corrugations is 5.4 – 5.6 Å.[22] The crystallographic unit cell of ZSM-5 has 96 T sites (Si or Al), 192 O sites, and a number of compensating cations depending on the Si/Al ratio, which ranges from 12 to infinity.

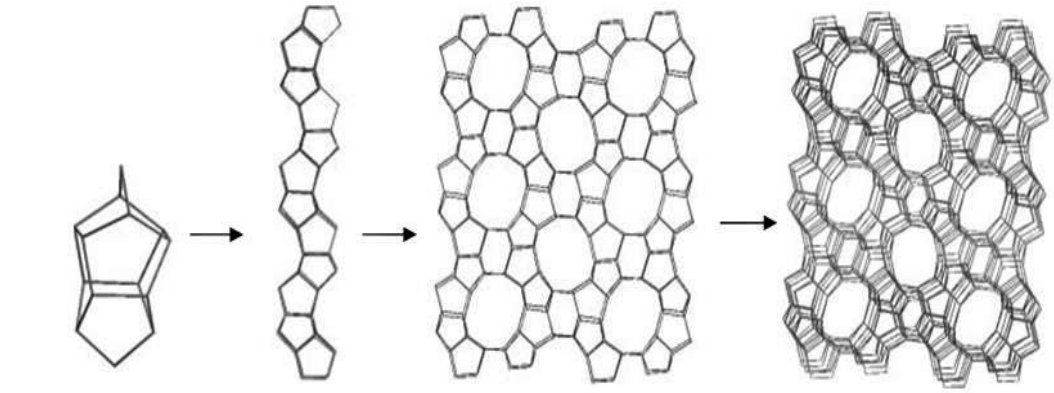

Figure 1.10 Construction of ZSM-5

1.6 Catalysis by Zeolite

Zeolites are viewed as the “philosopher’s stone” of modern chemistry. They are widely applied as solid acid catalysts in oil refining and petrochemical manufacture.

Their use avoids the effluent handling problems associated with conventional mineral acids such as aluminium chloride, for example, in the alkylation of aromatic hydrocarbons. Moreover, crystalline zeolites require mild reaction conditions and hence use of these catalysts leads to lower capital investment and increased flexibility in industrial applications. Zeolites, as well as the metal-exchanged zeolites are used on a vast scale for separation of gases, for softening hard water and as a catalyst in the petroleum and chemical industry. The most important use is in shape selective catalysis.[23-25] Shape selective property of zeolites has been used in isomerization and alkylation reactions. Zeolite X, Y and mordenite are used for the synthesis of several organic compounds.[26-29] Zeolites are also employed for carrying out certain nucleophilic substitution reactions of aliphatic compounds. Acetalisation, ester formation, trans-esterification are also catalyzed by acid zeolites.[30] Aromatics such as toluene, phenol and hetero aromatics can be acylated using carboxylic acids, acid anhydride or acid chloride.

Several addition and elimination reactions such as dehydration of alcohols, ethers and hydration of olefins are carried out using zeolites. Transition metal incorporation via ion exchange is known to influence the acidity of zeolite. These metal exchanged zeolites catalyze certain important reactions. Another application of zeolites is in the light-induced electron transfer mechanisms to mimic artificial photosynthesis.[31] Several studies to understand the influence of cation size in rearrangement and disproportionation of alkyl-dibenzyl ketones had been carried out. The selectivity of products in these cases was influenced by both the zeolite structure and the nature of cation present. Zeolites are also employed as phosphate substituent in detergents and as absorbents for the separation and purification of substances. New potential application of zeolites is in semiconductor, optical sensor technology and optical storage devices.[32,33]

Zeolites have been used for the several potential applications. Improvement of an existing process can be achieved by a simple exchange of conventional catalysts. By using zeolites, commercially viable reactions can be introduced in the industry which has been unsuccessful previously owing to insufficient activity, selectivity and catalyst life. Another potential application is heterogenisation i.e., immobilization of homogeneous catalyst to avoid separation problem. Thus zeolites stand for clean chemistry and for protection of our environment.

Zeolites are used in acid catalyzed reactions such as alkylation and acylation. Mostly faujasite, ZSM-5 and mordenite type zeolites are used as catalysts. Zeolites also find wide applications in fine chemical synthesis. Zeolites are widely accepted as shape-selective catalysts.[34] As acidic, basic, or redox catalysts, zeolites essentially act in a way similar to their homogeneous counterparts. However, because of their specific nature, these solid materials sometimes show a behavior not observed in the homogeneous phase due to shape selectivity. In zeolites, most of the active sites are located in the well-defined and molecularly sized pores and cages. Throughout a reaction, the transforming molecules are continuously exposed to steric limitations imposed by the zeolite structure, possibly changing the course of the reaction and finally resulting in product distributions showing deviations from those obtained in the homogeneous phase. In this context, molecular shape selectivity can be described as the restrictions imposed on guest molecules by size and shape of the zeolite pores.

Activity, selectivity and stability are the primary requirements of an industrial catalyst, which are met remarkably by zeolites. The nature and degree of exchange of the cation, the silica-alumina ratio, the size of reactant and product molecules are some of the main factors, which determine the catalytic activity of zeolites. The supercages in the zeolite are lager enough to accommodate most hydrocarbon molecules. The

channels interconnecting the supercages provide the molecular sieving action of zeolites.

1.6.1 Synthesis of Zeolite Encapsulated Transition Metal Complexes

The well-defined cages and channels of zeolite with the reactivity of metal complex make these molecular sieves particularly attractive as active solid supports. The distinct advantage of zeolite over conventional support materials is that a metal complex can be physically trapped in the pores and not necessarily bound to the oxide surface. Another advantage of zeolites is the high thermal stability and large internal surface area and potential to impose size and shape selectivity on the product distribution due to the molecular sieving effect.

The polyhedral cavities in zeolite-Y inscribe a cavity of substantial dimensions that they could be able to hold clusters of small molecules in addition to the appropriate number of exchangeable cations. Proper choice of complex molecule of correct size that fit securely within the supercages of zeolite-Y ensures that the molecule cannot escape through the ring opening of the supercage. A wide variety of metal clusters, organometallic compounds and coordination compounds have been encapsulated in a range of different hosts. Such immobilization of known homogeneous complexes on solid supports would combine the advantages of both homogeneous and heterogeneous catalysts while minimizing the disadvantages of both. Enhanced selectivity and ease of separation and purification of reactants and products would accompany its activity in solution phase.

Zeolite encapsulated transition metal complexes are generally referred to as zeozymes. For encapsulation of complexes, zeolite with large pore structures has been used in most cases. So that they can readily accommodate large metal complexes of ligands such as phthalocyanines, porphyrins, Schiff bases, amino acids etc. The primary

advantages are the uniform dispersion of metal ions throughout the solid and prevention of polynuclear cluster formation of metal ions. Furthermore, the framework structure of many zeolites, including the dimensions and arrangements of the cages are roughly equivalent to those that are encountered in enzyme catalysis, thus making some possible comparisons. Available space restricts the number of active complexes to one per supercage, and pore windows are not large enough to allow them diffuse and oxidize each other.

1.6.2 Methods for Encapsulating the Metal Complexes in the Zeolites

1) Ship-in-a-bottle method: Large zeolite cages offer themselves as locations for the synthesis of metal complexes with dimensions exceeding those of the pore apertures, so that they are trapped like a ship in bottle synthesis. The ship in bottle is used to immobilize such complexes within the zeolite cavities providing an opportunity to heterogenize a homogeneous catalyst system. This method is generally user for the encapsulation of transition metalphthalocyanines and porphyrazines in zeolites. The first step of preparation involves the introduction of metal ion into the zeolite cavity which is followed by the addition of a ligand.

2) Template synthesis method: This method involves assembling of the ligands from smaller species inside the zeolite cavities. In this method, metal complex which acts as a structure directing agent (template) during the hydrothermal synthesis is added to the synthesis gel. A major restriction for this method is that the metal complex to be used as the templating agent must be stable during all stages of the zeolite synthesis.

3) Flexible ligand method: This method is applied to the free ligands that are flexible enough to pass through the smaller windows to the larger cages of the zeolite host material. A flexible ligand is able to diffuse freely through the zeolite pores and make complexes with a previously exchanged metal ion. Ligand that enters the zeolite

cages complexes with the previously exchanged transition metal ions. Hence the resulting complex becomes too large to escape out of the cages. Thus metal complex is physically entrapped in the supercages of faujasite.

1.7 Density Functional Theory (DFT)

The main tool for most of the present day computational chemistry is density functional theory (DFT). DFT differ from conventional *ab initio* quantum chemical methods in that it does not formally deal with wave functions, but rather it deals with the electron density. In 1964, Hohenberg - Kohn gave two basic theorems which are fundamental statements of DFT theory.[35] The first theorem is stated as follows "*the exact ground state energy of a molecular system is a functional only of the electron density and the fixed positions of the nuclei*". It merely assures the existence of a functional for the molecular ground state but the form of functional is unknown. The second theorem establishes the variation principle, "*the exact electron density function is the one which minimizes the energy (i.e., as functional of the density), thereby providing a variational principle to find the density*". The total energy of a system consisting N_e electrons can be written in terms of the electron density

$$\rho_{KS}(r) = \Sigma \int |\Psi_i(x)|^2 \, ds \equiv \rho_{exact}(r) \qquad \ldots\ldots. (1)$$

where ψ_i denotes the single particle wave functions. The total energy in terms of a functional of the electron density is composed of four terms such as kinetic, Coulombic, exchange-correlation energy and the interaction with the external potential. So the energy functional may be written as,

$$E[\rho] = T_s[\rho] + J[\rho] + E_{XC}[\rho] + V_{ext}[\rho] \qquad \ldots\ldots. (2)$$

Where $J[\rho] = \frac{1}{2}\sum_{ij}\langle ij \mid ji\rangle = \frac{1}{2}\iint \rho(r_1)\rho(r_2) r_{12}^{-1} dr_1 dr_2$

$$V_{ext}[\rho] = \int \hat{V}_{ext} \rho(r) dr$$

$$\rho_{KS}(r) = \Sigma \int |\Psi_i(x)|^2 \, ds \equiv \rho_{exact}(r)$$

The kinetic energy ($T_s[\rho]$) and exchange-correlation terms are unknown. In 1965, Kohn and Sham developed the approach to approximate the above two terms.[36] They introduced a fictitious system of N non-interacting electrons to be described by a single determinant wave function in N "orbitals" Φ_i. In this system the non-interacting kinetic energy can be known exactly from the Kohn-Sham orbitals;

$$T_S[\rho] = -\frac{1}{2} \sum_{ij} \langle \Psi_i | \nabla^2 | \Psi_i \rangle$$

The exchange correlation functional is simply accounted from the kinetic energy differences between interacting and non-interacting systems and also from the difference between the classical and quantum mechanical electron repulsion.

$$E_{XC}[\rho] = (T[\rho] - T_s[\rho]) + (V_{ee}[\rho] - V_H[\rho]) \qquad \ldots\ldots. (3)$$

Second Hohenberg-Kohn theorem can now be applied to yield through the variation of the density, the single particle (Kohn-Sham) equations:

$$\left[-\frac{1}{2} \nabla^2 + \nu_{eff}(r) \right] \phi_i(r) = \varepsilon_i \phi_i \qquad \ldots\ldots. (4)$$

Importantly, the 'effective potential $\nu_{eff}(r)$' seen by the electrons is given by

$$\nu_{eff}(r) = V_{ne}(r) + \int \frac{\rho(r')}{|r - r'|} dr' + V_{XC}(r)$$

$\nu_{ne}(r)$ can be expressed as

$$V_{ne}(r) = -\sum_A \frac{Z_A}{|r - R_A|}$$

The exchange-correlation potential is the functional derivative of the exchange-correlation energy with respect to the density.

$$V_{\mathrm{XC}}(r) = \frac{\delta E_{XC}[\rho]}{\delta \rho(r)} \qquad \ldots\ldots. (5)$$

This set of non-linear equations (the Kohn-Sham equations) describes the behaviour of non-interacting "electrons" in an effective local potential. From equations 3 and 5, one can easily calculate the exact ground state density and ground state energy. These Kohn-Sham equations have the same structure as the Hartree-Fock equations [37, 38] with the *non-local exchange potential* replaced by the local *exchange-correlation potential* V_{xc}.

$$\left[-\frac{1}{2}\nabla^2 + \nu_{ext}(r) + \int \frac{\rho(r')}{|r-r'|}dr'\right]\phi_i(r) + \int \nu_X(r,r')\phi_i(r')dr' = \varepsilon_i\phi_i(r) \quad \ldots\ldots (6)$$

1.7.1 Exchange-Correlation Functional (E_{xc})

As stated above, E_{xc} contains not only an element differing in the kinetic energy difference between fictitious non-interacting system and real system, but it also accounts for the difference between the classical and quantum mechanical electron repulsion.

$$E_{xc} = E_x + E_c \qquad \ldots\ldots. (7)$$

Many efforts have been made to calculate the exchange-correlation energy after the successful formalism of Kohn-Sham self-consistent field methodology.[39] Local density approximation (LDA) has proved to be remarkably accurate for prediction of properties of solid states.

Kohn and Sham showed that the local density (LD) approximation as follows,

$$E_{xc}^{LD} = \int d^3 r n(r)\varepsilon_{xc}^{unif} n(r) \qquad \ldots\ldots. (8)$$

LSDA replaces LDA because spin densities are not equal in most of the cases. In local spin density approximation, the exchange-correlation energy is written as

$$E_{xc}^{LSD}[n_{\uparrow}, n_{\downarrow}] = \int d^3 r n(r) \varepsilon_{xc}^{unif}(n_{\uparrow}(r), n_{\downarrow}(r))$$

Where $\varepsilon_{xc}^{unif}(n_{\uparrow}(r), n_{\downarrow}(r)$ is the exchange-correlation energy per particle of a uniform electron gas with spin densities of $n_{\uparrow}(r)$ and $n_{\downarrow}(r)$. LSD approximates the exchange-correlation energy density of a real, spatially inhomogeneous system at each point r in space by that of a uniform electron gas with spin densities equal to the local $n_{\uparrow}(r)$ and $n_{\downarrow}(r)$. The exchange-correlation energy per particle of a uniform electron gas $\varepsilon_{xc}^{unif}(n_{\uparrow}(r), n_{\downarrow}(r)$ is obtained from Quantum Monte Carlo calculations in LSD approximation; the exchange functional is given by

$$\varepsilon_x(\rho) = -C\rho^{1/3} \qquad \ldots\ldots. (9)$$

where C is free constant for generality. A combination of Slater exchange and the Vosko, Wilk and Nusair (VWN) correlation functional was employed in the LSDA calculations.

1.7.2 Generalized Gradient Approximation (GGA)

In the generalized gradient approximation (GGA), an exchange-correlation functional form depends on both the density and its gradient but retains the analytic properties of the exchange correlation hole inherent in the LDA. The typical form for a GGA functional is,

$$E_{xc}^{GGA}[n_{\uparrow}, n_{\downarrow}] = \int d^3 r n(r) \varepsilon_{xc}^{GGA}(n_{\uparrow}, n_{\downarrow}, \nabla n_{\uparrow}, \nabla n_{\downarrow}) \qquad \ldots\ldots. (10)$$

BLYP, BP86 and BPW91 have been most widely used GGA functional and they combine the exchange functional of B88 respectively with the correlation functional of LYP, P86 and PW91.

1.7.3 Meta Generalized Gradient Approximation (MGGA)

Meta GGA functional provides an exchange-correlation functional which contains semi-local information in the Laplacian of the spin densities or local kinetic energy densities explicitly. The form of the functional is typically as follows:

$$E_{xc}^{MGGA}[n_{\uparrow}, n_{\downarrow}] = \int d^{3}rn(r)\varepsilon_{xc}^{MGGA}(n_{\uparrow}, n_{\downarrow}, \nabla n_{\uparrow}, \nabla n_{\downarrow}, \nabla^{2} n_{\uparrow}, \nabla^{2} n_{\downarrow}, \tau_{\uparrow}, \tau_{\downarrow}) \quad \text{.... (11)}$$

Where the kinetic energy density τ is, $\tau = \frac{1}{2}\sum_{i} |\nabla \phi_i|^2$.

1.7.4 Hybrid Density Functional Methods

Hybrid DFT methods provide an exact connection between the non-interacting density functional system and the fully interacting many body systems. This is also called 'adiabatic connection method' which allows for calculating the exact exchange-correlation functional. This usually contains linear combination of Hartree-Fock exact exchange functional (E_X^{HF}) and any number of exchange and correlation explicit densities functional ($E_{XC} = (1-a)E_X^{DFT} + aE_X^{HF}$). Becke adopted this approach in the definition of a new functional with coefficients determined by a fit to the observed atomization energies, ionization potentials, proton affinities and total atomic energies for a number of small molecules. In Becke three parameter functional, the exchange functional consists of a combination of exchange terms from HF, LSDA and a gradient corrected term where as the correlation functional contains a LSDA from and a gradient correction form. The resultant energy functional is

$$E_{XC}^{HF} = E_{XC}^{LDA} + 0.2(E_X^{Fock} - E_X^{LDA}) + 0.72\Delta E_X^{B88} + 0.81\Delta E_C^{PW91} \quad \text{..... (12)}$$

Here ΔE_X^{B88} and ΔE_C^{PW91} are widely used GGA corrections to the LDA exchange and correlation energies respectively.

1.7.5 Basis Set Terminology

A basis set is a set of functions used to create the molecular orbitals, which are expanded as a linear combination of such functions with the weights or coefficients to be determined. Normally, the functions are atomic orbitals and they are centered on atoms. Sometimes, the functions centered on bonds or lone pairs are also used.

1.7.6 Slater Type Orbitals

Initially, the Slater Type Orbitals (STOs) were used as basis functions due to their similarity to atomic orbitals of the hydrogen atom. They are expressed as:

$$\chi_{\zeta,n,l,m}(r,\theta,\phi)=Nr^{n-1}e^{-\zeta r}Y_{l,m}(\theta,\phi) \qquad \text{.....(13)}$$

where N is a normalization constant and ζ is called the orbital exponent r, θ and ϕ are spherical coordinates, and Y_{LM} is the angular momentum part (the function describing the "shape" of the orbital). n, l and m are quantum numbers: principal, angular momentum and magnetic, respectively.

1.7.7 Gaussian Type Orbitals

However, Slater Type Orbitals (STOs) are not suitable for fast calculations of the two-electron integrals. They were therefore replaced by Guassian Type Orbitals (GTOs). GTO functions are described as follows:

$$\chi_{\alpha,l,m,n}(x,y,z)= N \quad x^l y^m z^n \quad e^{-\alpha r^2} \qquad \text{.....(14)}$$

where N is a normalized constant and is called the exponent. x, y and z Cartesian coordinates. l, m and n are integral exponents of the Cartesian coordinates. The summation of l, m and n is called L, which is used to determine the type of orbital. For instance, s-type (L=0), p-type (L=1), d-type (L=2), f-type (L=3), etc. $\chi_{\alpha,\ l,\ m,\ n}$ are not orbitals and are called Gaussian primitives.

Unfortunately, there is a problem with d-type and higher functions. There are six possible Cartesian Gaussians, namely, x^2, y^2, z^2, xy, xz and yz, but there are only five linearly independent and orthogonal d orbitals, namely, xy, xz, yz, x^2-y^2 and $3z^2$-r^2. Similarly, f-type functions show ten possible Cartesian Gaussians, but there are only seven linearly independent f-type functions.

Together with the fact that Gaussian functions are differentiable at the nucleus (r = 0) they also show radial decay exponential in r^2, where hydrogenic real atomic orbitals decay exponentially in r. Therefore, in practice, linear combinations of GTOs have to be made to better approximate the true shape of atomic orbitals. These combinations are called contractions and the individual Gaussians are called primitives. Furthermore, there are two ways of making the contractions, segmented of general contractions. In segmented contractions, each primitive is only used once. In general contractions, all primitives are used in each contraction. GTOs are thus defined by their contractions coefficients and the orbitals exponents of each primitive.

1.8 Natural Bond Orbital Analysis

Natural bond orbital (NBO) analysis[40] have been used for studying hybridization and covalency effect in polyatomic wave functions, based on local block eigenvectors of the one-particle density matrix. NBOs were conceived as a chemists basis set that would correspond closely to the picture of localized bonds and lone pairs as basic units of molecular structure. The NBO for a localized σ bond σ_{AB} between atoms A and B is formed from directed orthonormal hybrids $\boldsymbol{h_A}$, $\boldsymbol{h_B}$ [natural hybrid orbitals [NHOs)]

$$\boldsymbol{\sigma_{AB} = C_A h_A + C_B h_B} \qquad \text{.....(15)}$$

The natural hybrids in turn composed from a set effective valence-shell atomic orbital (natural atomic orbitals [NAOs]), optimized for the chosen wave function. A distinguishing feature of such natural localized functions (analogous to classic "natural orbitals" in the Lowdin delocalized sense) is the simultaneous requirement of ***orthonormality*** and ***maximum*** occupancy, leading to compact expressions for atomic and bond properties. The filled NBOs, σ_{AB} of the "natural Lewis structure" are well adapted to describing covalency to orbitals that are unoccupied in the formal Lewis structure and that may thus be used to describe non-covalency effects. The most important of these are these antibonds $\boldsymbol{\sigma^*AB}$

$$\boldsymbol{\sigma^*AB = C_B h_A - C_A h_B} \qquad \ldots\ldots (16)$$

which arise from the same set of atomic valence-shell hybrids that unite to form the bond functions $\boldsymbol{\sigma_{AB}}$ **.** The antibonds represent unused valence-shell capacity, spanning portions of the atomic valence space that are formally unsaturated by covalent bond formation. Small occupancies of these antibonds correspond, in Hartee-Fock theory, to irreducible departures from the idealized Lewis picture and thus to small non-covalent corrections to the picture localized covalent bonds.

Natural bond orbital analysis comprises a sequence of transformations from the basis set to $\{\varphi_i\}$ localized basis sets [natural atomic orbitals (NAOs), hybrid orbitals (NHOs), bond orbitals (NBOs), and localized molecular orbitals (NLMOs)].

$$\text{Input basis NAOs} \rightarrow \text{NHOs} \rightarrow \text{NBOs} \rightarrow \text{NLMOs} \qquad \ldots\ldots.(17)$$

The localized may be subsequently transformed to delocalized natural orbitals (NOs) or canonical molecular orbitals (MOs). These steps are automated by the NBO computer program.

1.8.1 Natural Atomic Orbital

Natural Atomic Orbital (NAOs) are constructed by the occupancy-weighted symmetric orthogonalization (OWSO) procedure in which the non orthogonal AOs $\{\tilde{\varphi}_i\}$ are transformed into orthonormal AOs $\{\varphi_i\}$

$$T_{OWSO}\{\varphi_i\} = \{\varphi_i\}, <\varphi_i/\varphi_i> = \delta_{ij} \quad \text{.....(18)}$$

The transformation matrix, T_{OWSO} has the mathematical property of *minimizing* the occupancy-weighted, mean-squared derivations of the φi from the parent non orthogonal $\tilde{\varphi}_i$

$$\min\{\sum_i w_i \int |\varphi_i - \tilde{\varphi}_I|^2 d\tau\} \quad \text{.....(19)}$$

with the weighting factor $w_i = <\tilde{\varphi}_i | \tilde{\Gamma} | \tilde{\varphi}_i>$ taken as the occupancy of $\tilde{\varphi}_i$

A small set of high-occupancy (core plus valence shell) NAOs forms the "natural minimal basis" (NMB) set. The NMB set is found to describe virtually all the electron density of the system, as simple valence-shell MO theory would suggest.

1.8.2 Natural Hybrids and Natural Bond Orbitals

With the density matrix transformed to the NAO basis, the NBO program begins the search an optimal natural Lewis structure. NAOs of high occupancy (>1.99 e) are removed as unhybridized core orbital $\mathbf{K_A}$. The program next loops over one-centre blocks Γ^A, searching for lone-pair eigenvectors $\mathbf{n_A}$ whose occupancy exceeds a preset pair threshold (p_{thresh} = 1.90). The density matrix is depleted of eigenvectors satisfying this threshold, and the program then cycles over all two centre blocks Γ^{AB} searching for bond vector σ_{AB} whose occupancy exceeds $\boldsymbol{p}_{thresh}$. Each σ_{AB} is decomposed into two normalized hybrid contributions h_A and h_B from each atom in equation and hybrids from each centre participating in different bonds are

symmetrically orthogonalized to remove intra-atomic overlap. The set of localized electron pairs (K_A) $(nA)^2(\sigma AB)^2$ … found in this way constitutes a "Natural Lewis Structure" to describe the system.

1.9 Scope of the Present Work

One of the great challenges in the catalysis field is the design of an eco-friendly metal complex catalyst. Even though metal complex catalyst shows good recyclability and separability, stability concerns are not effective due to the metal leakage. The leakage problem can be rectified by the immobilization of metal complexes into the zeolite matrix. The increased stability achieved by the encapsulation into the zeolite matrix simultaneously enhances the activity, selectivity and recyclability of the catalyst. Zeolite structure has a crucial role in the catalytic properties of metal complexes. By varying the zeolite structure properties, one can control the catalytic properties of metal complexes. This will enable us to extend the application of encapsulated metal complexes catalysts to a wide range of applications. Apart from this, usage of metal complex supported zeolite bridges the homogeneous as well as heterogeneous catalysis.

In the present work, we theoretically designed and studied the catalytic activity of various transition metal incorporated zeolite structures towards economically important oxidation reactions such as allyl alcohol epoxidation, conversion of phenol into catechol and carbonyl-ene reactions. All the designed catalysts show better activity towards the respective catalytic reactions. These design criteria can be directly applied to the above-mentioned oxidation reactions to achieve better product yield, which is the extended scope of the thesis.

References

1. Baumeister, P.; Studer, M.; Roessler, F.; Ertl, G.; Knozinger, H.; Weitkamp J. Handbook of Heterogeneous Catalysis, WileyVCH, New York, 5, 2252, 1984.
2. Wood, C.O.; Garrou, P.E. *organomet*. **1984**, *3*,170.
3. Manly, T.O. *Chem.Ind. London* **1962,** 12.
4. Schinnann, I.P.; Oelavarenne, S.Y. Hydrogen Peroxide in Organic Chemistry, Information Chimie, Paris 1979.
5. Dumas, T.; Bulani, W. Oxidation of Petrochemicals: Chemistry and Technology, Appl.Sci.Publ. London 1974.
6. Bragg, W.L. The atomic structure of Mineral, Cornell University press, Ithaca, NewYork 1937.
7. Lok, B.M.; Cannen, T.R.; Messina, C.A. *Zeolites*, **1983**, *282*, 44.
8. Meier, W.M.; Holson, D. Atlas of zeolite structure types, structure commission of the Inernational Zeolite Association 1978.
9. Meir, W.M. Molecular sieves, Society of Chem.Ind.London 10, 1983.
10. Barrer, R.M. Hydrothermal Chemistry of zeolite, Academic press, London.
11. Flanigen, E.M. Proc.of the fifth international Conference on zeolites, Heyden and sons, London 1980.
12. Flanigen, E.M. ACS symposium ser. Washington D.C., 171, 80, 1976.
13. Topsoe, N.; Pederson, R.; Derouane, E.G. J. *Catal.* **1981**, *70*, 41.
14. Moscou, L.; Stud. *Surf. Sci. Catal.* **1991**, *58*, 559.
15. Loewenstein, W. *Am. Minerals* **1982**, *39*, 92.
16. Szostak, R. Molecular sieves, Principles of synthesis and identification, Van Nostard Reinold Catalysis series, New York 1937.
17. Breck, D. W.; Acara, N. A. US Patent 3, 216,789, 1965.
18. Barrer, R. M.; Villiger, H. *Z. Kristallogr.* **1969**, *128*, 352.
19. Artioli, G.; Kvick, A. *Eur. J. Mineral.* **1990**, *2*, 749.
20. Corma, A; Corell, C.; Pitrez-Pariente, J.; Guil, J.M.; Guil-Lopez, R.; Nicolopoulos, S.; Gonzalez Calbet, J.; Vallet-Regit, M. *Zeolites* **1996**, *16*, 7.

21. Cejka, J.; Van Bekkum, H. Zeolites and Ordered Mesoporous Materials: Progress and Prospects. **2005**, 157.

22. Catlow, C.R.A. Modeling of Structure and Reactivity in Zeolites, Academic Press, Ltd, London, 1992.

23. Chen, N.Y.; Garwood, W.E.; Duyer, F.G. Shape selective catalysis in industrial applications, Marcel Dekker Inc. New York 1996.

24. Argauer, R.J.; Landolt, G.R. US patent 3702886, Mobil Oil Corp. P.B.Weisz, Pure Appl.Chem. 1980, 52, 2091.

25. Chen, N.Y.; Garwood, W.E. *Catal. Rev. Sci. Eng.* **1986**, *28*, 185.

26. Landis, P.S.; Venuto, P.B. *J. Catal*. **1966**, *6*, 245,

27. Venuto, P.B.; Landis, P.S. *Adv. Catal.* **1968**, *18*, 259.

28. Venuto, P.B. *Chem.Tech.* **1971**, 215.

29. Segawa, K.; Sugiywa, A.; Sakaguchi, M.; Sakurai, K. Proc. Int.Symp. Acid base catalysis, Sapporo, Japan 1988.

30. Hoelderich, W.F.; Hesse, M.; Naeumann, F. *Angew. Chem. Int. Edit . Eng*. **1988**, *27*, 226.

31. Ozin, G.A.; Kupermonn, A.; Stein, A. *Angew. Chem*. **1989**, *101*, 373.

32. Beyer, H.K.; Borbely, G.; Miasnikov, P.; Rozsa, P. *Stud. Surf. Sci. Catal.* **1989**, *46*, 635.

33. Scicsery, S.M. *Review on Shape-selective catalysts in zeolites*, **1984**, *14*, 202.

34. Singh, A.P.; Selvam, T. *J. Mol. Catal. A: Chem.* **1984**, *113*, 489.

35. Hohenberg, P.; Kohn, W. *Physical Review* **1964,** *136* (3B), B864.

36. Kohn, W.; Sham, L. J., *Self-consistent equations including exchange and correlation effects*. APS: 1965.

37. Slater, J. C.; Phillips, J. C. *Physics Today* **1974,** *27*, 49.

38. Vosko, S. H.; Wilk, L.; Nusair, M. *Canadian Journal of Physics* **1980,** *58* (8), 1200-1211.

39. Scuseria, G. E.; Staroverov, V. N., *Theory and Applications of Computational Chemistry: The First* **2005,** *40*, 669-724.

40. Reed, A. E.; Curtiss, L. A.; Weinhold, F. *Chemical Reviews* **1988,** *88* (6), 899-926.

2. Influence of Different Zeolite Framework on the Geometry of Platinum(II)tetraammine Complex

2.0 Abstract

The structural changes in the guest platinum(II)tetraammine complex due to the steric and electronic interactions with the host zeolite LTL, MWW and Y frameworks have been investigated using density functional theory (DFT) calculations. It is observed that the square planar geometry of platinum(II)tetraammine complex has been distorted to non-planar geometry when encapsulated in supercages of zeolite framework. The distortion is found to be higher in LTL than Y and MWW frameworks, without affecting the nature of the zeolite framework. Geometrical parameters, HOMO and LUMO energies, global hardness and softness were calculated to understand the distortion in the pores of the zeolite matrix. The most plausible active site of the complex was identified using Fukui functions.

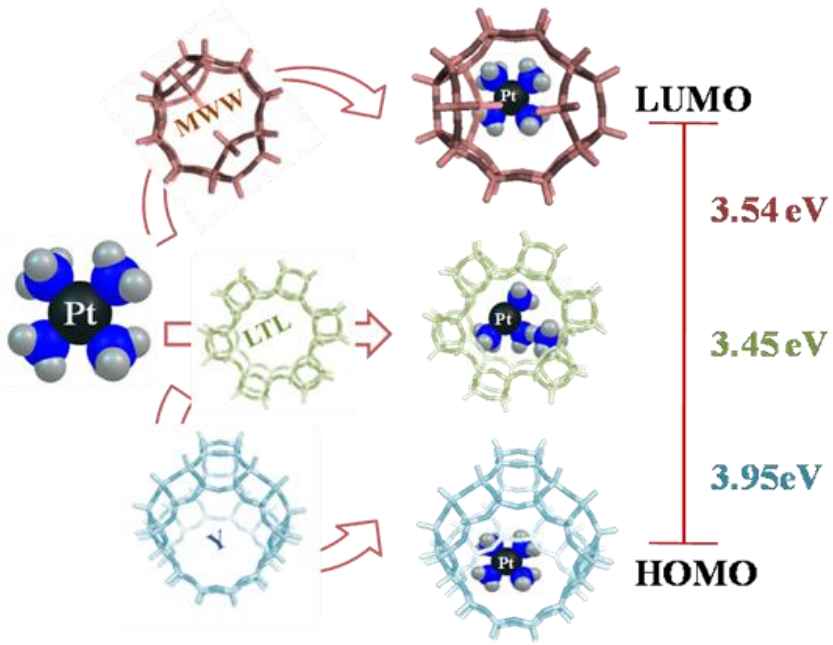

2.1 Introduction

Zeolite encapsulated transition metal complexes are interesting candidates for catalysis as their features are analogous to homogeneous and heterogeneous catalytic systems. It creates a unique environment by posing steric and electrostatic constraints on voids and walls. These constraints determine the changes in the structural, electronic, redox and magnetic properties of the encapsulated complexes, thereby contributing to the reactivity of the encapsulated complex.[1-12] Zeolite framework has a porous structure that can accommodate a wide range of cations, such as Na^+, K^+, Ca^{2+}, Mg^{2+}, and others. These cations can readily be exchanged by the incoming cations. Exchanged cation plays a major role in compensating the negative charge and increasing electropositivity thereby strengthening the zeolite framework. It controls the space availability and offers various reactive sites for the guest molecules to interact.[13,14]

Bulk transition metal oxides or on nonacid support were utilized as the first generation catalysts which were developed for the alkanes aromatization. Among metal oxides, Cr_2O_3 based materials show interesting catalytic properties. In spite of their high selectivity, low activity, and fast deactivation: transition metal oxides have paved the way for the discovery of catalysts based on supported noble metals which comprise second generation catalyst. Generally, noble metal-supported catalysts are highly active for dehydrogenation of alkanes and hydrogenolysis reactions. However, the drawback of noble metal- supported acidic supports is that they favor the formation of aliphatic hydrocarbons (light alkanes, isoparaffins, alkyl cyclo pentanes, and alkyl benzenes) than aromatic hydrocarbon. The selectivity towards aromatic hydrocarbon strongly depends on metal dispersion, alloying, passivation of metals due to carbon and/or sulfur deposition, acidic properties of the support, temperature, and pressure (hydrogen and

alkane). Among the noble metals, platinum has been found to be the best candidate as it possesses excellent catalytic behavior, adaptable/stable with solid support.[15]

Platinum clusters (5-12 atoms) supported on basic zeolite (LTL) are found to be highly selective towards dehydrocyclization of alkanes. The reason for higher selectivity is still an unsolved mystery. It could be due to alternating of the redox potential because of confinement or due to the creation of active centers for the adsorption of substrates undergoing reactions. There are few speculations over the selectivity such as non-acidic nature of the support and monofunctional catalyst with platinum which can provide catalytic sites.[16,17] Miller *et al* have proposed that cluster size plays an important role along with the presence of a nonacidic support. Furthermore, they reported that the geometry of the LTL zeolite pores is mainly responsible for the adsorption of n-hexane such that they are aligned inside the pore in a special manner which favors 1–6 ring closure in the alkane.[18,19] To resolve the mystery, the present chapter describes the theoretical investigation of platinum(II)tetraammine complex encapsulated in various zeolites such as Zeolite -Y, MWW, LTL and their catalytic activities were reasoned using studies based on density functional theory.

2.2 Computational Details

All the calculations are carried out using the Gaussian 09 program with B3LYP correlation functional using LANL2DZ basis set.[20,21] Three different zeolite frameworks (Zeolite Y, MWW and Linde type L) were created by taking 40 tetrahedral units (40T), where the supercage was saturated with hydrogens. First, crystallographic positions of Si and O atoms of the clusters were fixed and the positions of terminal H atoms were optimized. Following the Lowenstein's rule, two aluminium atoms were replaced in the position of two silicon atoms in the six-member ring to compensate two

positive charges of the complexes. The gas phase optimized platinum complex is then encapsulated inside the supercage. All geometric optimizations were performed without point group constraints.

The chemical potential (μ) and global hardness (η) can be expressed by the Koopmans theorem[22] as

$$\mu = \frac{E_{LUMO} + E_{HOMO}}{2} \quad (1)$$

$$\eta = \frac{E_{LUMO} - E_{HOMO}}{2} \quad (2)$$

where E_{LUMO} is the energy of the lowest unoccupied molecular orbital and E_{HOMO} is the energy of the highest occupied molecular orbital.

The ionization potential (IP) and electron affinity (EA) of the system defined by the finite difference approximation as follows,[23]

$$IP = E_{N-1} - E_N \quad (3)$$

$$EA = E_N - E_{N+1} \quad (4)$$

where E_N, E_{N-1}, and E_{N+1} are the energies of the N, N − 1, and N + 1 electron systems.

The global electrophilicity defined by Parr *et al* [24] is given as

$$\omega = \frac{\mu^2}{2\eta} \quad (5)$$

The global softness (S) is defined as

$$S = {}^{1}/_{2\eta} \quad (6)$$

The condensed Fukui function[25] of an atom, k, in a molecule with N electrons is defined by a finite difference approximation as,

$$f_k^+ = [\, q_k(N+1) - q_k(N) \,] \quad \text{(for nucleophilic attack)} \quad (7)$$

$$f_k^- = [\, q_k(N) - q_k(N-1) \,] \quad \text{(for electrophilic attack)} \tag{8}$$

$$f_k^0 = [\, q_k(N+1) - q_k(N-1) \,]/2 \quad \text{(for radical attack)} \tag{9}$$

where $q_k(N)$, $q_k(N + 1)$, and $q_k(N - 1)$ are the charges of the k^{th} atom for the N, N + 1, and N − 1 electron systems, respectively.

Equations 1-6 were used to calculate the global and local reactivity descriptors. Equations 7 & 8 are used to calculate Fukui functions (FFs, f_k^+ and f_k^-). The local softness value of an atom k can be defined as the product of the Fukui function and the global softness and the local softness values of selected atoms were calculated using equations 10-12.

$$S_k^+ = [\, q_k(N+1) - q_k(N) \,]S \tag{10}$$

$$S_k^- = [\, q_k(N) - q_k(N-1) \,]\, S \tag{11}$$

$$S_k^0 = [\, q_k(N+1) - q_k(N-1) \,]/2 \tag{12}$$

A generalized concept of philicity associated with a site k in a molecule was defined by Chattaraj *et al* [26] as below

$$\omega_k^\alpha = \omega f_k^\alpha \tag{13}$$

where α = +, - and 0 represent nucleophilic, electrophilic, and radical attacks, respectively.

The charge distribution in the complexes has been analyzed via the natural population analysis (NPA).[27]

2.3 Results and Discussion

2.3.1 Ground State Geometries

The optimized geometry of the neat and zeolites encapsulated platinum(II) tetraammine complex are shown in Figure 2.1. The selected geometric parameters of

the optimized neat and the zeolite encapsulated complexes from B3LYP/ LANL2DZ level calculations are tabulated in Table 2.1.

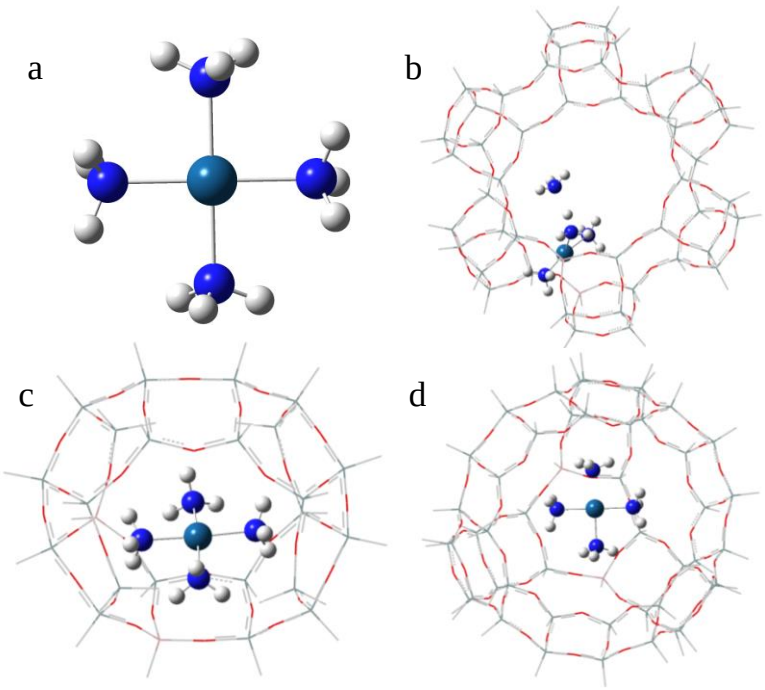

Figure 2.1. Optimized geometries of the neat a) $[Pt(NH_3)_4]^{2+}$ and encapsulated b) $[Pt(NH_3)_4]^{2+}$-LTL, c) $[Pt(NH_3)_4]^{2+}$-MWW, d) $[Pt(NH_3)_4]^{2+}$-Y complexes

The geometrical parameters of the neat complex have been compared with the encapsulated complexes. The optimized geometry of the neat complex has equal Pt-N bond length. The bond angles of N1-Pt -N3, N1- Pt -N2, N2 -Pt -N4 and N3-Pt- N4 strongly confirms the square planar geometry. After encapsulating in LTL, MWW and Y zeolite, Pt-N bond lengths and bond angles vary. Among the three encapsulated complexes the LTL zeolite experienced more deviation due to the pore size. These observations support the experimental results reported by Miller *et al*.[18]

Table 2.1 Bond length and bond angle of the neat and encapsulated complexes

Complex	**$[Pt(NH_3)_4]^{2+}$**	**$[Pt(NH_3)_4]^{2+}$ -LTL**	**$[Pt(NH_3)_4]^{2+}$ -MWW**	**$[Pt(NH_3)_4]^{2+}$ -Y**
Bond Length (in Å)				
Pt – N_1	2.11	3.11	2.03	2.09
Pt – N_2	2.11	2.08	2.11	2.11
Pt – N_3	2.11	2.04	2.09	2.12
Pt – N_4	2.11	2.09	2.10	2.08
Bond Angle (in deg)				
$N_1 \angle$ Pt $\angle N_3$	179.9	38.9	176.6	175.6
$N_2 \angle$ Pt $\angle N_4$	179.9	170.8	169.8	177.6
$N_1 \angle$ Pt $\angle N_2$	89.9	108.7	88.5	89.8
$N_3 \angle$ Pt $\angle N_4$	90.0	92.0	93.4	88.0

Table 2.1 reports the differences in bond length and bond angles of the neat and encapsulated complexes. The covalent character is proven by quantum chemical calculations of Si-O bonds in zeolites.[28] Partially delocalized electronic clouds which are contributed by valence electrons are seen all over the framework of the zeolite. At short distances the electron-electron repulsions will be operative between the complex molecule and the walls of cavities present in the zeolite, resulting in deviations in bond lengths.

2.3.2 Frontier Molecular Orbital Analysis

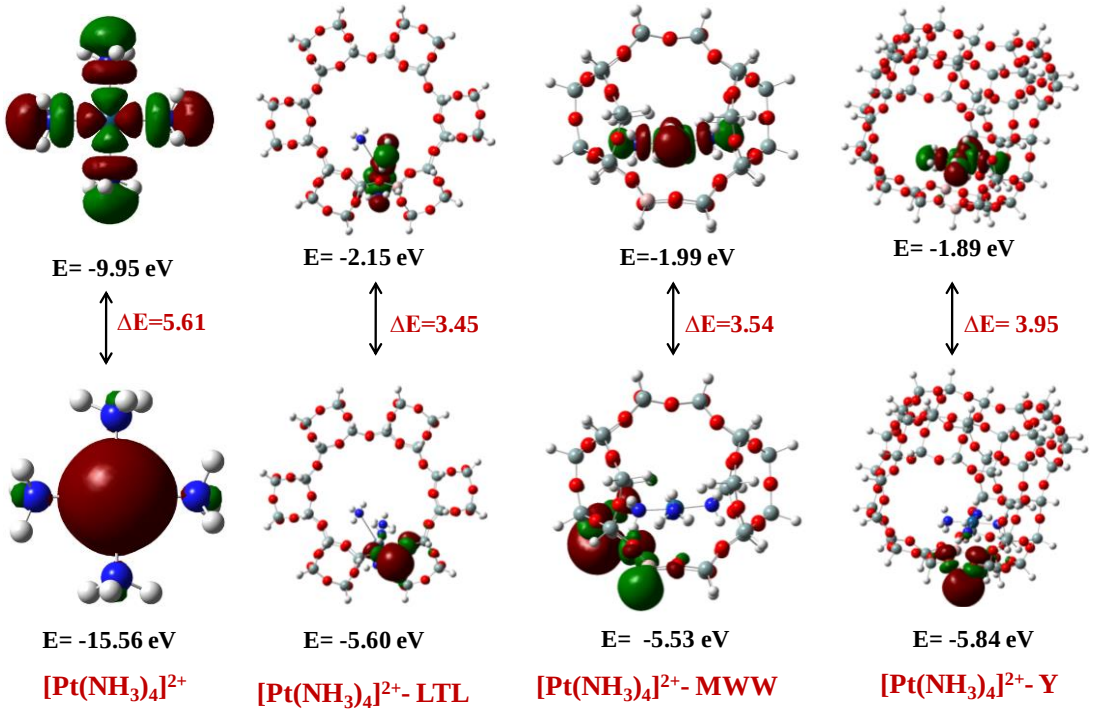

Figure 2.2 Pictorial representation of the HOMO and LUMO level of the neat and encapsulated complexes

The HOMO and LUMO energies of the neat and encapsulated complexes are represented in Figure 2.2. The HOMO energies are in the order of $[Pt(NH_3)_4]^{2+}$ < $[Pt(NH_3)_4]^{2+}$-Y < $[Pt(NH_3)_4]^{2+}$-LTL < $[Pt(NH_3)_4]^{2+}$-MWW and those of LUMOs are in the order of $[Pt(NH_3)_4]^{2+}$ < $[Pt(NH_3)_4]^{2+}$ -Y < $[Pt(NH_3)_4]^{2+}$ -MWW < $[Pt(NH_3)_4]^{2+}$ -LTL. It can be observed from Figure 2.2 that the HOMO and LUMO energies of encapsulated complexes become destabilized. The energies of the frontier orbital of the metal complexes get changed upon encapsulation, leading to a small HOMO-LUMO energy gap. These changes may be due to (i) the effect of the counterion (two aluminium atoms in zeolite), (ii) the steric constraint imparted by the zeolite matrix. When a guest molecule is confined inside the zeolite, few types of interaction are considered such as Coulombic effects, coordination effects, van der Waals interactions

and double layer effects.[29,30] These effects alter the energy levels including the metal complex chemical behavior.

Table 2.2 Orbital contribution (in %) to HOMO and LUMO for the neat and encapsulated complexes

Complex		**Pt**			**Al**		**O**	**N**	**H**
		s	**p**	**d**	**s**	**p**	**p**	**p**	**S**
$[Pt(NH_3)_4]^{2+}$	HOMO	15		85					
	LUMO			100					
$[Pt(NH_3)_4]^{2+}$-LTL	HOMO				20		14		66
	LUMO			80				20	
$[Pt(NH_3)_4]^{2+}$-MWW	HOMO				17				83
	LUMO			84				16	
$[Pt(NH_3)_4]^{2+}$-Y	HOMO				20	14			66
	LUMO			100					

The percentage of orbital contribution to each atomic orbital viz., HOMO and LUMO are given in Table 2.2. The main contributions to HOMO are from s (15%) and d (85%) orbital of platinum and LUMO are only from d orbital of platinum. After encapsulation, the main contributions to HOMO are from the s and p orbital of aluminum, p and s orbital of oxygen which is present in the zeolite matrix. The contributions to LUMO are mainly from d orbital of platinum and a small quantity is contributed by the p orbital of nitrogen. But in the case of zeolite -Y encapsulated complex, the LUMO is coming only from the d orbital of platinum. This shows that the metal complex molecular orbital cannot extend over the entire space and restricts within the dimension of the zeolite cage. Upon substitution of aluminium in zeolite matrix both, HOMO and LUMO level of platinum(II)tetraammine are stabilized. The

electrostatic potential generated inside the cage changed by the presence of Bronsted sites.

The compositions of HOMO and LUMO considering the metal complex and zeolite as two segments are calculated and are listed in Table 2.3. As apparent from the MO diagram of $[Pt(NH_3)_4]^{2+}$-LTL , the contribution of the $[Pt(NH_3)_4]^{2+}$ and LTL group is around 1.58% and 98.42%, respectively towards HOMO whereas LUMO is mainly constituted by metal complex (87%) and zeolite (13%). The HOMO of $[Pt(NH_3)_4]^{2+}$-MWW and $[Pt(NH_3)_4]^{2+}$-Y are composed largely of zeolite and LUMO is stabilized with the contributions from metal complex.

Table 2.3 Frontier molecular orbital compositions (in %) in the ground state for the neat and encapsulated complexes

Complex	**HOMO**		**LUMO**	
	Complex	**Zeolite**	**Complex**	**Zeolite**
$[Pt(NH_3)_4]^{2+}$-LTL	1.58	98.42	87.00	13.00
$[Pt(NH_3)_4]^{2+}$-MWW	1.98	98.02	97.45	2.55
$[Pt(NH_3)_4]^{2+}$-Y	2.45	97.55	98.91	1.09

2.3.3 Ionization Potential (IP), Electron Affinity (EA) and Binding Energy

The Ionization Potential (IP) and Electron Affinity (EA) values for all the complexes are calculated and tabulated in Table 2.4. The values of the ionization potential (IP) of the encapsulated complexes are less than those of the neat complex. This indicates that the encapsulated complexes will act as a better oxidizing agent. This study reports the calculated interaction energy of the encapsulated complexes as the energy differences between the optimized encapsulated complexes and the corresponding fragments (the neat complex and the zeolite). The calculated interaction energies can be ordered as $[Pt(NH_3)_4]^{2+}$-LTL (−22.87 in kcal/mol) > $[Pt(NH_3)_4]^{2+}$-Y

(−22.23 in kcal/mol) > $[Pt(NH_3)_4]^{2+}$-MWW (−21.27 in kcal/mol), which indicates that the LTL complex interacts strongly and it is stable than the other two complexes. This interaction energy differences can be attributed to changes in the geometrical parameters.

Table 2.4 Ionization potential (IP, in eV), Electron affinity (EA, in eV) and Binding energy (BE, in kcal/mol)

Complex	**IP**	**EA**	**BE**
$[Pt(NH_3)_4]^{2+}$	0.680	0.3091	-
$[Pt(NH_3)_4]^{2+}$-LTL	0.279	0.0482	-22.87
$[Pt(NH_3)_4]^{2+}$-MWW	0.262	0.0497	-21.27
$[Pt(NH_3)_4]^{2+}$-Y	0.261	0.0486	-22.23

2.3.4 Electronic Absorption Spectra in the Gas Phase from TD-DFT Calculations

TD-DFT predicted vertical excitation energies for the neat and encapsulated complexes as shown in Figure 2.3. The important d–d transitions calculated, with the corresponding energies, oscillator strengths and assignments for the neat and encapsulated complexes have been tabulated in Table 2.5.

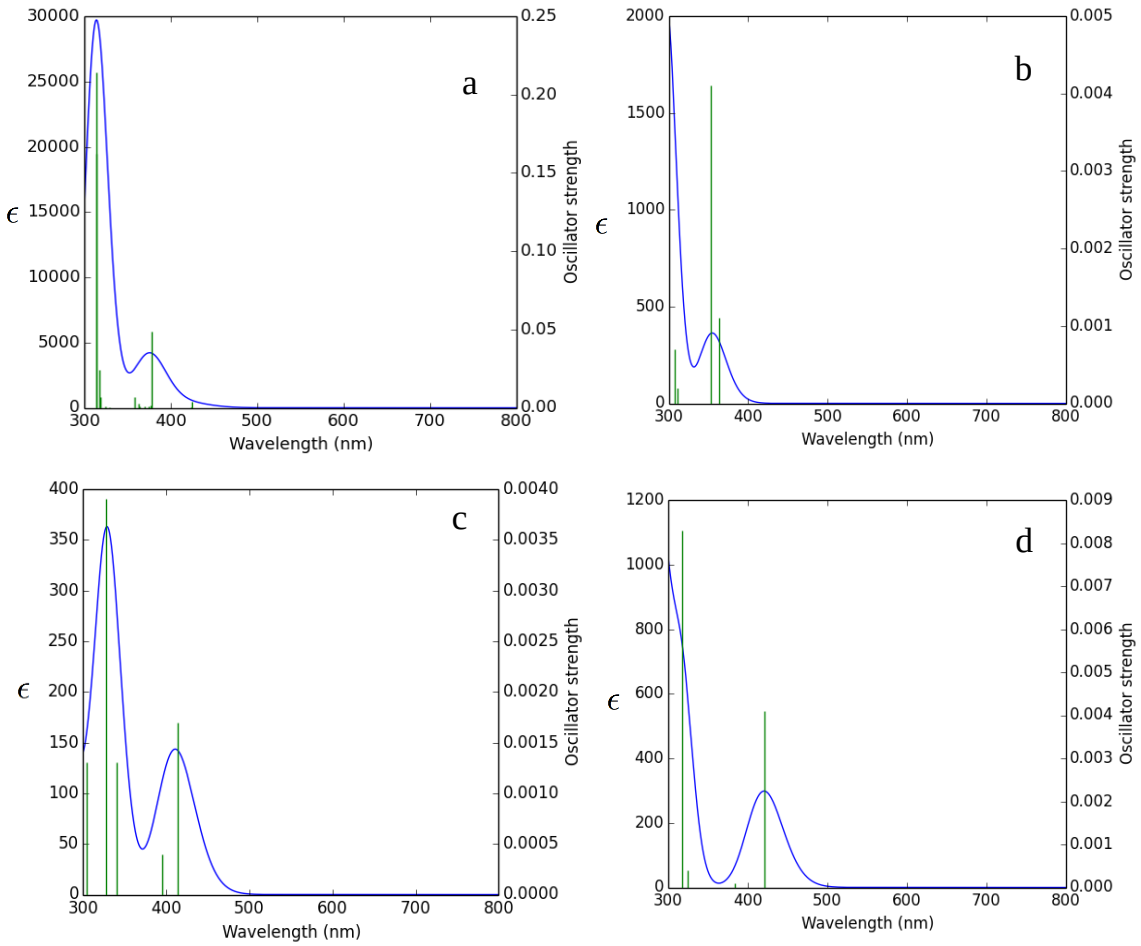

Figure 2.3 TD-DFT simulated absorption spectra for neat a) $[Pt(NH_3)_4]^{2+}$ and encapsulated b) $[Pt(NH_3)_4]^{2+}$-LTL, c) $[Pt(NH_3)_4]^{2+}$-MCM, d) $[Pt(NH_3)_4]^{2+}$-Y complexes

Detailed analysis of the TD-DFT computed electronic spectra of neat and encapsulated complexes indicates that most of the electronic transitions of the 200-400 nm regions can be characterized as the ligand to metal charge transfer transitions (LMCT). In particular, the majority of the transitions in this region are dominated by electronic excitations from the occupied MOs localized on the ammine ligands to the platinum-based LUMO which will be, for simplicity, denoted as n_π (N) $\rightarrow$ d_σ (Pt). Several electronic transitions originating from the metal-centered $d_\pi \rightarrow d_\sigma$ electronic excitations (MC or d-d) have been identified in the 280-360 nm region. The

transitions at 200-360 nm represent the d-d and N→Pt LMCT transitions. The fact that the LMCT transitions populate the highly antibonding LUMO may indicate that the corresponding charge transfer excited states are dissociative with respect to the Pt-N bond. This suggestion was proposed by the group of Sadler [40, 41] based on the DFT computations and appears to be supported by their experimental work. The population of the excited state leads to the increase of the Pt-N bond lengths. These structural changes are accompanied by the bending of (Pt-N-N) bond angle.

Neat complex shows transition around 313 nm, the most intense d-d transition with an oscillator strength of 0.2141. $[Pt(NH_3)_4]^{2+}$-LTL shows peaks at 299 and 352 nm with an oscillator strength of 0.0159 and 0.0041 due to LMCT with a significant metal d orbital participation to the ligand-based orbitals and d-d transitions. Similarly $[Pt(NH_3)_4]^{2+}$-MCM gives LMCT and d-d transitions at 254 and 327 nm with an oscillator strength of 0.0104, and 0.0039. $[Pt(NH_3)_4]^{2+}$-Y shows LMCT and d-d transitions at 236, 275 nm with an oscillator strength of 0.0151 and 0.0168.

Table 2.5 Important d–d transitions, energies, extinction coefficients and band assignments for neat and encapsulated complexes.

Complex	λ_{max} (nm)	E (eV)	f	Major and Minor Contributions
$[Pt(NH_3)_4]^{2+}$	313.48	3.9491	0.2141	H-2→L+1 (84%), H-3→L+2 (5%), H-1→L+2 (5%)
	377.60	3.2833	0.0486	H-2→LUMO (91%), HOMO→L+1 (4%)
$[Pt(NH_3)_4]^{2+}$-LTL	299.95	4.1333	0.0159	H-11→LUMO (15%), H-3→LUMO (15%), H-1→LUMO (55%), H-17→LUMO (3%),
	352.78	3.5143	0.0041	H-6→LUMO (2%) H-3→LUMO (78%), H-1→LUMO (19%)
$[Pt(NH_3)_4]^{2+}$-MCM	254.34	4.8745	0.0104	H-6→LUMO (58%), H-5→LUMO (22%), H-8→LUMO (4%), H-7→LUMO (5%), HOMO→L+4 (3%)
	327.28	3.7881	0.0039	H-1→L+1 (99%)
$[Pt(NH_3)_4]^{2+}$-Y	236.343	5.2458	0.0151	HOMO→L+5 (86%), HOMO→L+6 (4%), HOMO→L+9 (5%)
	275.84	4.4946	0.0168	HOMO→L+3 (97%)

2.3.5 Global and Local Descriptors

The global and local descriptors calculations have been performed as reported by Deka *et al.*[1,2] Table 2.6 reports the chemical hardness (η), the chemical potential (μ), and electrophilicity index (ω) values computed using B3LYP/LANL2DZ for the neat and the encapsulated complexes. The global hardness of $[Pt(NH_3)_4]^{2+}$-LTL is lower in comparison with $[Pt(NH_3)_4]^{2+}$-MWW and $[Pt(NH_3)_4]^{2+}$-Y while it has higher global softness (S) than other two encapsulated complexes. The maximum hardness and the minimum polarizability principle (MPP)[31-36] states that "hardness measures the stability and softness (polarizability) measures the reactivity". Following the stated principle, $[Pt(NH_3)_4]^{2+}$ encapsulated in LTL zeolite shows higher reactivity with maximum

softness and minimum hardness which makes this complex as the better catalyst in comparison with others complexes reported.

Table 2.6 Calculated hardness (η, in eV), Chemical potential (μ, in eV), Electrophilicity index (ω, in eV), and Global softness (S, in eV) values for the neat and encapsulated complexes

Complex	M	η	ω	S
$[Pt(NH_3)_4]^{2+}$	-12.755	2.805	29.00	0.178
$[Pt(NH_3)_4]^{2+}$-LTL	-3.875	1.725	4.352	0.289
$[Pt(NH_3)_4]^{2+}$-MWW	-3.760	1.770	3.993	0.282
$[Pt(NH_3)_4]^{2+}$-Y	-3.865	1.975	3.781	0.253

Table 2.7 Hirshfeld population analysis of Fukui functions for the selected atoms of the neat and encapsulated Complexes

Atom	$[Pt(NH_3)_4]^{2+}$		$[Pt(NH_3)_4]^{2+}$-LTL		$[Pt(NH_3)_4]^{2+}$-MWW		$[Pt(NH_3)_4]^{2+}$-Y	
	f_k^+	f_k^-	f_k^+	f_k^-	f_k^+	f_k^-	f_k^+	f_k^-
Pt	-0.4227	-0.2173	-0.0318	-0.1631	-0.0157	-0.1884	-0.0138	-0.1850
N1	-0.0254	-0.0888	0.0001	-0.0863	-0.0093	-0.1285	-0.0081	-0.0296
N2	-0.0647	-0.0885	-0.0036	-0.0307	0.0024	-0.0297	-0.0027	-0.1344
N3	-0.0254	-0.0888	-0.0171	-0.0689	-0.0082	-0.1174	-0.0038	-0.0318
N4	-0.0646	-0.0886	-0.0104	-0.0371	-0.0077	-0.0265	-0.0100	-0.1130

Table 2.8 Hirshfeld population analysis of local softness for the selected atoms of the neat and encapsulated complexes

Atom	$[Pt(NH_3)_4]^{2+}$		$[Pt(NH_3)_4]^{2+}$-LTL		$[Pt(NH_3)_4]^{2+}$-MWW		$[Pt(NH_3)_4]^{2+}$-Y	
	S_k^+	S_k^-	S_k^+	S_k^-	S_k^+	S_k^-	S_k^+	S_k^-
Pt	-0.0753	-0.0387	-0.0092	-0.0472	-0.0044	-0.0532	-0.0035	-0.0468
N1	-0.0045	-0.0158	3.5E-05	-0.0250	-0.0026	-0.0362	-0.0021	-0.0075
N2	-0.0115	-0.0157	-0.0010	-0.0089	0.0007	-0.0083	-0.0007	-0.0340
N3	-0.0045	-0.0158	-0.0049	-0.0199	-0.0023	-0.0331	-0.0010	-0.0081
N4	-0.0115	-0.0157	-0.0030	-0.0107	-0.0022	-0.0074	-0.0025	-0.0286

Table 2.9 Hirshfeld population analysis of local philicity indices for the selected atoms of the neat and encapsulated complexes

Atom	$[Pt(NH_3)_4]^{2+}$		$[Pt(NH_3)_4]^{2+}$-LTL		$[Pt(NH_3)_4]^{2+}$-MWW		$[Pt(NH_3)_4]^{2+}$-Y	
	ω_k^+	ω_k^-	ω_k^+	ω_k^-	ω_k^+	ω_k^-	ω_k^+	ω_k^-
Pt	-12.2575	-6.3002	-0.1384	-0.7096	-0.0627	-0.7525	-0.0522	-0.6996
N1	-0.7365	-2.5748	0.00052	-0.3757	-0.0372	-0.5130	-0.0308	-0.1120
N2	-1.8747	-2.5674	-0.0155	-0.1337	0.0095	-0.1184	-0.0100	-0.5083
N3	-0.7365	-2.5756	-0.0745	-0.3001	-0.0325	-0.4686	-0.0143	-0.1203
N4	-1.8739	-2.5688	-0.0451	-0.1616	-0.0306	-0.1057	-0.0378	-0.4274

Tables 2.7-2.9 present the Fukui functions (FFs, f_k^+ and f_k^-), local softness (S_k^+ and S_k^-), and electrophilicity index (ω_k^+ and ω_k^+) of the selected atoms calculated using Hirshfeld population analysis (HPA) scheme. The f_k^-, s_k^-, and ω_k^- are analyzed in the context of an electrophilic attack and the larger value of f_k^-, s_k^-, and ω_k^- corresponds to the most evident reaction site available for receiving an electrophile. It is observed from Tables 2.7-2.9, upon encapsulation, the values of the FFs at the metal centers decrease. Reported calculations[37-39] has shown that a minimum Fukui function site is preferred for hard-hard interactions and maximum for soft-soft interactions. However, upon encapsulation, the value of f_k^- is changed with the metal ion having the most positive value of f_k^-. The values of f_k^-, s_k^- and ω_k^- suggest that the encapsulation alters the reaction site.

2.3.6 Natural Population Analysis (NPA)

Table 2.10 Atomic charge distribution calculated from the natural population analysis (NPA) for the neat and encapsulated complexes

Atom	$[Pt(NH_3)_4]^{2+}$	$[Pt(NH_3)_4]^{2+}$-LTL	$[Pt(NH_3)_4]^{2+}$-MWW	$[Pt(NH_3)_4]^{2+}$-Y
Pt	+0.604	+0.592	+0.576	+0.567
N1	-1.029	-1.013	-1.049	-1.032
N2	-1.029	-1.018	-1.012	-1.030
N3	-1.029	-1.152	-1.046	-1.025
N4	-1.029	-1.042	-1.043	-1.023

The results of the NPA analysis are given in Table 2.10. The NPA charge of platinum in the neat complex is +0.6048 e while it has decreased in the zeolite system. The charge of nitrogen atoms in the neat complex is -1.0295 e which shows the compensation between the complex and surrounding zeolite matrix. The interaction energies between the complex and zeolite were found to be -22.87, -21.27, and -22.23 kcal/mol for LTL, MWW and Y encapsulated complexes respectively. It's noteworthy that the interaction energies with the amount of charge transfer between metal and the zeolite framework were revealed by the charge reduction of the metal cation.

2.4 Conclusion

Density functional theory studies done, reports the influence of different zeolite on platinum(II)tetraammine complex. Three different frameworks such as LTL, MWW, and Y zeolite were studied. The framework of the LTL zeolite can stabilize the adsorption between the complex and the cage. The interaction energy for LTL zeolite is -22.87 kcal/mol, which is higher than that for MWW (-21.27 kcal/mol) and Y (-22.23 kcal/mol). Theoretical studies confirmed that the zeolite framework walls enforce space

constraint to the metal complexes, which modifies their geometrical and catalytic behavior. The encapsulation changes the value of redox potential which in turn causes altered catalytic behavior. Supporting information is drawn from DFT calculations which shows the reduced energy between the HOMO and LUMO levels which are influenced by space constraint and coulombic electrostatic field forced by the zeolite framework. On the whole, DFT calculations report that encapsulation (i) reduces the global hardness, (ii) increases the softness and (ii) Fukui functions values of the complexes, leading to higher catalytic activity. Taking Fukui functions into account and evaluating the reactivity indexes, we conclude that the platinum atom is the most prone site for the attack of both nucleophile and electrophile.

References

1. Bania K. K.; Deka R. C. *J. Phys. Chem. C.***2011**, *115*, 9601.
2. Bania K. K.; Deka R. C. *J. Phys. Chem. C*. **2012**, 116, 14295..
3. Uzunova E.L; Mikosch H. *ACS Catal*. **2013**, 3, 2759.
4. Bania K.K.; Deka R. C. *J. Phys. Chem. C*. **2013**, *117*, 11663.
5. Majetich G.; Microwave Assisted Organic Synthesis Edited by Tierney J.P.; Lidström P Blackwell Publishing: Oxford, 2005; pp 280.
6. Corma A.; Garcia H. *Eur. J. Inorg. Chem.* **2004**, *6*, 1143.
7. Salavati-Niasari M.; Shakouri-Arani M.; Davar F. *Microporous Mesoporous Mater*. **2008**, *116*, 77-85.
8. Salavati-Niasari M.; Shaterian M.; Reza Ganjali M.; Norouzi P. *J. Mol. Catal A: Chem.* **2007**, *261*, 147-155.
9. Salavati-Niasari M. *Microporous Mesoporous Mater*. **2006,** *95*, 248-256.
10. Salavati-Niasari M. *J. Mol. Catal A: Chem.* **2006**, *245*, 192-199.
11. Salavati-Niasari M. *Inorg.Chem. Commun.* **2005**, *8*, 174-177.
12. Salavati-Niasari M. *Inorg.Chem. Commun.* **2004**, *7*, 963-966.

13. Tschernich R.W. Zeolites of the world, *Geoscience Press: 1992, pp 563*

14. Bania K. K.; Bharali D.; Viswanathan B.; Deka R. C. *Inorg. Chem.* **2012**, *51*, 1657–1674.

15. Meriaudeau P. ; Naccache C. *Catal. Rev. Sci. Eng.* **1997**, *39*, 5-48.

16. Vaarkamp M.; Grondelle J.V.; Miller J.T.; Sadjkowski D.J.; Modica F.S.; Lane G.S.; Gates B.C.; Koningsberger D.C. *Catal. Lett.* **1990**, *6*, 369.

17. Jentoft R. E.; Tsapatsis M.; Davis M. E.; Gates B. C. *J. Catal*. **1998**, *179*, 565–580.

18. Miller J. T.; Agrawal N.G.B.; Lane G.S.; Modica F.S. *J. Catal.* **1996**, *163*, 106.

19. Derouane E. G.; Vanderveken D. J. *Appl. Catal.* **1988**, *45*, 15.

20. Frisch M.J; Gaussian 09, Revision B.01; Gaussian, Inc.: Wallingford, CT, 2010.

21. Jenkins D. M.; Bernhard S. *Inorg. Chem*. **2010**, *49*, 11297.

22. Koopmans T. A. *Physica*. **1933**, *1*, 104−113.

23. Parr R.G.; Yang W. *Density Functional Theory of Atoms and Molecules* Oxford University Press: New York, **1989.**

24. Parr R.G.; Szentpaly L.V.; Liu S. *J. Am. Chem. Soc.* **1999**, *121*, 1922−1924.

25. Yang W. Mortier W.J. *J. Am. Chem. Soc.* **1986**, *108*, 5708− 5711.

26. Chattaraj P.K.; Maiti B.; Sarkar U. Philicity: *J. Phys. Chem. A.* **2003**, *107*, 4973–4975.

27. Fu H. ; Xie S.; Fu A.; Ye T. *Comp. Theor. Chem.* **2012**, *982*, 51–57.

28. Sauer J. *Chem. Rev.* **1989**, *89*, 199−255.

29. Zicovich Wilson C.M.; Corma A.; Viruela P. *J. Phys. Chem*. **1994**, 98, 10863−10870.

30. Bard A.J.; Faulkner L.R. Electrochemical Methods. Fundamentals and Applications, 2nd ed.; Wiley: New York, 2001; pp 115

31. Parr R.G.; Chattaraj P.K. *J. Am. Chem. Soc.,* **1991,** *113*, 1854− 1855.

32. Chattaraj P.K.; Liu G.H.; Parr R.G. *Chem. Phys. Lett.* **1995**, *237*, 171−176.

33. Pearson R.G. Chemical Hardness: Applications from Molecules to Solids; Wiley-VCH Verlag GMBH: Weinheim, 1997

34. Pearson R.G. *J. Chem. Educ.* **1987**, *64*, 561−567.

35. Chattaraj P.K., Cedillo A.; Parr R.G. *Chem. Phys.***1996**, *204*, 429−437.

36. Ayers P.W.; Parr R.G. *J. Am. Chem. Soc*, **2000**, *122*, 2010−2018.

37. Nguyen L.T.; Le T.N.; De Proft F.; Chandra A.K.; Langenaeker W.; Nguyen M.T.; Geerlings P. *J. Am. Chem. Soc.* **1999**, *121*, 5992.

38. Pal S.; Chandrakumar K.R.S. *J. Am. Chem. Soc.* **2000**, *122*, 4145.

39. Chattaraj P.K. *J. Phys. Chem. A.* **2001**, *105*, 511−513.

40. Ronconi L.; Sadler, P. J. *Chem. Commun.*, **2008**, 235.

41. Salassa, L.; Phillips, H. I. A.; Sadler, P. J. *Phys. Chem. Chem. Phys.*, **2009**, *11*, 10311.

3. Theoretical Studies of the Zeolite-Y Encapsulated Chlorine substituted Copper(II)phthalocyanine Complex on the Formation Glycidol from Allyl Alcohol

3.0 Abstract

Density functional theory used to study the encapsulation of copper(II)phthalocyanine and chlorine substituted copper(II)phthalocyanine to a zeolite-Y framework. Changes occurring in the redox properties, as well as the redshift of the time-dependent DFT (TD-DFT) spectra, point out the influence of encapsulation on the geometric parameters of the complexes. Also, the TD-DFT calculations show good agreement with the energy changes occurred in the HOMO and LUMO. DFT based descriptors are used for scrutinizing the reactivity of the encapsulated complexes and a mechanism of the glycidol formation is proposed based on the energetics involved in the transformation.

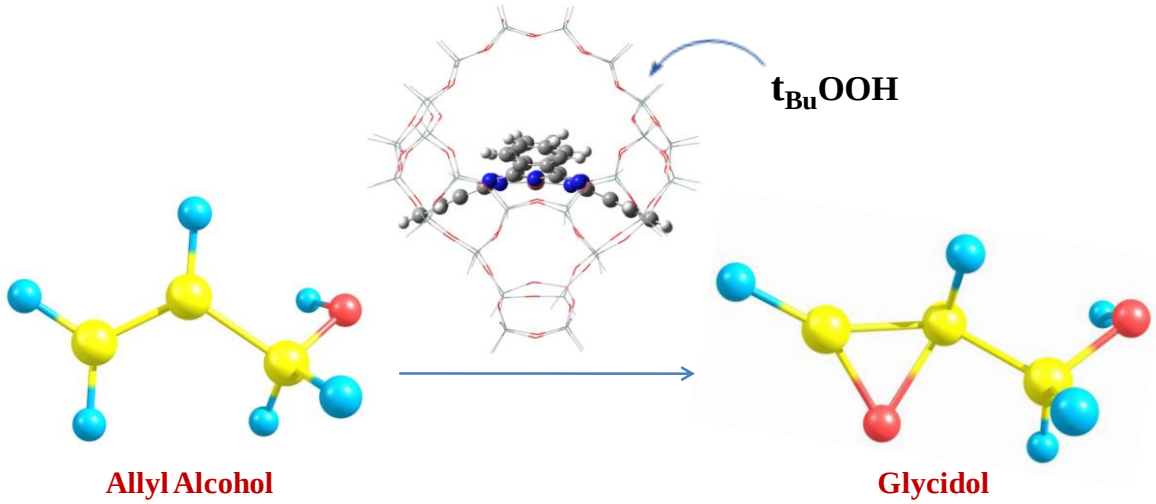

3.1 Introduction

Metallophthalocyanine (MPc) complexes, widely known as enzyme mimic catalysts have been used for activating peroxides.[1-4] Phthalocyanine compounds with N4-macrocycles, an analog to porphyrin molecule are highly stable owing to their diverse coordination. It exhibits excellent spectroscopic properties and reversible redox chemistry.[5-8] The catalytic performance of these phthalocyanine catalysts was hindered basically because of two main reasons: aggregation leading to the formation of inactive dimers and oxidative self-destruction at some point in the catalytic oxidation. To minimize these problems various supports such as zeolites, graphene, carbon nanotube, chitosan and fibrous materials (silk, cellulose) were utilized to immobilize these catalysts.[9-15] Among various supports, zeolites were considered as ideal candidates because of their distinctive framework. The geometry and physicochemical properties of the encapsulated complex could be altered by the topology (voids), steric and electrostatic constraints obliged by zeolite framework walls. The encapsulated complex shows better reactivity than the homogeneous counterparts of the same. These complexes are generally used as an alternative to the most of the biosystem and known as zeozymes.[16-23]

Recently, metal phthalocyanine-based complexes have been widely used as the catalyst for alkane and alkene oxidation reactions. However, the major drawback of this application is the mechanism and the species which is actively involved in the mechanism is not well established. To overcome these problems much effort is focused to design the novel catalyst in the aspect of the mechanistic path. However, only some of the reports have been paying attention to the use of these biomimetic catalysts over epoxidation reactions (e.g. allyl alcohol epoxidation).[24-29] Jana *et al* [30] have used Cu(II) complex encapsulated Si-MCM-41 for the epoxidation of a variety of olefinic compounds (styrene and allyl alcohol) using *tert*-BuOOH as the oxidant. The complex

has been reported showing tremendous catalytic activity with a conversion of 73% than Cu(II) complex alone. Ti-MWW and TS-1 ZSM-5 have been utilized for the bis(allyl)-ether and allyl alcohol epoxidation, where the catalysts oxidise effectively to their corresponding ethers, allyl glycidyl ether and bis(glycidyl) ether. The reaction has been supported with 30% aqueous hydrogen peroxide.[31,32] The allyl alcohol epoxidation is a big challenge in the industrial point of view because of their wide range of applications in the field of organic synthesis and pharmaceuticals.[33-38] Allyl alcohol undergoes epoxidation and gives glycidol. Glycidol is used as an oil additive, precursor and stabilizer for the synthesis of novel polymers. Because very few studies have been reported in this area, here, we have focused on understanding the physicochemical properties of zeolite-Y encapsulated phthalocyanine and tetra-chlorine substituted phthalocyanine Cu(II) complexes. Geometrical and electronic alterations in the encapsulated catalyst were studied using DFT and TD-DFT studies to confirm the environment of the same.

3.2 Computational Methods

G09 program is used to perform the density functional calculations with B3LYP/6-31G(d,p) level.[39-43] The Faujasite zeolite framework has been chosen, and the cluster dimension was reduced to 40 tetrahedral units (40T). In the zeolite framework, Si and O atoms were held on their respective crystallographic positions, and all the terminal positions were optimised using H atoms. Al atoms were substituted with two Si atoms, in the six-member ring satisfying Lowenstein's rule. The starting geometry of copper(II)phthalocyanine (CuPc) is taken from the X-ray diffraction data from the literature.[44] The free neat complex was first optimised in the gaseous state followed by encapsulation inside supercage. Geometric optimisations were done eliminating the point group constraints.

The chemical potential (μ) and global hardness (η) can be calculated as follows, [45]

$$\mu = \frac{E_{LUMO} + E_{HOMO}}{2} \quad (1)$$

$$\eta = \frac{E_{LUMO} - E_{HOMO}}{2} \quad (2)$$

where E_{LUMO} is the LUMO energy and E_{HOMO} is the HOMO energy.

The global electrophilicity calculated by Parr *et al* [46] as follows,

$$\omega = \frac{\mu^2}{2\eta} \quad (3)$$

The calculation of the global softness is done by,

$$S = {}^{1}/_{2\eta} \quad (4)$$

The Fukui function [47] of an atom, k, is calculated using the following equations,

$$f_k^+ = [\, q_k(N+1) - q_k(N) \,] \quad \text{(for nucleophilic attack)} \quad (5)$$

$$f_k^- = [\, q_k(N) - q_k(N-1) \,] \quad \text{(for electrophilic attack)} \quad (6)$$

$$f_k^0 = [q_k(N+1) - q_k(N-1)]/2 \quad \text{(for radical attack)} \quad (7)$$

where $q_k(N)$, $q_k(N + 1)$, and $q_k(N - 1)$ are the charges of the k^{th} atom for the N, N + 1, and N − 1 electron systems, respectively.

Time-dependent DFT (TD-DFT) calculations were performed at the B3LYP /6-31G (d,p) level from the ground-state optimised geometry. Conductor-like polarizable continuum model (C-PCM) was used for solvation effects. We have computed 100 excitation energies. Transition states were confirmed by frequency analysis.

3.3 Results and Discussion

3.3.1 Geometrical Parameters

Planar complexes such as porphyrins and phthalocyanines show two types of distortions such as saddle and ruffled distortions. In ruffled geometry, because of counter-rotation of different isoindole rings, N_β and two isoindole carbon atoms are displaced perpendicularly to the molecular plane. However, in saddle-type distortion, each pair of isoindole C_β carbon atoms lies above and below of the molecular plane together with the axis joining pyrrole C_α atoms and it makes the central CuN_8 ring as planar. Because of this distortion, the ruffled geometry was not considered, and the centre of inversion of CuPc molecule also preserved as not like the saddle distortion. The isoindole ring displacements were equivalent and upright to the molecular plane: for this reason, only symmetric saddle distortions have been considered. From the optimised saddle-deformed geometry, the isoindole rings tetrahedrally distorted to accommodate into the zeolite framework supercage and this distortion results in lower interaction energy.[23] The geometry of CuPc does not have a centre of inversion. The optimized geometry of CuPc, $CuPcCl_4$, CuPc-Y and $CuPcCl_4$-Y complexes have been shown as follows (Figure 3.1).

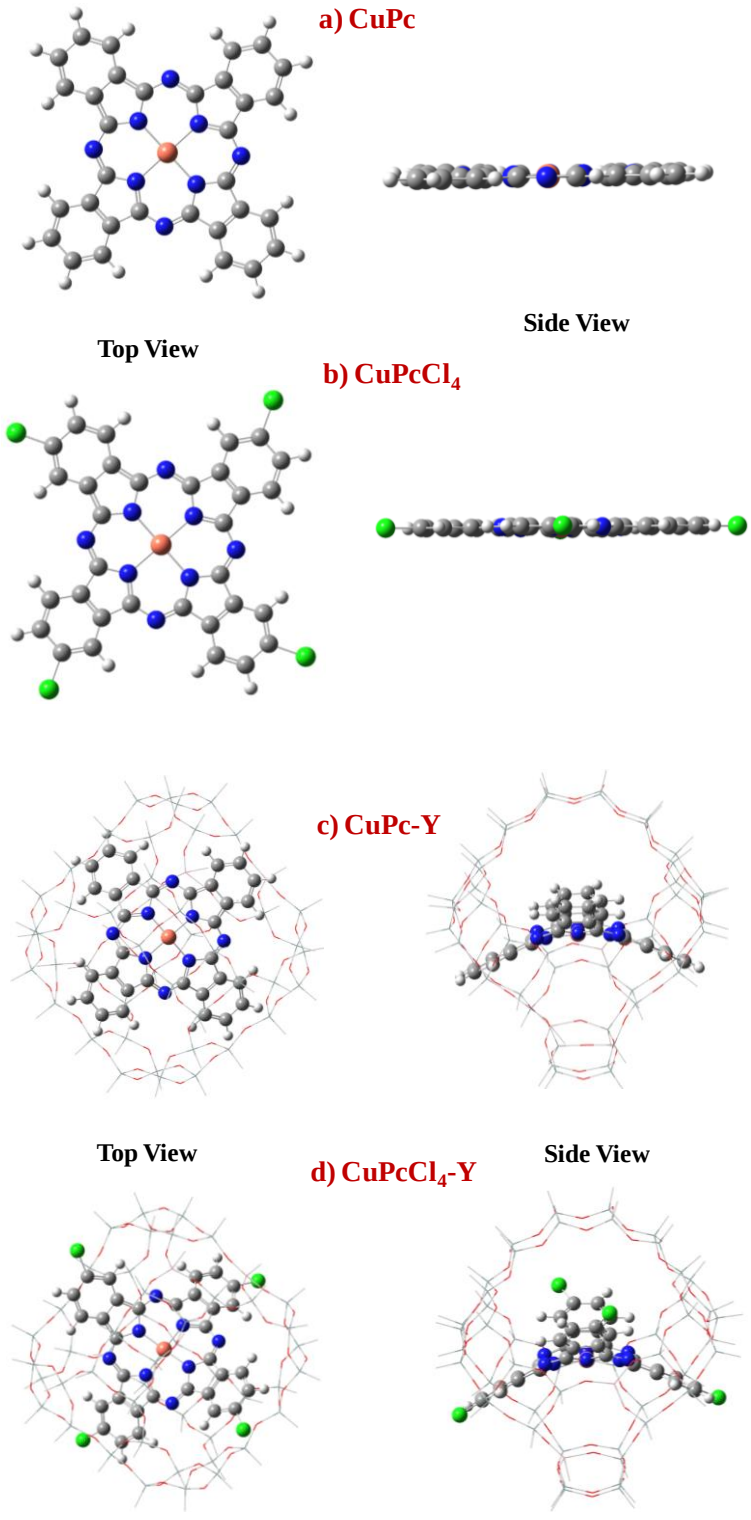

Figure 3.1 Optimized structures of the a) CuPc, b) $CuPcCl_4$, c) CuPc-Y and d) $CuPcCl_4$-Y complexes

Table 3.1 Geometrical parameters of the optimized CuPc, $CuPcCl_4$, CuPc-Y and $CuPcCl_4$-Y complexes

Bond Distances (Å) **/Angles** (in deg)	**CuPc**	**$CuPcCl_4$**	**CuPc-Y**	**$CuPcCl_4$-Y**
Cu-N8	1.953	1.954	1.908	1.908
C7-N21	1.324	1.324	1.373	1.390
C7-C3	1.457	1.456	1.481	1.482
C4-C3	1.395	1.396	1.379	1.377
C4-C5	1.405	1.405	1.437	1.440
C2-C3	1.393	1.392	1.415	1.419
C1-C2	1.408	1.408	1.393	1.386
∠C9-N8-C7	108.23	108.27	107.18	107.84
∠N8-C7-N21	127.65	127.61	125.63	124.45
∠C7-N21-C24	122.91	122.87	121.07	120.64
∠N8-C7-C4	109.47	109.48	110.56	109.62
∠C7-C4-C5	106.40	106.41	106.13	106.81
∠C5-C4-C3	121.20	120.99	121.50	121.34
∠C4-C3-C2	117.58	118.00	117.44	119.93
∠N12-Cu-N23	179.24	179.49	169.97	166.98

The geometrical parameters from B3LYP/6-31G(d,p) level calculations for CuPc, $CuPcCl_4$, CuPc-Y and $CuPcCl_4$-Y complexes are given in Table 3.1. The calculated geometrical parameters of the CuPc are in good concurrence with the metal phthalocyanine complex reported earlier. After encapsulation, changes are observed in the geometrical parameters of the metal complexes, this shows that zeolite encapsulation changes the metal active sites. The bond angle between N12-Cu-N23 is 169.97 and 166.98 for CuPc-Y and $CuPcCl_4$-Y complexes. This shows that chlorine

substituted phthalocyanine complexes undergoes more distortion than unsubstituted phthalocyanine complex.

The CuPc is found to be planar and in concurrence with the available computational and experimental information. In 1935, Robertson reported that the X-ray structural studies of NiPc, CuPc and PtPc[48] and revealed that the metal atom lies in a plane surrounded with the four isoindole nitrogen atoms.

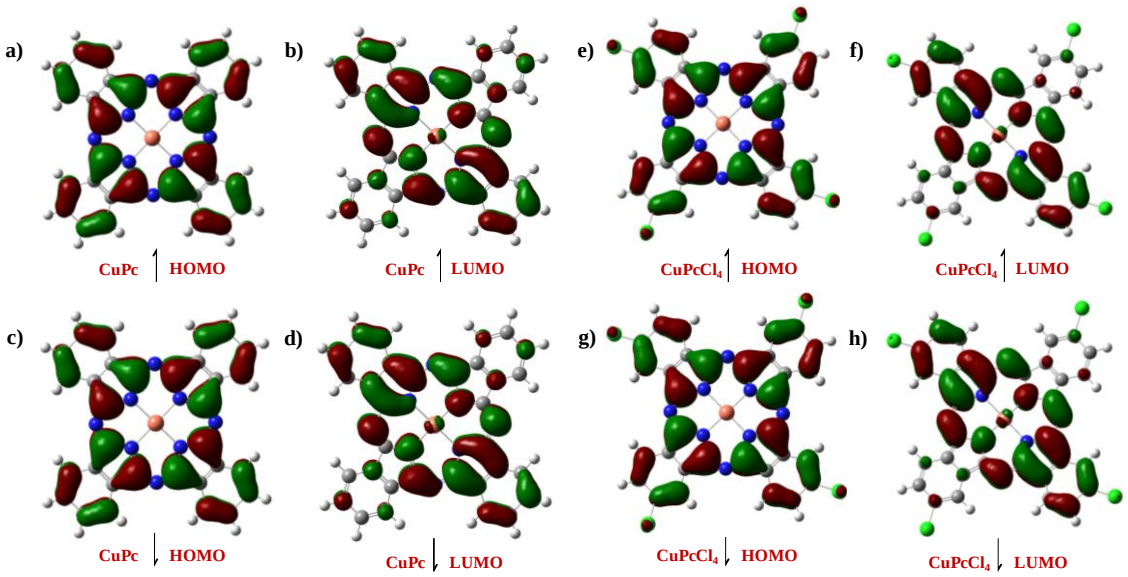

Figure 3.2 HOMO-LUMO of CuPc and $CuPcCl_4$ complexes. The arrows represent spin-up (↑) and spin-down (↓) states

3.3.2 Frontier Molecular Orbitals

It is evident that from the Figures 3.2 and 3.3 that the HOMO-LUMO patterns were qualitatively equivalent. Spin unrestricted calculations performed with all the complex systems because of Cu(II) open-shell d^9 configuration system. The frontier orbital energies (spin-up and spin-down states) of CuPc, $CuPcCl_4$, CuPc-Y and $CuPcCl_4$-Y were found to be different (Table 2).

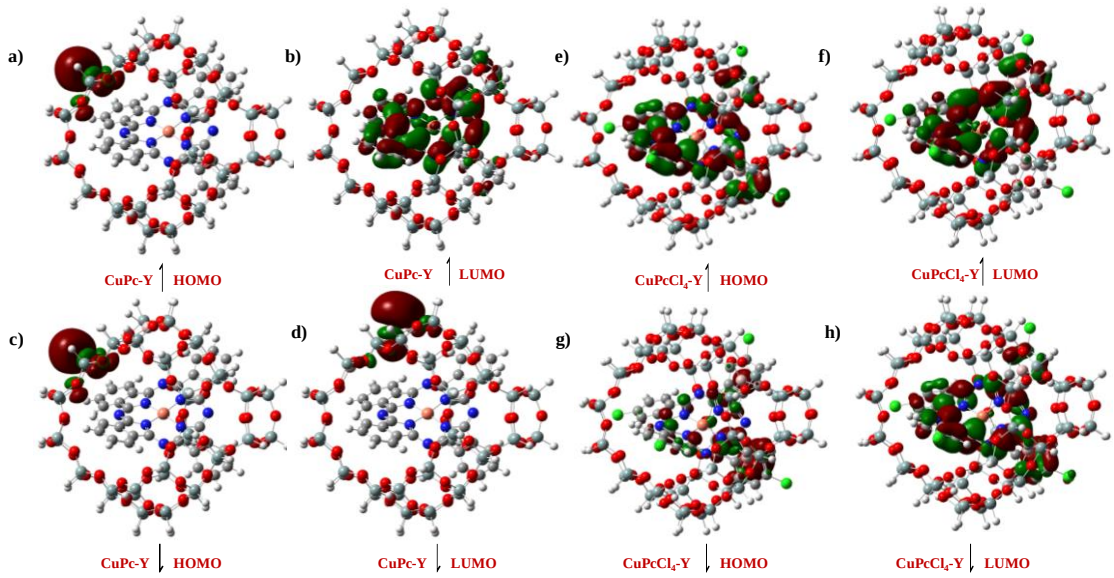

Figure 3.3 HOMO-LUMO of CuPc-Y and $CuPcCl_4$-Y complexes. The arrows represent spin-up (↑) and spin-down (↓) states

The HOMO and LUMO populations of the CuPc, $CuPcCl_4$, CuPc-Y and $CuPcCl_4$-Y are presented in Figures 3.2 and 3.3, and the gap between these two states found to be 2.19 (↑), 2.23(↓) eV, 2.18(↑), 2.21(↓) eV, 3.98 (↑), 3.50 (↓) eV and 4.90 (↑), 5.39 (↓) eV for CuPc, $CuPcCl_4$, CuPc-Y and $CuPcCl_4$-Y respectively. The neat complexes have planar geometry. However, the encapsulated complexes have a distorted planar geometry because of the steric hindrance and counterion effect of the zeolite-Y framework, and this leads to a change in the frontier orbital energy levels. A Coulombic interaction and coordination effects exist between the zeolite walls and the metal complex. The encapsulation stabilises the HOMO level to a lower energy and LUMO to a higher energy and leads to higher energy gap and it is found to be correlated with the absorption spectrum of the encapsulated complex and the redshift indicates the structural distortion. The interaction energy is found to be in the order of $CuPcCl_4$-Y (-20.64 in kcal/mol) > CuPc-Y (-15.89 in kcal/mol) . This shows that the

$CuPcCl_4$-Y has stronger interaction than CuPc-Y. Global and local descriptors were calculated to understand the reactivity of the molecular system.

Table 3.2 Values of HOMO-LUMO energy levels, Chemical potential (μ), Hardness (η), Electrophilicity index (ω) and Softness (S) in eV

Complex	**HOMO**	**LUMO**	**μ**	**η**	**ω**	**S**
CuPc(↑)	-4.94	-2.75	-3.845	1.095	6.750	0.456
CuPc(↓)	-4.96	-2.73	-3.845	1.115	6.629	0.448
$CuPcCl_4$(↑)	-5.39	-3.21	-4.300	1.090	8.481	0.458
$CuPcCl_4$(↓)	-5.40	-3.19	-4.295	1.105	8.347	0.452
CuPc-Y(↑)	-5.87	-1.89	-3.884	1.991	3.788	0.251
CuPc-Y(↓)	-5.87	-2.37	-4.126	1.750	4.863	0.285
$CuPcCl_4$-Y(↑)	-6.60	-1.70	-4.155	2.452	3.521	0.203
$CuPcCl_4$-Y(↓)	-6.60	-1.21	-3.911	2.697	2.835	0.185

3.3.3 Absorption Spectra

TD-DFT calculations have been performed in various solvents using the B3LYP /6-31G(d,p) basis level. Conductor-like polarizable continuum model (C-PCM) was used for solvation effects. Copper(II)phthalocyanine exhibits Soret bands (n→ π*) around 330-370 nm and Q (π→ π*) bands around 600–780 nm. These bands have been assigned to $a_{1u} \rightarrow e_g$ and $a_{2u} \rightarrow e_g$ transitions. In the gas phase, the CuPc and $CuPcCl_4$ complexes show Q bands at 518, 592 nm and 523, 597 nm respectively. These bands are redshifted to 556, 778 nm and 592, 718 nm in the encapsulated complexes. The Soret bands are also redshifted from 334 and 357 nm to 347 and 364 nm for CuPc and $CuPcCl_4$ respectively. The solvent effects on absorption properties were studied using different solvents. Table 3.3 shows that the largest redshift of the Q band for both neat and encapsulated complexes in DMSO. The LUMO gets stabilized if the transition

shifts to longer wavelength. According to that, the metal complex LUMO orbital gets stabilized while it interacts with coordination solvents. From this, it is evident that the zeolite supercage effectively accommodates the complexes. In consequence, the encapsulation results in the distortion of the structure of CuPc and $CuPcCl_4$ because of steric hindrance.

Table 3.3 Absorption values of CuPc, $CuPcCl_4$, CuPc-Y and $CuPcCl_4$-Ycomplexes in various solvents

Solvent	Wavelength (nm)			
	CuPc	**$CuPcCl_4$**	**CuPc-Y**	**$CuPcCl_4$-Y**
DMF	332,620,681	356,622,686	345,673,686	363,678,691
DMSO	339,619,692	356,621,698	352,676,745	362,681,757
Ethanol	339,616,673	355,618,676	352,683,744	361,693,748

3.3.4 Global Descriptors

The global descriptor values are given in Table 3.2. The maximum hardness principle (MHP) [49,50] reveals that the complex stability increases with its hardness. The chemical hardness of CuPc, $CuPcCl_4$, CuPc-Y and $CuPcCl_4$-Y complexes are observed at 1.095 and 1.115 eV; 1.090 and 1.105 eV; 1.991 and 1.750 eV; and 2.452 and 2.697 eV respectively. Thus, the encapsulated complexes show better stability corresponding to that of the neat complexes. The electrophilicity index of the encapsulated complexes shows that the minimum electrophilicity and maximum hardness are responsible for its higher reactivity. The higher chemical potential value of the encapsulated complexes makes it more active toward electron transfer reactions compared with the neat complexes.

3.3.5 Local Descriptors

Hirschfeld population analysis (HPA) has been carried out to evaluate the Fukui function (f_k^+ and f_k^-) values of copper and four nitrogens present in the complexes CuPc, $CuPcCl_4$, CuPc-Y and $CuPcCl_4$-Y (Table 3.4). A site having a minimum value of Fukui function favors the hard-hard interaction, whereas that of maximum value favors the soft-soft interaction.[51-53] Because the central copper atom of the encapsulated complex showing a minimum Fukui function value, the zeolite framework influences the metal reactivity and enhances the hard–hard interaction.

Table 3.4 Fukui function values of CuPc, $CuPcCl_4$, CuPc-Y and $CuPcCl_4$-Y complexes

Selected Atom	CuPc		CuPc-Y		$CuPcCl_4$		$CuPcCl_4$-Y	
	f_k^+	f_k^-	f_k^+	f_k^-	f_k^+	f_k^-	f_k^+	f_k^-
Cu	-0.0177	-0.1303	0.0296	-0.1870	-0.0148	-0.1421	-0.0220	-0.0121
N1	-0.0189	-0.0100	-0.0076	0.0178	-0.0178	0.00036	-0.0164	0.0141
N2	-0.0190	0.0064	-0.0261	0.0204	-0.0178	-5.5E-05	-0.0162	0.0124
N3	-0.0189	0.0065	-0.0349	0.0408	-0.0178	1.5E-05	-0.0136	0.0115
N4	-0.0189	-0.0101	-0.1159	0.1108	-0.0179	0.0006	-0.0154	0.0104

3.3.6 Energy and Spin Density

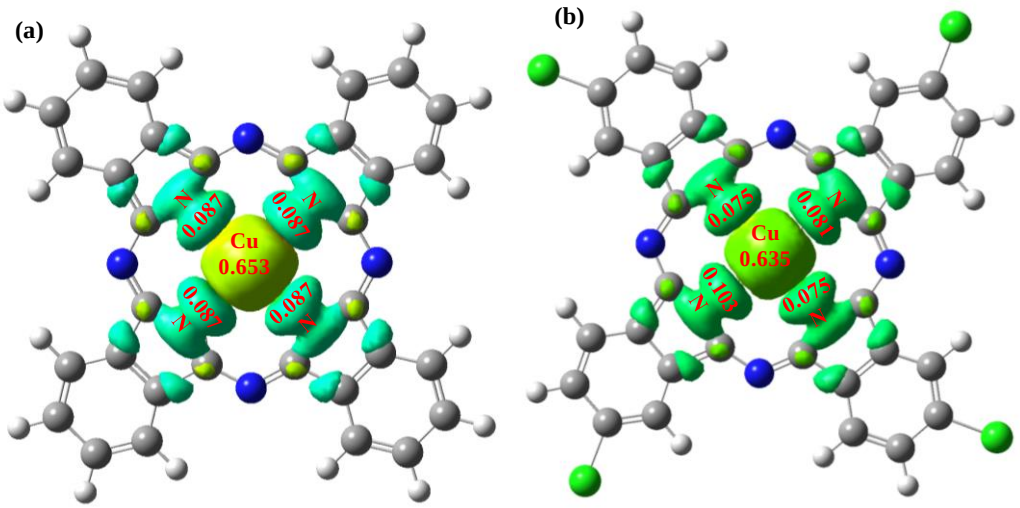

Figure 3.4 Representation of spin density distribution in a) CuPc b) $CuPcCl_4$ complexes

The energies of the CuPc, $CuPcCl_4$, CuPc-Y and $CuPcCl_4$-Y complexes are tabulated in Table 3.5. The spin density values were calculated for CuPc, $CuPcCl_4$ complexes and they are presented in Figure 3.4. The central copper atom has high Mulliken charge density and the four coordinated nitrogen atoms have lesser density. The high charge density on central Cu atom implies that the unpaired d electron is presented on the metallic center and not over the ligands aromatic rings.[54]

Table 3.5 Energies of the CuPc, $CuPcCl_4$, CuPc-Y and $CuPcCl_4$-Y complexes

Complex	Energy (in Hartree)
CuPc	-3307.57
$CuPcCl_4$	-5145.84
CuPc-Y	-22561.04
$CuPcCl_4$-Y	-24394.04

3.3.7 A Possible Mechanism for the Conversion of Allyl Alcohol to Glycidol in Presence of CuPc and ^{t}BuOOH

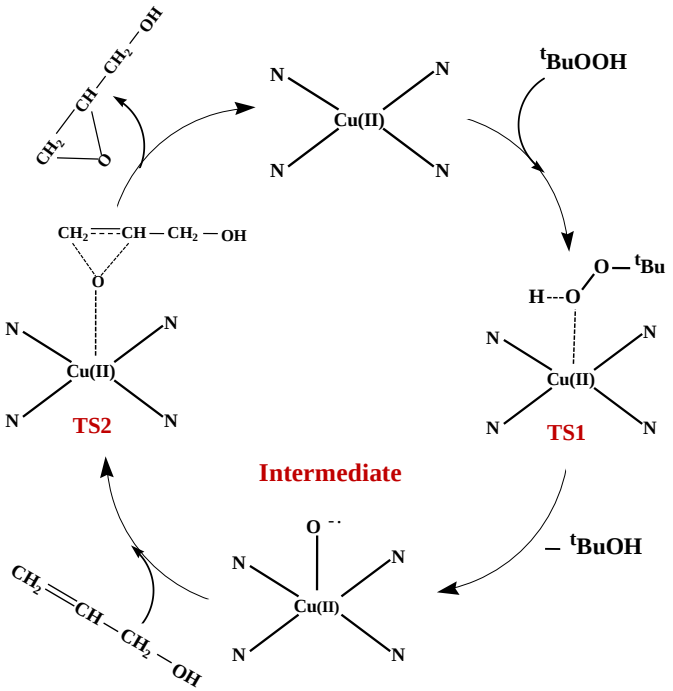

Scheme 1. Possible reaction path for glycidol formation

A possible catalytic cycle for allyl alcohol transformation into glycidol in the presence of CuPc and ^{t}BuOOH is presented in scheme 1. The mechanism involves a direct electrophilic attack of the peroxo group of the allyl alcohol. DFT studies focused on the allyl alcohol epoxidation mechanism including the location of transition states and activation barriers of oxygen transfer. The calculations disclose that direct nucleophilic attack of the allyl alcohol at electrophilic peroxo oxygen centre is preferred. An active species CuPc* is generated via electron transfer between CuPc and ^{t}BuOOH. This leads to the formation of CuPc-$O^{-\cdot}$ intermediate by the interaction of peroxo O to Cu^{2+}. Finally, the transfer of oxygen from peroxide to allyl alcohol resulted in the formation of glycidol.

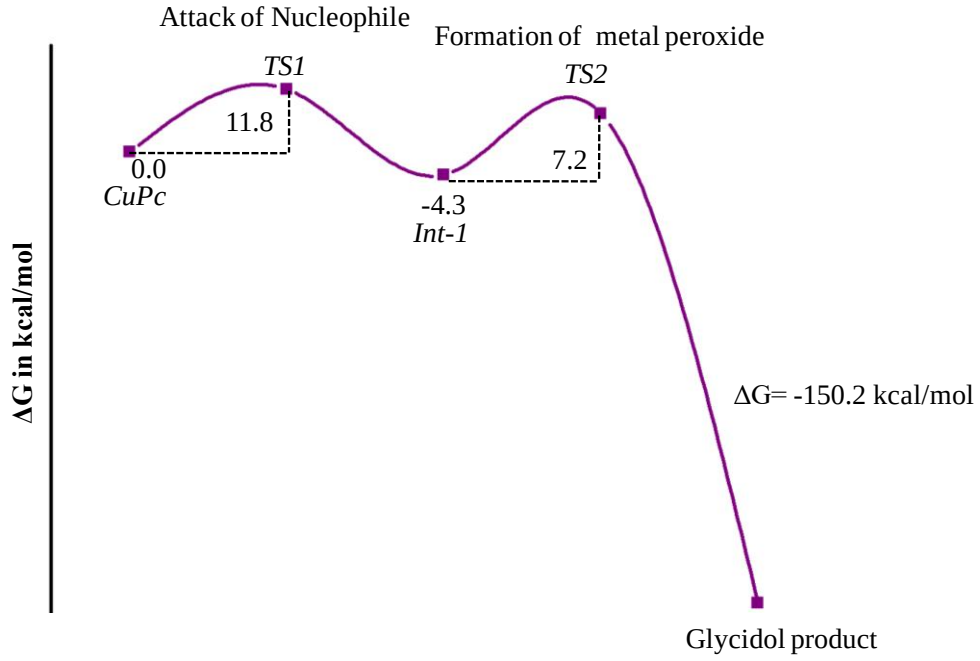

Figure 3. 5 Simple energy profile diagram for the catalytic conversion

The addition of tertiary butyl hydrogen peroxide to the CuPc complex through the axial position forms a weekly bound Cu(II)Pc.^{t}BuOOH complex via TS1. The transition step is associated with an energy barrier of 11.8 kcal/mol. In the TS1, the

oxygen atom of ^{t}BuOOH moves toward the metal centre and leads to the formation of Cu-O linkage. The optimised intermediate state geometries show the weakly bound complex formed via the interaction of the metal centre with one of the peroxide-oxygen moiety. The oxidation state of copper in the intermediate remains as Cu(II). Cu(III) intermediates were proposed by Hamilton *et al* [56] in galactose oxidase base. However, later it was found to be Cu(II). The experimental reports indicate that, without forming the high valent copper center, Cu(II)- hydroperoxo complexes which are present in the biological system directly oxidize the substrates. [55-58] The Cu···O distance is 2.09 Å. If allyl alcohol inserts to the metal peroxide complex, oxygen from peroxide transferred to allyl alcohol (TS2) leading to the formation of product and CuPc subsequently regenerated. This transition step TS2 has an energy barrier of 7.2 kcal/mol. The energy profile diagram for this conversion is given in Figure 3.5.

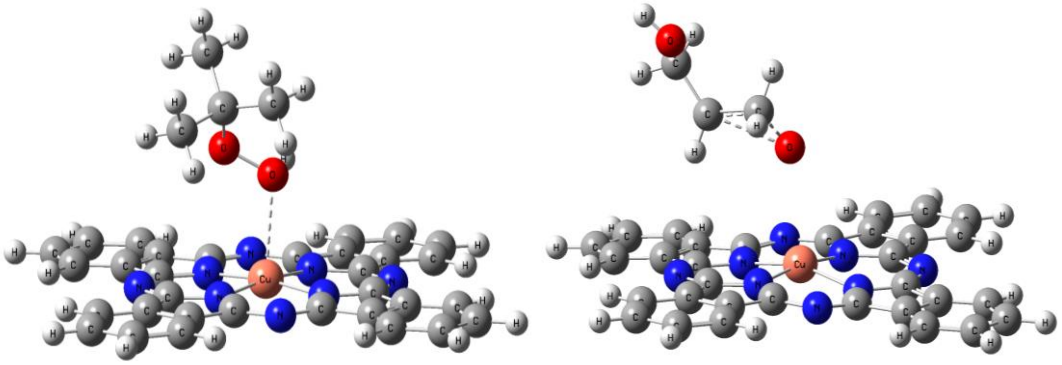

TS1 TS2

Figure 3.6 The possible transition states involved in the glycidol formation

3.4 Conclusion

Square planar phthalocyanine and tetra- chlorine substituted phthalocyanine complexes of Cu(II) are encapsulated with zeolite-Y, and studied using different DFT studies. It revealed that zeolite framework walls impose steric hindrance and modify the overall behaviour of the complex. DFT calculation further supports that encapsulation changes the values of the global, local and Fukui function values of the

complexes, resulting in the higher catalytic ability. The electron transfer process is responsible for the interaction of ^{t}BuOOH with metal complexes. The encapsulated complexes show better catalytic activity than the free complexes.

References

1. Han, Z.; Han, X.; Zhao, X.; Yu , J.; Xua, H.*J. Hazard. Mater*. **2016**, *320*, 27–35.
2. Joseph, J.K.; Jain, S.L.; Sain, B. *Ind. Eng. Chem. Res.* **2010**, *49*, 6674–6677.
3. Huang, Z.; Bao, H.; Yao, Y.; Lu, W.; Chen, W. *Appl. Catal. B: Environ*. **2014**, *154*, 36–43.
4. Gao, M.; Li, N.; Lu,W.; Chen, W. *Appl. Catal. B: Environ*. **2014**, *147*, 805–812.
5. Drozd, D.; Szczubialka, K.; Lapok, L.; Skiba, M.; Patel, H.; Gorun, S.M.; Nowakowska, M.*Appl. Catal. B: Environ.* **2012**, *125*, 35–40.
6. Lu,W.; Chen, W.; Li, N.; Xu, M.;Yao,Y.*Appl. Catal. B: Environ.* **2009**, *87*, 146–151.
7. Zanjanchi, M.A.; Ebrahimian, A.; Arvand, M.*J. Hazard. Mater.* **2010**, *175*, 992–1000.
8. Bıyıklıoglu, Z.; Saka, E.T.; Gökce, S.; Kantekin, H.*J. Mol. Catal. A: Chem*. **2013**, *378*, 156–163.
9. Shukla, P.R.; Wang, S.; Singh,K.; Ang, H.M.; Tadé, M.O.*Appl. Catal. B: Environ.* **2010**, *99*,163–169.
10. Yang, J.; Mu, D.; Gao, Y.; Tan, J.; Lu, A.; Ma, D. *J. Nat. Gas Chem.* **2012**, *21*, 265–269.
11. Jubete , E.; Zelechowska ,K.;. Loaiza, O.A.; Lamas, P.J.; Ochoteco, E. ; Farmer,K.D.; Roberts, K.P.; Biernat, J.F. *Electrochim. Acta* **2011**, *56*, 3988–3995.
12. Lu, W.; Li, N.; Bao, S.; Chen, W.; Yao, Y. *Carbon*, **2011**, *49*, 1699–1709.
13. Shen, C.; Song, S.; Zang, L.; Kang, X.; Wen, Y.; Liu, W.; Fu, L.; *J. Hazard. Mater.* **2010**, *177*, 560–566.
14. Yao. Y.; Huang, Z.; Zheng, B.; Zhu, S.; Lu, W.; Chen. W.; Chen, H. *Curr. Appl. Phys.* **2013**, *13*, 1738–1742.
15. Gao, M.; Lu, W.; Li. N.; Chen, W. *Cellulose*, **2014**, *21*, 2073–2087.

16. Biernacka, I.K.; Raposo, M. M. M.; Batista, R.; Parpot, P.; Biernacki,K.; Magalhaes, A.L.; Fonseca.A. M. ; Neves, I.C. *Microporous Mesoporous Mater.* **2016**, *227*, 272-280.

17. Modi, C.K. ; Trivedi, P. M.; Chudasama, J. A.; Nakum, H.D.; Parmar, D. K.; Gupta, S. K.; Jha, P. K. *Green Chem Lett Rev*. **2014**,*7:3*, 278-287.

18. Hailu, S.L.; Nair, B. U.; Abshiro, M. R.; Aravindhan, R.; Diaz, I.; Tessema,M. *RSC Adv.***2015**, **5**, 88636-88645.

19. Uzunova, E. L.; Mikosch,H. *ACS Catal.* **2013**, *3*, 2759−2767.

20. Bania, K. K, Deka, R. C. *J. Phys. Chem. C.* **2013**, *117*, 11663−11678.

21. Bania, K. K.; Deka, R. C. *J. Phys. Chem. C.* **2012,***116*, 14295−14310.

22. Bania, K. K.; Deka, R. C. *J. Phys. Chem. C.* **2011**, *115*, 9601–9607.

23. Ray, S.; Vasudevan, S. *Inorg. Chem.* **2003**, *42*, 1711-1719.

24. Chan, Y.W.; Wilson, R.B. *Jr., ACS Natl. Meeting*, **1988**, *33*, 453.

25. Seelan, S. ; Agashe, M.S.; Srinivas, D.; Sivasanker, S. *J. Mol. Catal.A: Chem.* **2001**, *168*, 61.

26. Ratnasamy, P.; Raja, R. European Patent, EP 0,784,045 A1.

27. Armengol, E. ; Corma, A. ; Fornés, V.; Garc´ıa, H.; Primo, *J. Appl. Cat.A: Gen*. **1999**, *181*,305.

28. Grootboom, N.; Nyokong, T. *J. Mol. Catal. A: Chem.* **2002**, *179*,113.

29. Kasuga,K.; Tsuboi,K.; Handa,M.; Sugimori,T.; Sogabe, K. *Inorg.Chem. Commun*. **1999**, *21*,507.

30. Jana,S.; Dutta,B..; Bera,R.; Koner,S.; *Langmuir*, **2007**, *23*, 2492-2496

31. Wróblewska,A. ; Fajdek,A. *J. Hazard. Mater.* **2010**, *179*, 258–265.

32. Harvey,L.; Kennedy,E.; DlugogorskiB. Z.; Stockenhuber,M. *Appl. Catal. A: Gen.* **2015**, *489*, 241–246

33. Azarkamanzad, Z.; Farzaneh, F.; Maghami, M.; Simpson, J; Azarkish, M. *Appl.*
Organometal Chem. **2018**, *32*, 4168.

34. Botubol-Ares, J.M.; Hanson, J.R.; Hernández-Galán, R,.;Collado, I. G. *ACS Omega* **2017**, *2*, 3083−3090.

35. Çakıcı, M.; Kılıç,H.; Ulukanlı, S.; Ekinci, D.*Tetrahedron* **2018**, *74*, 49-57.

36. Li, T.; Wang, Z.; Chen, W.; Miras, H. N.; Song, Y.; *Chem. Eur. J.* **2017**, *23*, 1069 – 1077.

37. Li, L.; Niu, Y.; Dong, K.;Ma, P.; Zhang, C.; Niu, J.; Wang, J.*RSC Adv.* **2017**, *7*, 28696–28701.

38. Ma, W.; Chen, C.; Kong, K.; Dong, Q.; Li, K.; Yuan, M.; Li, D.; ,Hou Z.*Chem. Eur.J.***2017**, *23*, 7287 – 7296.

39. Frisch M.J; Gaussian 09, Revision B.01; Gaussian, Inc.: Wallingford, CT, 2010.

40. Becke,A.D. *J. Chem. Phys.***1993,** *98* , 5648.

41. Becke,A.D. *Phys. Rev. A*. **1988**, *38*, 3098.

42. Lee, C.; YangW.;Parr, R.G.*Phys. Rev. B.***1988**, *37*, 785.

43. Stevens, P.J.; Devlin,F.J.; Chabalowski.C.F.;Frisch,M.J. *J. Chem. Phys*. **1994**, *98*, 11623.

44. Hoshino, A.; Takenaka, Y.; Miyaji, H.;*Acta Cryst.* **2003**, *B59*, 393-403.

45. Koopmans,T. A. *Physica,* **1933**, *1*, 104−113.

46. Parr,R.G.; Szentpaly,L.V.; Liu.S. *J. Am. Chem. Soc.***1999**, *121*, 1922−1924.

47. Yang,W.; Mortier,W.J.*J. Am. Chem. Soc*. **1986**, *108*, 5708− 5711.

48. Robertson, J. M. *J. Chem. Soc*. **1935**, 615-621.

49. Chattaraj, P. K.; Liu,G. H. ; Parr,R. G. *Chem. Phys. Lett*. **1995**, *237*, 171−176.

50. Morell,G. ;Labet,V.; Grand,A.; Chermette ,H.*Phys. Chem. Chem.Phys.* **2009**, *11*, 3417−3423.

51. Nguyen, L.T. ; Le, T.N.; De Proft, F.; Chandra,A.K. ; Langenaeker,W.; Nguyen,M.T.; Geerlings, P. *J. Am. Chem. Soc.* **1999**, *121*, 5992.

52. Pal,S.; Chandrakumar,K.R.S. *J. Am. Chem. Soc.* **2000**, *122*, 4145.

53. Chattaraj,P.K.*J. Phys. Chem. A.* **2001**, *105*, 511−513.

54. Bania,K.K.; Karunakar, G.V.; Goutham,K.; Deka, R.C. *Inorg. Chem.* **2013**, *52*, 8017−8029.

55. Decker, A.; Solomon,E.I.; *Curr. Opin. Chem. Biol.* **2005**, *9*, 152.

56. Hamilton, G.A.; Adolf, P.K.; De Jersey,J.; DuBois,G.C.; Dyrkacz,G.R.; Libby, R.D. J. *Am. Chem. Soc.* **1978**, *100*, 1899.

57. Clark, K.; Penner-Hahn, J.E.; Whittaker, M. M.; Whittaker, J. W. *J. Am. Chem. Soc.* **1990,** *112*, 6433.

58. Anamaria, I.; Mot, A. C.; Silaghi-Dumitrescu, R.; *Cent. Eur. J. Chem.* **2012**, *10(5)*, 1527- 1533.

4. Impact of the Zeolite-Y Framework on the Geometry and Reactivity of Ru (III) Benzimidazole Complexes – A DFT Study

4.0 Abstract

A detailed comparative density functional theory (DFT) study is made to understand the structural changes of the guest complex due to steric and electronic interactions with the host framework. In this study, ruthenium(III)benzimidazole and 2-ethyl ruthenium(III)benzimidazole complexes encapsulated in a supercage of zeolite Y. The zeolitic framework integrity is not disturbed by the intrusion of the large guest complex. A blue shift in the d–d transition observed in the UV-Visible spectroscopic studies of the zeolite encapsulated complexes and they show a higher catalytic efficiency. Encapsulation into zeolite matrix makes the metal center more viable to nucleophilic attack and favors the phenol oxidation reaction. Based on the theoretical calculations, transition states and structures of reaction intermediates involved in the catalytic cycles are derived.

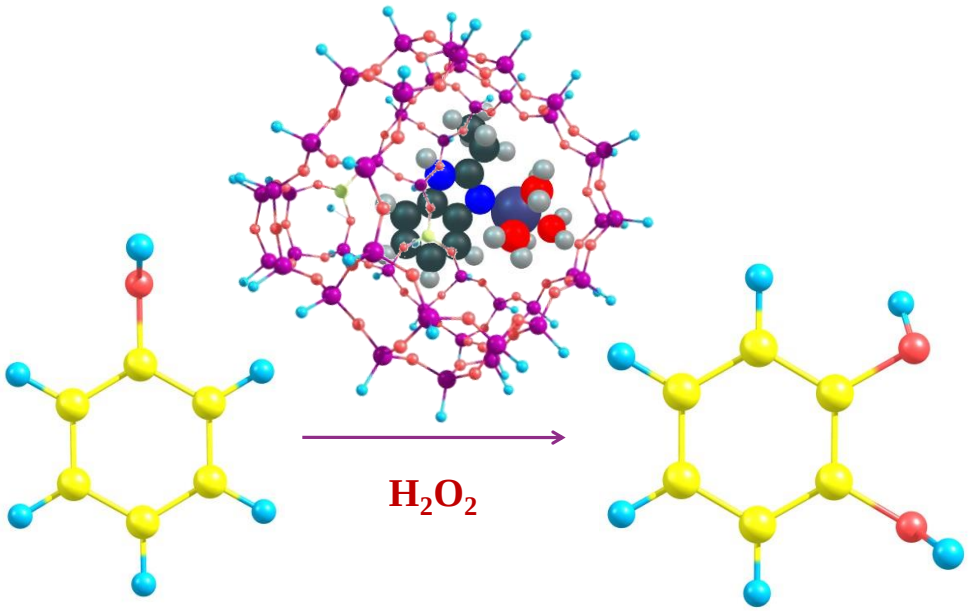

4.1 Introduction

The transition metal complexes of benzimidazole derivatives have been a matter of constant discussion over the past few decades because of the important catalytic properties of those materials. The material also behaves as a natural mimic and therefore has a relevance in the area of pharmacology as an antioxidant, antimicrobial, anthelmintic, anticancer, anti-inflammatory, antihypertensive, and analgesic activities.[1-9] The biological role of complexes containing an imidazole ring system has a direct connection with the characteristics of the two N atoms in the system. The deprotonated N atom could coordinate with a transition metal ion, and the protonated N atom involves in hydrogen bonding.[10-18] Benzimidazole and imidazoles moieties have extensively studied in the literature as models of biologically relevant molecules present in vitamin B12 and several metalloproteins. In most of the cases, the transition metal complexes of biologically relevant ligands are more efficient than the free ligands.[19, 20] Even though intensive studies are available on the zeolite encapsulated transition metals: very few reports are on ruthenium complexes. Ruthenium complexes with imidazole ligands are of substantial interest because of their antitumor activities.[21, 22] The encapsulation of these complexes on a host molecule makes it as heterogeneous catalysts for oxidation and epoxidation reactions. Zeolite-Y encapsulated imidazole complexes have a functional similarity with cytochrome P-450. This enables the use of zeolite-Y as biomimetic systems.[23, 24] The walls of zeolite framework influence the geometry, and physicochemical properties (magnetic, electronic, and redox) of the guest encapsulated complex. Thus, the topology (voids and steric/electrostatic constraints of walls) of the host zeolite-Y matrix controls the reactivity and selectivity of the guest species. Several works have focused on the geometrical and reactivity aspects of various complexes encapsulated into zeolite-Y matrix.[25-33]

Zeolite encapsulated transition metal imidazole and benzimidazole complexes normally used as an oxidant for organic substrates such as phenol, benzyl alcohol, ethylbenzene, benzoin, and cyclohexanol. The role of transition metal centers and its preferred location in the complexes and the reaction mechanism became a challenge for theoretical studies. This chapter deals with density functional theory studies on zeolite-Y encapsulated ruthenium(III) with benzimidazole and 2-ethyl benzimidazole.

4.2 Computational Methods

All the density functional calculations were done using the Gaussian 09 program. For calculations, Becke's three-parameter exchange Lee, Yang and Parr correlation hybrid functional (B3LYP) and an effective core potential basis set LanL2DZ were employed.[34, 35] Zeolite frameworks were generated using 40 tetrahedral units (40T), where hydrogen atoms saturate the supercage structure. Initially, crystallographic positions of Si and O atoms were fixed and the positions of terminal hydrogen atoms are optimized. To generate three negative charges in the six-membered ring, as per Lowenstein's rule, three silicon atoms replaced with three aluminium atoms. Then, neat optimized ruthenium(III) complex was encapsulated inside the zeolite framework. All geometric optimizations performed without point group constraints. Three positive charges of the complexes compensate the three negative charges generated in the cluster.

Koopmans theorem[36] gives the chemical potential (μ) and global hardness (η) of a system of complexes and it could express as

$$\mu = \frac{E_{LUMO} + E_{HOMO}}{2} \quad (1)$$

$$\eta = \frac{E_{LUMO} - E_{HOMO}}{2} \quad (2)$$

Here, E_{LUMO} and E_{HOMO} represent the lowest unoccupied molecular orbital energy and highest occupied molecular orbital energy respectively.

The global electrophilicity as presented by Parr *et al* [37] can be defined as

$$\omega = \frac{\mu^2}{2\eta} \quad (3)$$

The inverse of the global hardness (η) is the global softness (S)

$$S = {}^{1}/_{2\eta} \quad (4)$$

Time-dependent DFT (TD-DFT) calculations were performed at B3LYP/LANL2DZ level from the optimized ground state geometry. 150 excitation energies are computed. Calculation of UV-Vis spectra was accomplished using GaussSum 2.0.[38] The intra-molecular interaction in the complexes has been analyzed via the natural bond orbital analysis (NBO). Transition state was confirmed by analysis of first frequency which has a negative value which corresponds to the imaginary frequency. TS1, TS2 and TS3 transition states showed only a single imaginary frequency corresponding to the eigenvector along the reaction path.

4.3 Results and Discussion

4.3.1 Ground-State Geometries

In the present work, all the calculations were done using the Gaussian 09 program package with the use of the Gauss view visualization program. The geometry of the complexes was optimized using Becke's three-parameter exchange, Lee, Yang, and Parr correlation (B3LYP) hybrid functional with LanL2DZ basis set. The vibrational frequency analysis of the optimized geometry shows all real frequencies and it is confirmed that the optimized geometry corresponded to the minimum potential

energy surface. The optimized structures of the neat and encapsulated form of the complexes have been shown in Figure 3.1.

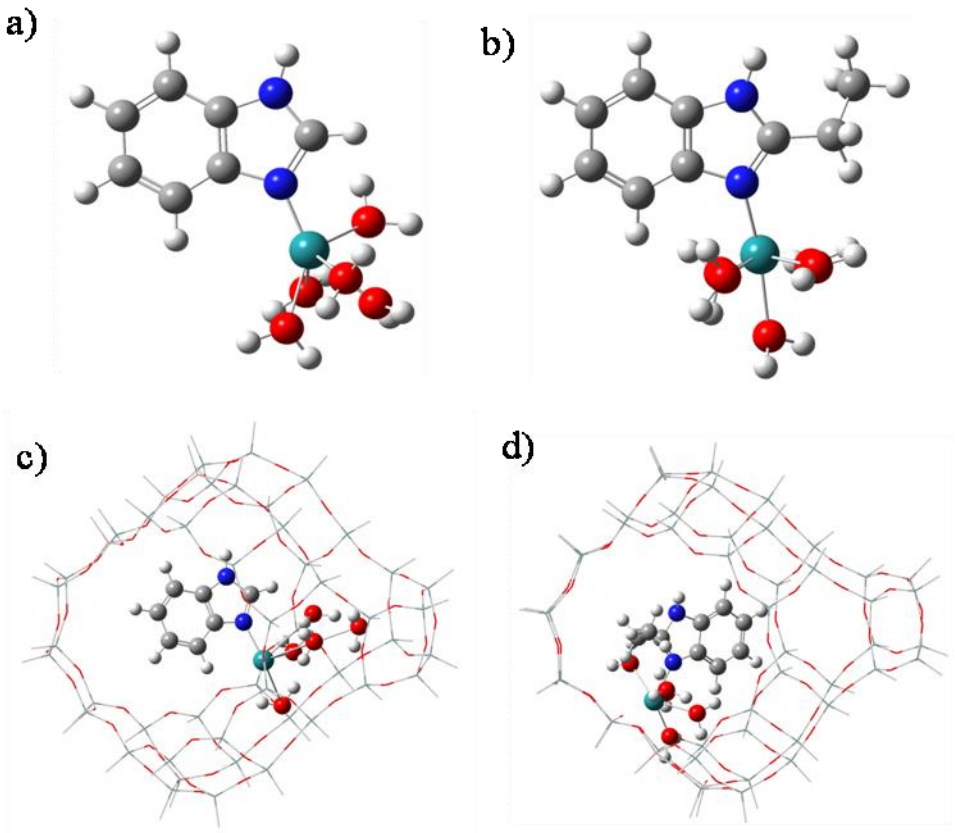

Figure 4.1 Optimized structures of a) RuBzl, b) Ru-2-EtBzl, c) RuBzl –Y and d) Ru-2-EtBzl-Y complexes

The selected geometric parameters of the optimized neat complex and the zeolite encapsulated complex from LanL2DZ level calculations are provided in Table 3.1. The geometrical parameters such as bond length and bond angles of the neat complex have been compared with those of encapsulated complexes. The bond length between ruthenium and metal nitrogen is 2.07 and 2.06Å. While encapsulating, this bond length is decreased by 0.04 and 0.02Å. Ethyl substituted ruthenium complexes show shorter bond length because the ethyl group donates the electron density to the metal centre. Similarly, bond angle also varies. The variation in the bond distances and

bond angles on encapsulation is due to the influence of the zeolite framework; here the topology of the supercage is expected to impose steric constraints on the complex.

Table 4.1 Geometrical parameters of the neat and encapsulated complexes

Complex	**Bond Length (in Å)**	**Bond Angle (in deg)**	
	N – Ru	C1∠N∠Ru	C2∠N∠Ru
RuBzl	2.07	121.7	132.5
Ru-2-EtBzl	2.06	129.5	124.9
RuBzl-Y	2.03	138.2	114.0
Ru-2-EtBzl-Y	2.04	125.6	128.2

4.3.2 Frontier Molecular Orbital Analysis

The HOMO and LUMO energies of neat and encapsulated complexes are represented in Figure 3.2. The HOMO energies are in the order of RuBzl < Ru-2-EtBzl < RuBzl-Y < Ru-2-EtBzl-Y and those of LUMOs are in the order of RuBzl < Ru-2-EtBzl < Ru-2-EtBzl-Y< RuBzl-Y. It can be observed from Figure 3.2 that the HOMO and LUMO energies of these complexes become destabilized in comparison to the neat complexes. Upon encapsulation of the metal complexes, the energies of the frontier orbital get lifted up, leading to a small HOMO-LUMO gap. The change in the energies of the frontier orbitals may be either due to the effect of the counterion or due to the steric constraint imparted by the zeolite matrix. The partial ionic character of the zeolite lattice causes a Coulombic effect by the charge distribution along the framework. This charge distribution produces a strong Coulombic field in the cavities, which might change the energy level of the transition metal complexes which is further supported by TD-DFT studies.

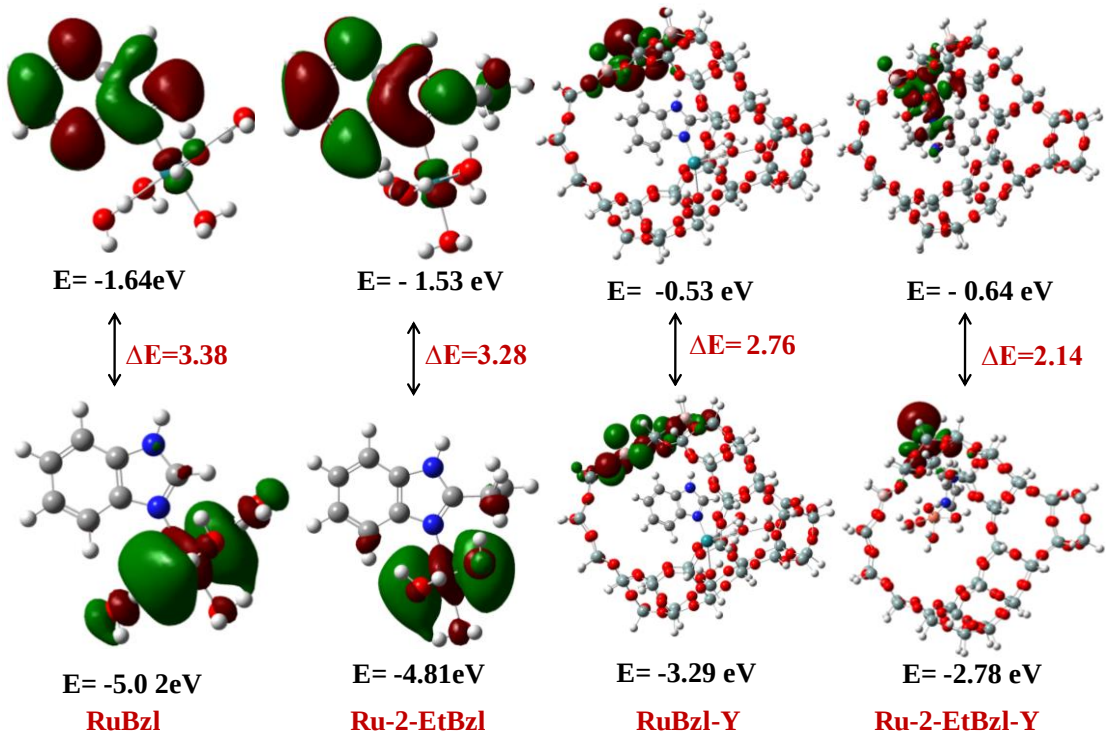

Figure 4.2 Pictorial representation of the HOMO and LUMO level of the neat and the encapsulated complexes

The percentage orbital contribution of each atomic orbital to HOMO and LUMO are given in Table 3.2 and 3.3. The main contribution for RuBzl to HOMO is from s (24%), and d (76%) orbital of ruthenium and LUMO is only from p orbital of carbons. Similarly, for Ru-2-EtBzl, HOMO is contributed by the s and d orbital of ruthenium and LUMO is contributed by the p orbital of carbons. After encapsulation, the main contribution for RuBzl to HOMO is from s orbital of aluminum, p orbital of oxygen of the zeolite matrix. The contribution to LUMO is mainly from d orbital of ruthenium. In the case of Ru-2-EtBzl-Y encapsulated complex the HOMO is shared by the s orbital of ruthenium and zeolite aluminium and hydrogen. It indicates that the molecular orbital of the metal complex restricts within the dimension and cannot extend over the entire space of the zeolite cage. The HOMO and LUMO level of complexes get stabilized upon substitution of aluminum in the zeolite matrix. The interaction

energy is calculated at the same level of theory are found to be in the order of RuBzl-Y (32.83 eV) > Ru-2-EtBzl-Y (28.02 eV). The interaction energies calculated shows that the RuBzl-Y has stronger interaction than Ru-2-EtBzl-Y and becomes more stabilized compared to Ru-2-EtBzl-Y. These differences in the interaction energy bring a considerable change in the geometrical parameters and the energies of the HOMO and the LUMO levels.

Table 4.2 Orbital contributions (in %) to HOMO and LUMO for the neat complexes

Complex		**Ru**		**C1**	**C3**	**C6**	**C8**
		s	**d**	**p**	**p**	**p**	**p**
RuBzl	HOMO	24	76				
	LUMO			16	28	24	32
Ru-2-EtBzl	HOMO	19	81				
	LUMO			15	33	30	22

Table 4.3 Orbital contributions (in %) to HOMO and LUMO for the encapsulated complexes

Complex		**$Ru_{complex}$**		**$Al_{zeolite}$**	**$O_{zeolite}$**	**$H_{zeolite}$**
		s	**d**	**s**	**p**	**s**
RuBzl-Y	HOMO			49	51	
	LUMO		100			
Ru-2-EtBzl-Y	HOMO	15		20		65
	LUMO		100			

4.3.3 Optical Transitions from TD-DFT Studies

Table 4.4 Important d–d transitions, energies, extinction coefficients and band assignments for neat and the encapsulated complexes

Complex	λ_{max}(nm)	F	E(eV)	Major Contributions
RuBzl	527	0.0291	2.3525	H-3→L+1 (26%), HOMO→L+1 (42%)
	618	0.0043	2.0058	HOMO→LUMO (92%)
Ru-2-EtBzl	534	0.0083	2.3212	HOMO→L+3(22%), HOMO→L+6 (18%)
	669	0.0199	1.8515	H-3→LUMO (82%)
RuBzl-Y	598	0.0012	2.0728	H-2→LUMO (43%)
	641	0.0001	1.9323	H-1→LUMO(95%)
Ru-2-EtBzl-Y	583	0.0004	2.1243	HOMO→L+3 (99%)
	652	0.0004	1.8988	H-2→LUMO (53%)

TD-DFT methods employed to calculate the UV-Vis spectra for the neat complexes and encapsulated complexes. The d–d transitions calculated with the corresponding oscillator strengths, energies and assignments for all the complexes tabulated in Table 3.4. The encapsulated complex shows a weak band because of the metal-centered d–d transitions in the visible range at 450–800 nm. The absorption spectrum of RuBzl-Y and Ru-2-EtBzl-Y shows two absorption bands at 598 and 641nm and 583 and 652 nm respectively due to $2T_{2g} \rightarrow 2_{Eg}$ and $2T_{2g} \rightarrow 2A_{2g}$ transitions of the octahedral low spin d^5 system and is an indicator of the octahedral environment around ruthenium(III) ion reported by Bhagya *et al*.[39,40]

In the case of neat RuBzl complex, the first d–d transition is calculated at 527 nm, a transition primarily from the H-3→L+1, HOMO→L+1. The transition around 618 nm occurring from HOMO→LUMO is another significant d–d transition.

Ru-2-EtBzl shows two d-d transitions at 534 and 669 nm due HOMO→L+3, HOMO→L+6 and H-3→LUMO transitions. For the encapsulated RuBzl complex, the d–d transition appears at 598 nm which is a transition from H-2→LUMO orbitals and the transition around 641 nm is from H-1→LUMO is also a d–d transition. The Ru-2-EtBzl-Y complex shows the d–d transition at 583 and 652 nm which is a transition from HOMO→L+3 orbitals and H-2→LUMO. The presence of ethyl group indirectly alters the electronic environment around it. The transitions shifted to longer wavelengths and this indicates the ethyl group in the ligand has a drastic effect. Even though the d–d transitions are difficult to identify in the case of encapsulated complexes, due to the increased hybridization of ligand pi orbitals with the metal d orbitals, it has been carefully tried to assign few critical transitions. From these studies, it is evident that the d–d transition is shifted to lower wavelengths for encapsulated complexes after encapsulation which in accordance with the frontier molecular orbital analysis.

4.3.4. Global and Local Descriptors

The DFT-based global descriptors such as chemical hardness (η), the chemical potential (μ), electrophilicity index (ω), and softness (S) have calculated using a B3LYP functional with LanL2DZ basis set for the neat and encapsulated complexes and the values are given in Table 3.5. The maximum hardness principle (MHP) [41,42] states that most stable structure has the maximum hardness. Thus, the neat complexes with the maximum hardness are chemically more stable compared to the encapsulated complexes. Further, Table 3 reveals that on encapsulation the chemical potential (μ) values increase and that of electrophilicity index (ω) decreases. This result indicates that the occupancy of the electron would bring out a substantial change in the reactivity of the system. In this context, it is appropriate to mention that electrophilicity containing information of both electron transfer (chemical potential) and stability

(hardness) could consider being a better descriptor of the global chemical reactivity. Moreover, ω includes a hardness term in the denominator, which is a descriptor of the stability. The electrophilicity is expected to exhibit an inverse linear relationship with hardness, or in correlation with MHP, we can say that under the conditions for the existence of an MHP, there will also be a minimum electrophilicity principle.[43] Thus, an increase in the chemical potential (μ) and global softness (S) values and a decrease in the hardness (η) had observed when the complexes encapsulated into the zeolite framework. The changes in the values of the global descriptors reflect the effect of the zeolite matrix on their activity of the complexes and indicate that complexes with high μ values can actively participate in electron transfer reactions. The encapsulated complex with a minimum value of electrophilicity (ω) and chemical potential (μ) is more reactive than neat complex with a maximum value of ω, and highest value of μ. Therefore, the neat complex with the maximum hardness is more stable on the encapsulated one and Ru-2-EtBzl-Y complex with minimum η and maximum S values would be the most reactive system.

Table 4.5 Hardness (η, in eV), Chemical potential (μ, in eV), Electrophilicity index (ω, in eV), and Global softness (S, in eV)

Complex	**μ**	**H**	**ω**	**S**
RuBzl	-3.33	1.69	3.280	0.295
Ru-2-EtBzl	-3.17	1.64	3.063	0.304
RuBzl-Y	-1.91	1.38	1.321	0.362
Ru-2-EtBzl-Y	-1.71	1.07	1.366	0.467

4.3.5 Natural Bond Order Analysis

NBO analysis is done to capture intramolecular interactions between filled and vacant orbitals to determine the delocalization. Natural bond order analysis has

performed at B3LYP/6-31G(d,p) to gain further insight into various second-order interactions between filled and vacant orbitals, which is a direct measure of intramolecular delocalization. The second-order perturbation energy analysis has been carried out to evaluate the donor-acceptor interactions on NBO basis and the results are summarized in Table 3.6 and the pictorial representation of π →π* and n→π* interactions shown in Figure 3.3. The computed second-order perturbation analysis shows that the intramolecular hyper conjugative interactions produced by the orbital overlap between π and π*, n and π*, which causes stabilization of the molecules. Moreover, the n→ π* interactions are predominant in encapsulated complexes, whereas π → π* interactions favored in neat complexes. The π→ π* interaction occurs between the filled orbital of carbon and an empty orbital of carbon and nitrogen. The n→ π* interaction occurs between the filled carbon orbital, lone pair of nitrogen and an empty orbital of carbon and nitrogen.

Table 4.6 Second order perturbation theory analysis from NBO analysis obtained at B3LYP/LanL2DZ level

Complex	**Filled NBO**	**Empty NBO**	**E(2) [kcal/mol]**
RuBzl	π(C_1-C_6)	π*(C_4-C_5)	21.61
	π(C_2-C_3)	π*(C_1-C_6)	23.03
	n(N_9)	π*(C_4-C_5)	33.40
	n(N_9)	π*(N_7-C_8)	54.50
Ru-2-EtBzl	π(C_1-C_6)	π*(C_5-N_9)	37.12
	π(C_5-N_9)	π*(N_7-C_8)	28.77
	n(C_4)	π*(C_2-C_3)	67.20
	n(C_4)	π*(C_5-N_9)	278.72
RuBzl-Y	π(C_{173}-N_{177})	π*(N_{175}-C_{176})	29.67
	n(C_{172})	π*(N_{175}-C_{176})	73.41
	n(C_{174})	π*(C_{173}-N_{177})	317.79

Ru-2-EtBzl-Y	$\pi(C_{173}\text{-}N_{177})$	$\pi^*(N_{175}\text{-}C_{176})$	28.97
	$n(C_{172})$	$\pi^*(C_{173}\text{-}N_{177})$	273.12
	$n(C_{174})$	$\pi^*(C_{173}\text{-}N_{177})$	290.95

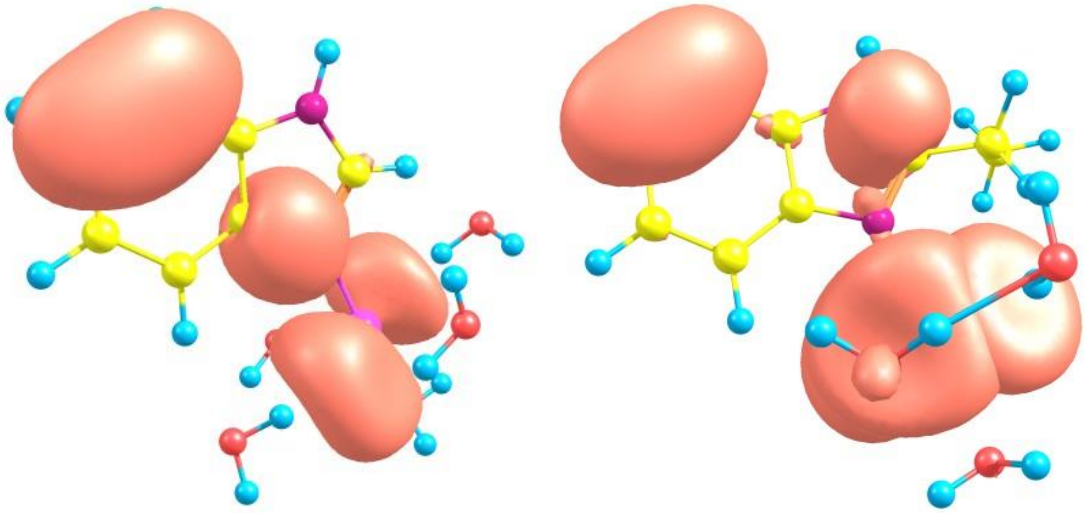

Figure 4.3 Pictorial representation of $\pi \rightarrow \pi^*$ and $n \rightarrow \pi^*$ interactions

4.3.6 Mechanism of Phenol Oxidation

A possible mechanism for the conversion of phenol to catechol catalyzed by ruthenium(III)benzimidazole complex in the presence of H_2O_2 shown in Scheme 1. Starting from the RuBzl and RuBzl-Y complexes, hydrogen peroxide was introduced, which immediately leads to the formation of a weakly bound van der Waals complexes (RuBzl).H_2O_2 and (RuBzl-Y).H_2O_2 through TS1 (RuBzl (-20.18 cm^{-1}) and RuBzl-Y (-32.51 cm^{-1})). This step has a barrier (ΔE) of 19.6 and 15.5 kcal/mol for RuBzl and RuBzl-Y respectively. At TS1, one of the hydrogen atoms of H_2O_2 moves toward the metal center. The M···O distances are found to be 4.57 and 3.52 Å and the O···H distances are 3.35 and 2.69 Å for RuBzl and RuBzl-Y. The optimized geometries of the intermediate states show that the weakly bound species complexes formed via the interaction of the metal center with one of the peroxide oxygen moiety. The M···O distances are found to be 3.12 and 2.89 Å and the O···H distances are 2.91 and 2.12 Å

for RuBzl and RuBzl-Y. Upon phenol addition into the metal peroxide complex, the H_2O_2 moves away from benzimidazole ligand and facilitates the formation of Ru−O (phenyl) linkage. The former step proceeds through TS2 (RuBzl (-29.21 cm^{-1}) and RuBzl-Y (-41.24 cm^{-1})) in RuBzl and RuBzl-Y which have to cross the energy barrier of 16.3 and 14.3 kcal/mol respectively.

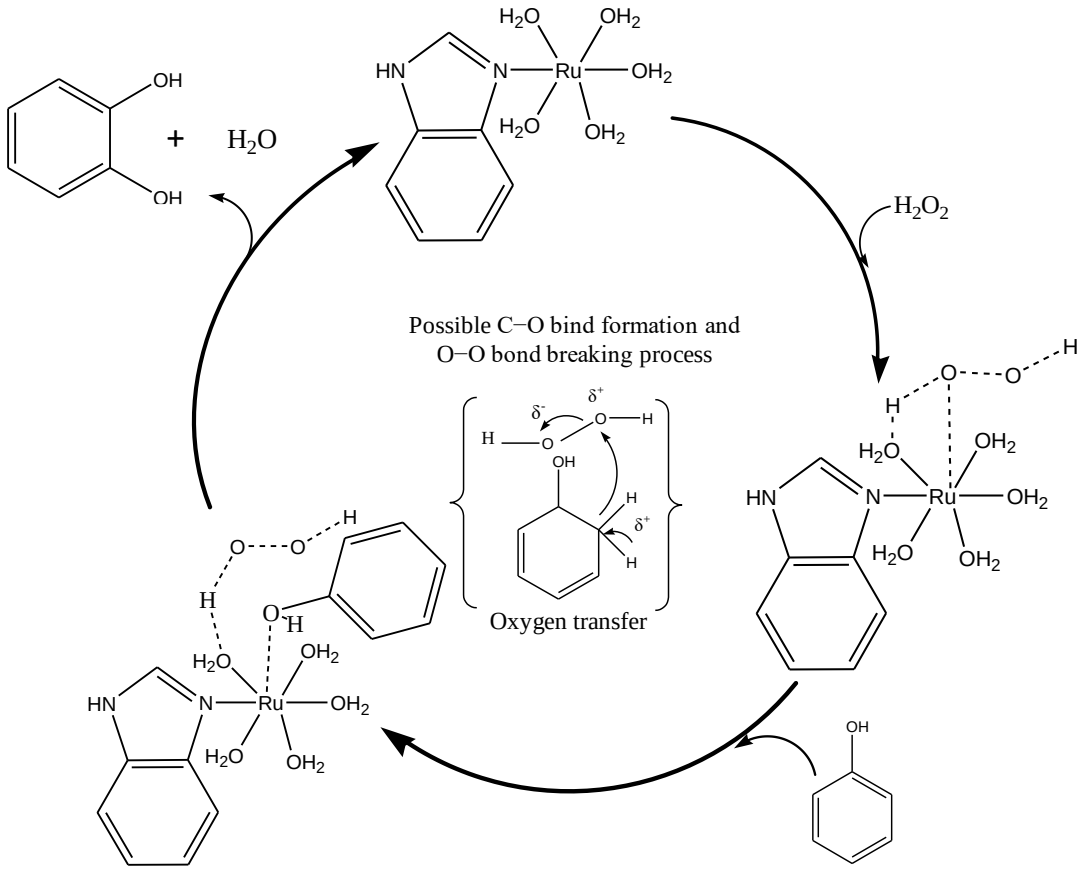

Scheme 1. A Possible catalytic cycle for conversion of phenol to catechol in the presence of RuBzl complex and H_2O_2

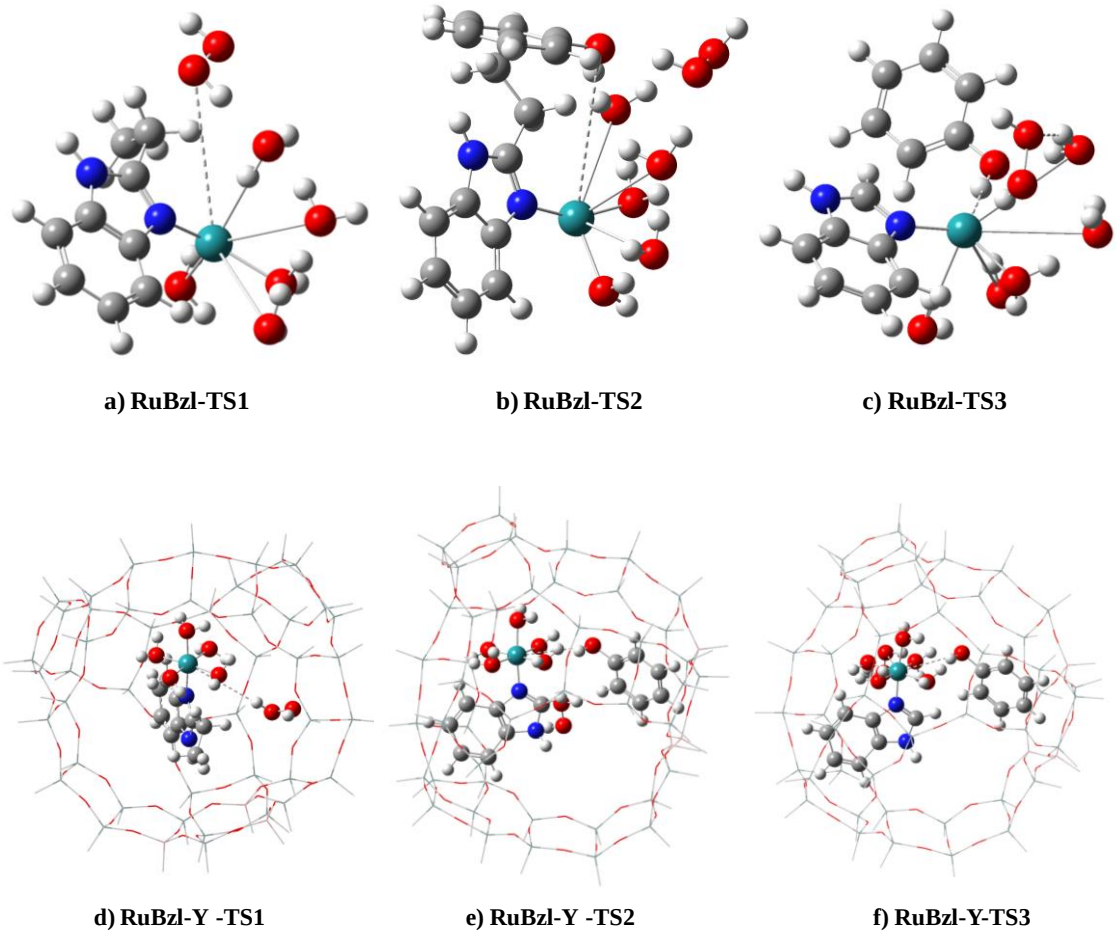

Figure 4.4 The possible transition states involved in the conversion of phenol to catechol

The final step of the mechanism involves the transfer of oxygen from peroxide to phenol (TS3) (RuBzl (-36.53 cm^{-1}) and RuBzl-Y (-54.35 cm^{-1})) leads to the formation of catechol and liberation of water and subsequent regeneration of the ruthenium(III)benzimidazole complex. The last step of the mechanism is a C−H bond activation process taking place by the transfer of oxygen from hydrogen peroxide to phenol and is the rate-determining step. This process proceeds via an intermolecular oxidation-reduction reaction between the substrate phenol and H_2O_2. Homolytic breakage results in rapid dissociation to give catechol, regenerating the complex in the catalytic cycle. A similar kind of mechanism has been recently proposed by Deka *et*

al.[30] These differences in the energy barrier bring significant changes in the catalytic activity of the metal complexes which indicates that the energy barrier is further lowered on encapsulation, leading to the high reactivity of the encapsulated complexes in comparison to the neat complexes.

4.4 Conclusion

This chapter presented DFT and TD-DFT studies of RuBzl and Ru-2-EtBzl complexes in the free state and encapsulated in zeolite-Y. The focus is on the influence of the topology of the pores of the host on the geometry adopted by complex on encapsulation. The electronic spectrum of the zeolite-Y encapsulated RuBzl, and Ru-2-EtBzl complex shows that charge transfer and d–d bands are mainly intensified and blue shifted. The affected transitions indicate that the complex has undergone significant distortion in geometry. All these theoretical observations establish that the topology of the zeolite supercage has a pronounced effect on the structure of the complex. The complex has undergone a distortion to fit into the cavity. As a result, the HOMO-LUMO energy gap diminished and the complexes encapsulated inside zeolite-Y are found to be better catalysts regarding stability and catalytic efficiency. DFT calculation predicts that encapsulation reduces the global hardness and increases the softness values of the complexes, resulting in a higher catalytic ability. A plausible catalytic cycle proposed for phenol oxidation based on the DFT calculation.

References

1. Kus. C.; Kilcigil, G. A.; Eke, B. C.; Iscan, M. *Arch. Pharm .Res*. **2004**, *27*, 156.
2. Goker, H.; Kus, C.; Boykin, D.W.; Yildiz, S.; *Altanlar, N. Bioorg. Med .Chem.* **2002**, *10*, 2589.
3. Pawar, N. S.; Dalal, D. S.; Shimpi, S. R.; Mahulikar, P. P . *Eur. J. Pharm. Sci.* **2004**, *21*, 115.

4. Mavrova, A. T.; Denkova, P. S.; Tsenov, Y. A.; Anichina, K. K.; Vutchev, D. L. *Bioorg. Med. Chem*. **2007**, *15*, 6291.

5. Starcevic, K.; Kralj, M.; Ester, K.; Sabol, I.; Grace, M.; Pavelic, K.; Zamola, G. K. *Bioorg. Med. Chem.* **2007**, *15*, 4419.

6. Jat, R. K.; Jat, J. L.; Pathak, D. P. *Eur. J. Chem*. **2006**, *3*, 278.

7. Lazer, E. S.; Matteo, M. R.; Possanza, G. J. *J. Med. Chem.* **1987**, *30*, 726.

8. Ito, K.; Kagaya, H.; Fukuda, T.; Yoshino, K.; Nose, T. *A. Forsch. Drug. Res*. **1982**, *32*, 49.

9. Vazquez, G. N.; Cedilla, R.; Campos, A. H.; Yepez, A.; Luis, F. H.; Valdez, J.; Morales, R.; Coetes. R.; Hernandez, M.; Castllo, R.; *Bioorg. Med. Chem.* **2001**, *11*, 187.

10. Santoro, A.; Mighell, A. D.; Zocchi, M.; Reimann, C. W. *Acta. Crystr*. **1969**, B25: 842.

11. Reimann, C. W.; Santoro, A.; Mighell, A. D. Acta. Cryst. **1970**, B26:521.

12. Ivarsson, G, J, M.; Forsling, W. *Acta. Cryst.* **1979**, B35:1896.

13. Lambert , F.; Renault , J. P.; Policar, C.; Badarau, I. M.; Cesario, M.; *Chem. Commun.* **2000**, 35.

14. Shiu, K.B.; Yen, C.H.; Liao, F. L.; Wang, S. L. *Acta. Cryst.* **2003**, E59:1189.

15. Masciocchi, N.; Ardizzoia ,G. A.; Brenna, S.; Castelli, F.; Galli, S.; Maspero, A.; Sironi, A.; *Chem. Commun.* **2003**, 2018.

16. Huang, X. C.; Zhang, J. P.; Lin, Y. Y.; Yu, X. L.; Chen, X. M. *Chem. Commun.* **2004**,1100.

17. Abuskhuna, S.; McCann, M.; Briody, J.; Devereux, M.; McKee, V. *Polyhedron* **2004**, *23*, 1731.

18. Gong, Y.; Hu, C.; Li, H.; Pan, W.; Niu, X.; Pu, Z. *J. Mol.Struct*. **2005**, 740, 153.

19. Kuzmonovic, S. O. P.; Leovac, L. M.; Janjic, N. U. P.; Rogan, J.; Balaz, J. *J. Serb. Chem. Soc.* **1999**, *64*, 381.

20. Ahuja, I. S.; Prasad, I. *Inorg Nucl Chem Lett* . **1976**, *12*, 777.

21. Clarke, M.J. Ruthenium and Other Non-Platinum Metal Complexes in Cancer Chemotherapy (Springer-Verla, Heidelberg, Germany, 1989).

22. Keppler, B.K. Metal Complexes in Cancer Chemotherapy (VCH, Weinheim, Germany, 1993).

23. Choudhary, A.; Das, B.; Ray, S. *Dalton Trans.* **2016, *45,*** 18967.

24. Parton, R. F.; Vankelecom, I. F. J.; Casselman, M. J. A.; Bezoukhanova, C.P.; Uytterhoeven, J. B.; Jacobs, P.A. *Nature* **1994,** *370*,541.

25. Biernacka, I.K.; Raposo, M. M. M.; Batista, R.; Parpot, P.; Biernacki, K.; Magalhaes, A. L.; Fonseca, A. M.; Neves, I. C. *Microporous. Mesoporous. Mater*. **2016**, *227*, 272.

26. Modi, C. K.; Trivedi, P. M.; Chudasama, J.A.; Nakum, H. D.; Parmar, D. K.; Gupta, S. K.; Jha, P. K. *Green Chem. Let.t Rev.* **2014** ,*7*, 278.

27. Hailu, S. L.; Nair, B. U.; Abshiro, M. R.; Aravindhan, R.; Diaz, I.; Tessema, M.; RSC *Adv*, **2015**, *5*,88636.

28. Mohan, S.; Bhattacharjee, D.; Deka, R. C.; Jothivenkatachalam. K. *RSC Adv.* **2016**, *6*,71214.

29. Uzunova, E. L.; Mikosch, H. *ACS Catal.* **2013**, *3*, 2759.

30. Bania, K, K.; Deka, R. C. *J. Phys. Chem. C* **2013**, *117*,11663.

31. Bania, K. K.; Deka, R. C. *J. Phys. Chem. C* **2012,** *116*, 14295.

32. Bania, K.K.; Deka, R. C. *J. Phys. Chem. C* **2011**, *11*, 9601.

33. Ray, S.; Vasudevan, S.; Inorg. Chem. **2003**, *42*,1711.

34. Frisch, M.J. Gaussian 09, Revision B.01; Gaussian, Inc (Wallingford, CT, 2010).

35. Gorelsky, S.I.; Lever, A.B. P. *J. Organomet. Chem.* **2001**, *635*,187.

36. Parr, R. G.; Szentpaly, L.V.; Liu, S. *J. Am. Chem. Soc.* **1999**, *121*,1922.

37. Yang, W.; Mortier, W.J. *J. Am. Chem. Soc*. **1986**, *108*, 5708.

38. Jenkins, D. M.; Bernhard, S. *Inorg. Chem.* **2010**, *49*, 24.

39. Bhagya, K. N.; Gayathri, V. *J. Porous. Mater*. **2014**, *21*,197.

40. Lever, A.B.P. Inorganic electronic spectroscopy, 2nd edn. (Elsevier, Amsterdam, 1984).

41. Parr, R.G.; Chattaraj ,P.K. *J. Am. Chem. Soc.***1991**, *113*, 1854.

42. Chattaraj, P. K.; Liu, G. H.; Parr, R. G. *Chem. Phys. Lett*. **1995**, *237*, 171.

43. Morell, G.; Labet, V.; Granda, A.; Chermette, H. *Phys. Chem. Chem. Phys.* **2009,** *11*, 3417.

5. Formation of 3-buten-1-ol over Metal Encapsulated ZSM-5 from Formaldehyde and Propene: A Density Functional Theory Study

5.0 Abstract

Carbonyl-ene reaction, which involves C-C bond formation, is an essential organic reaction. Here, we explained the possibility of the C-C bond formation between formaldehyde and propene catalyzed with Ni^{2+}, Pd^{2+}, and Pt^{2+} exchanged on ZSM-5 zeolite (metal-ZSM-5) by density functional theory. Pt exchanged ZSM-5 exhibits a better activity than other metal-ZSM-5 reported in the present work due to high charge transfer among the platinum and formaldehyde.

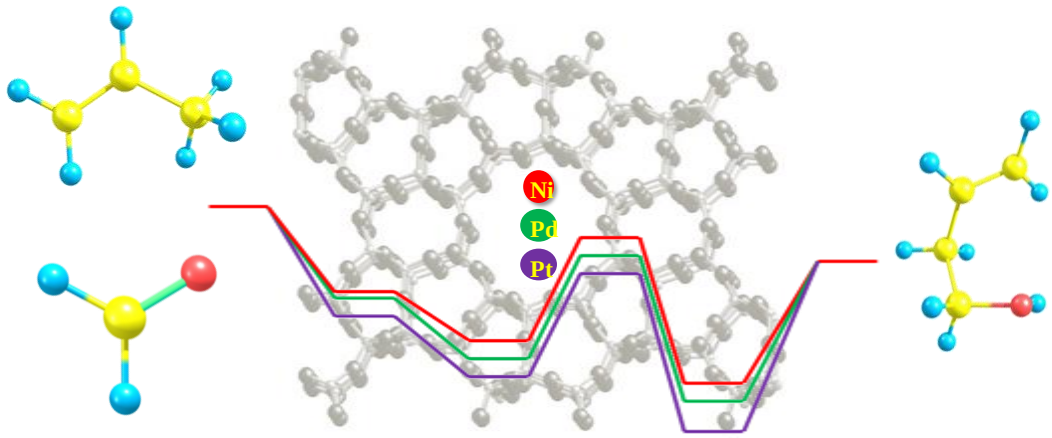

5.1 Introduction

The carbonyl-ene reaction is one of the crucial reactions in the chemical process, which involves the carbon-carbon bond formation. It is an enantioselective reaction which occurs between a carbonyl compound and allylic hydrogen which is present in the alkene. Lewis acids used as the catalyst for these reactions and it requires strong electrophilic carbonyl compounds. The product, 3-buten-1-ol is used to produce polypropylene from propylene copolymerization. This reaction also involves in

tetrahydrofuran synthesis, but it has two disadvantages, (i) low boiling point of formaldehyde (-19.5°C) makes it complicated to handle and (ii) rapid polymerization into trioxane and paraformaldehyde solid which makes its lifetime is relatively short. To preserve formaldehyde in monomer form, it has to be depolymerized by Lewis acid. However, formaldehyde requires more attention in its handling as it is corrosive and causes toxic waste problems, making environmentally frosty.[1-20] To overcome this problem discovering an appropriate storage material for maintaining formaldehyde in monomer form is important. Considering these issues, the proposal for new storage materials is an urgent need.

Materials like zeolites and metal organic frameworks (MOF) which are widely used for gas storage applications can be the suitable candidate for formaldehyde storage. Many researchers theoretically demonstrated the utilization of MOF-11, alkaline-exchanged and metal-exchanged faujasite zeolite as a formaldehyde storage material.[21-25] Here, we theoretically demonstrated formaldehyde-propene carbonyl-ene reaction on M-ZSM-5 zeolite (M- ZSM-5, M = Ni, Pd, and Pt) using density functional theory with the B3LYP functional. This work investigates the opportunity of using group 10 metal-exchanged zeolites as catalysts for the above reaction.

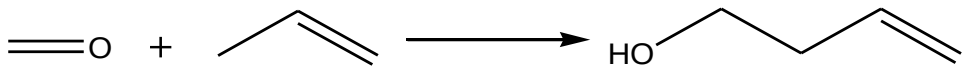

Scheme 1. Carbonyl-ene reaction scheme between formaldehyde and propene

5.2 Computational Methods

All the density functional calculations are done by using G09 program with B3LYP correlation functional using LANL2DZ basis set.[26-28] Formaldehyde-propene reaction over M/ZSM-5 zeolite was studied using $MAl_2Si_6O_9H_{14}$ cluster model, which represent two contiguous five-membered rings from the straight channel of ZSM-5

zeolite wall. Aluminium atoms were positioned in T12 and T6 lattice location for the modeling of a conventional ion exchange site. The distance between two aluminum ions was equal to 4.76 Å for the cluster model. The Si-O bonds are saturated by using hydrogen atoms. The X-ray diffraction data of ZSM-5 zeolite is taken for calculations.[29] Transition states are confirmed by one imaginary frequency.[30, 31] The charge distributions and population analyses done by natural bond orbital analysis (NBO).[32, 33]

5.3 Results and Discussion

Quantum chemical calculations for extrapolating the reaction mechanism are shown in scheme 1. The electronic behavior of the reactive site is influenced by a small fraction of the zeolite framework. The geometries and reaction path of the encapsulated formaldehyde on metal-ZSM-5 for carbonyl-ene reaction were investigated. The reaction is assumed to proceed on a concerted mechanism in which both reactants are involved in the rate-limiting step.

5.3.1 Geometry and Adsorption of the Formaldehyde

The optimized geometry of Ni-ZSM-5, Pd-ZSM-5, and Pt-ZSM-5 are illustrated in Figure 5.1. The metals are located in the five-membered ring plane. The adsorption energies are found to be -18.2, -18.8, and -38.3 kcal/mol for Ni-, Pd-, and Pt-ZSM-5, respectively. The geometrical parameters of all the states are tabulated in Table 5.1. The values at column 1 and 2 describe the metal exchanged zeolite and formaldehyde interaction. The metal ions move a little bit away from the five-membered plane when HCHO adsorbs on the zeolite. This is due to the interaction of the metal with formaldehyde oxygen.

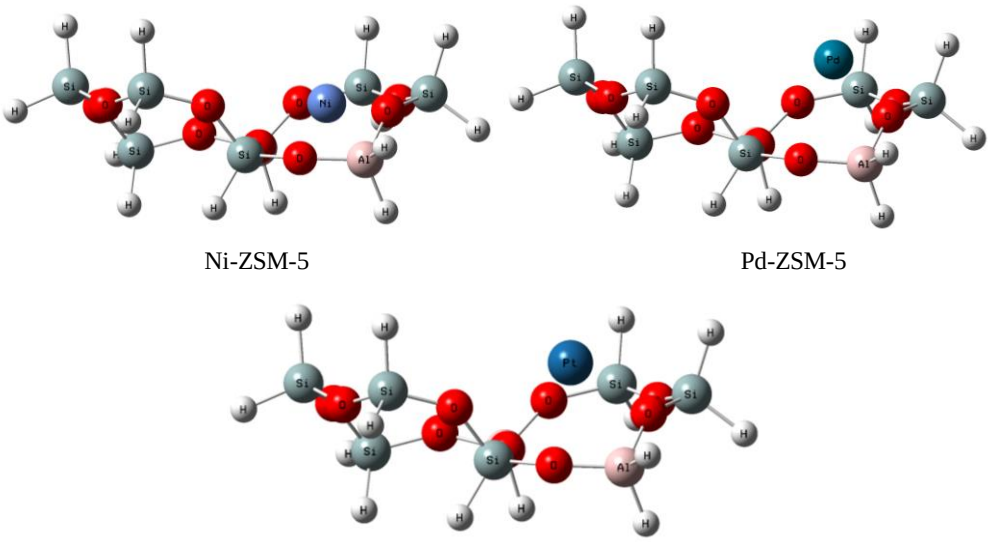

Ni-ZSM-5 Pd-ZSM-5

Pt-ZSM-5

Figure 5.1 Optimized geometries of Ni-ZSM-5, Pd-ZSM-5, and Pt-ZSM-5 catalysts

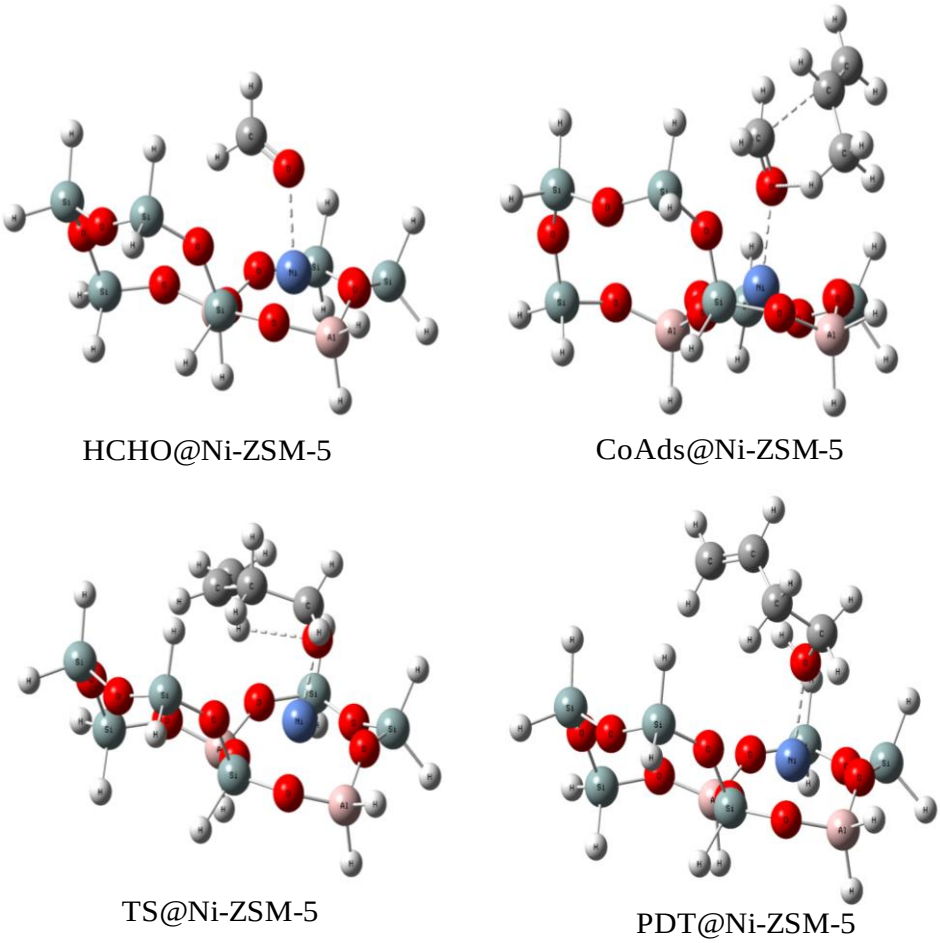

HCHO@Ni-ZSM-5 CoAds@Ni-ZSM-5

TS@Ni-ZSM-5 PDT@Ni-ZSM-5

Continue on next page ….

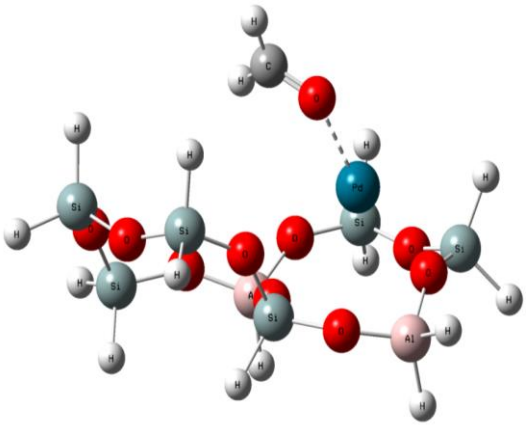

HCHO@Pd-ZSM-5

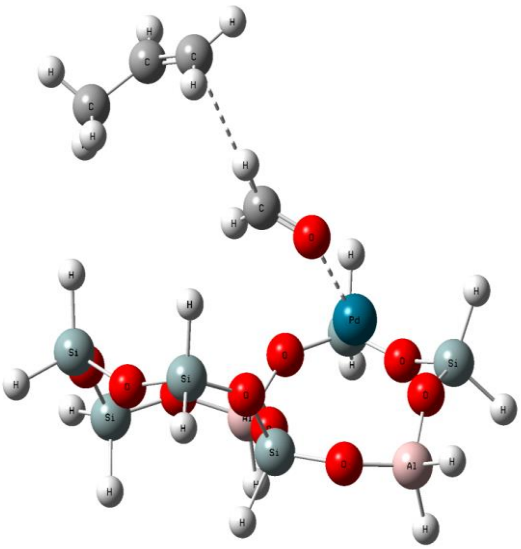

CoAds@Pd-ZSM-5

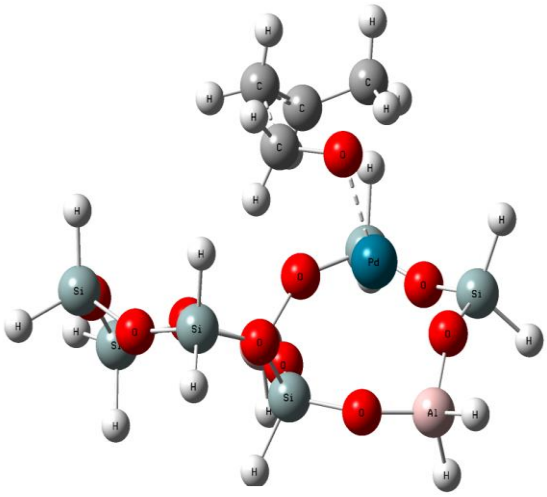

TS@Pd-ZSM-5

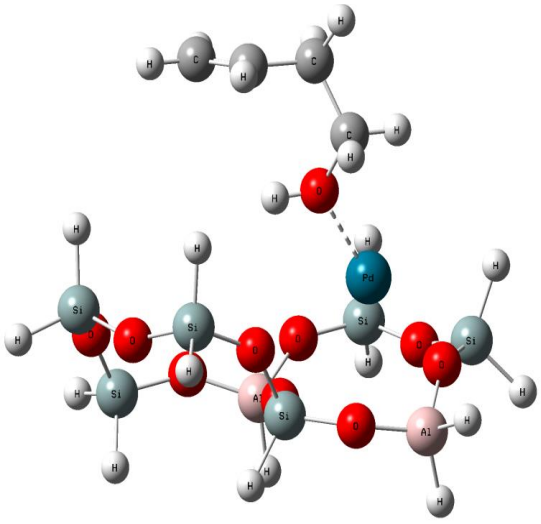

PDT@Pd-ZSM-5

Continue on next page….

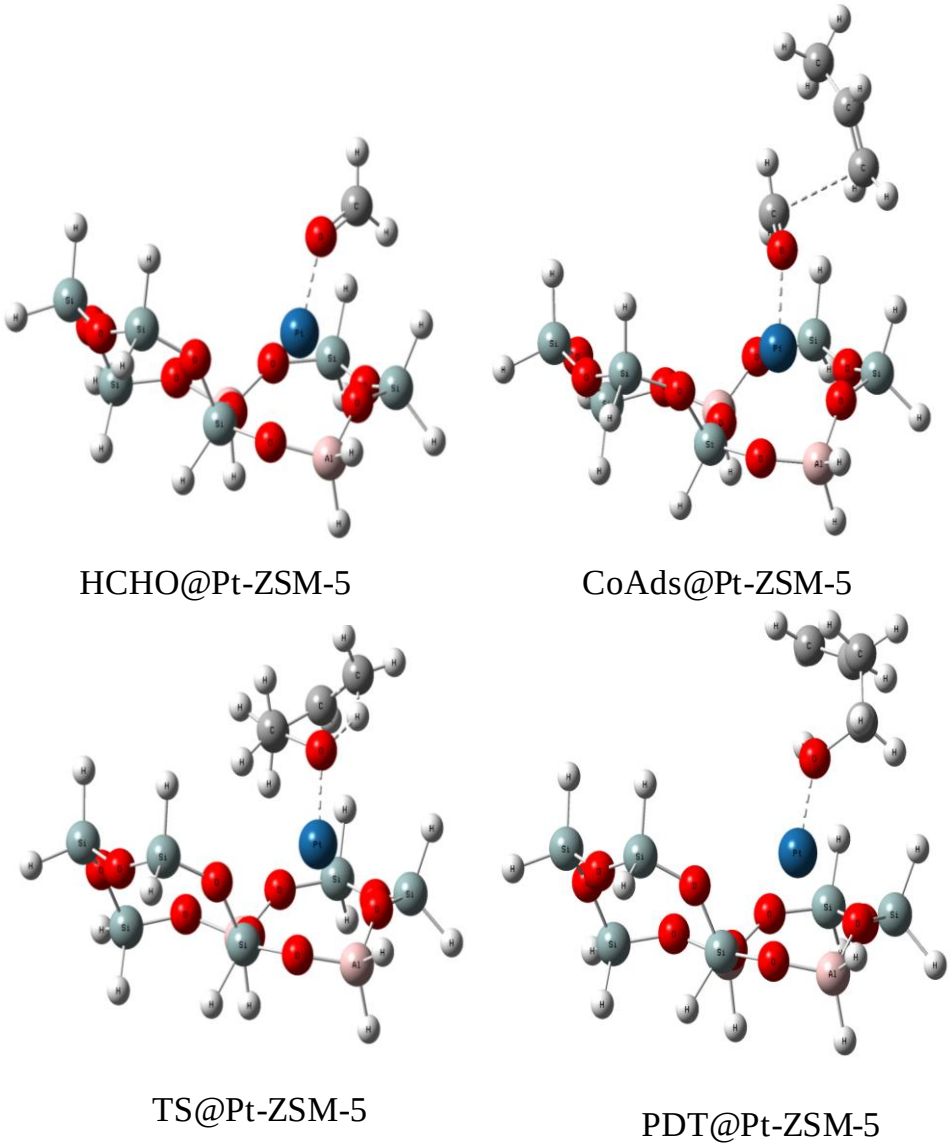

Figure 5.2 Optimized structures of the systems during the reaction

The reaction begins with formaldehyde encapsulated on the metal-ZSM-5 catalysts, to preserve formaldehyde. The C-O bond length in the formaldehyde is slightly larger than isolated formaldehyde C-O value due to the metal and the lone pair electron of carbonyl oxygen interaction. The C-O bond distance is increased by 0.041, 0.046 and 0.050 Å for Ni-, Pd-, and Pt-ZSM-5 systems, respectively. The metal cations and the zeolite binding energies were found to be -110.4, -46.9, and -55.4 kcal/mol for Ni-,Pd-, and Pt- ZSM-5 respectively. From the binding energy, the metal and the

zeolite framework charge transfer amount was revealed by the charge reduction of metals. The charge reduction follows the following order, Ni^{2+} > Pt^{2+} > Pd^{2+}. The HOMO-LUMO energy gap for M-ZSM-5 also found to be in the same order of Ni^{2+} > Pt^{2+} > Pd^{2+} shown in Figure 5.3. All optimized geometries are given in Figure 5.2.

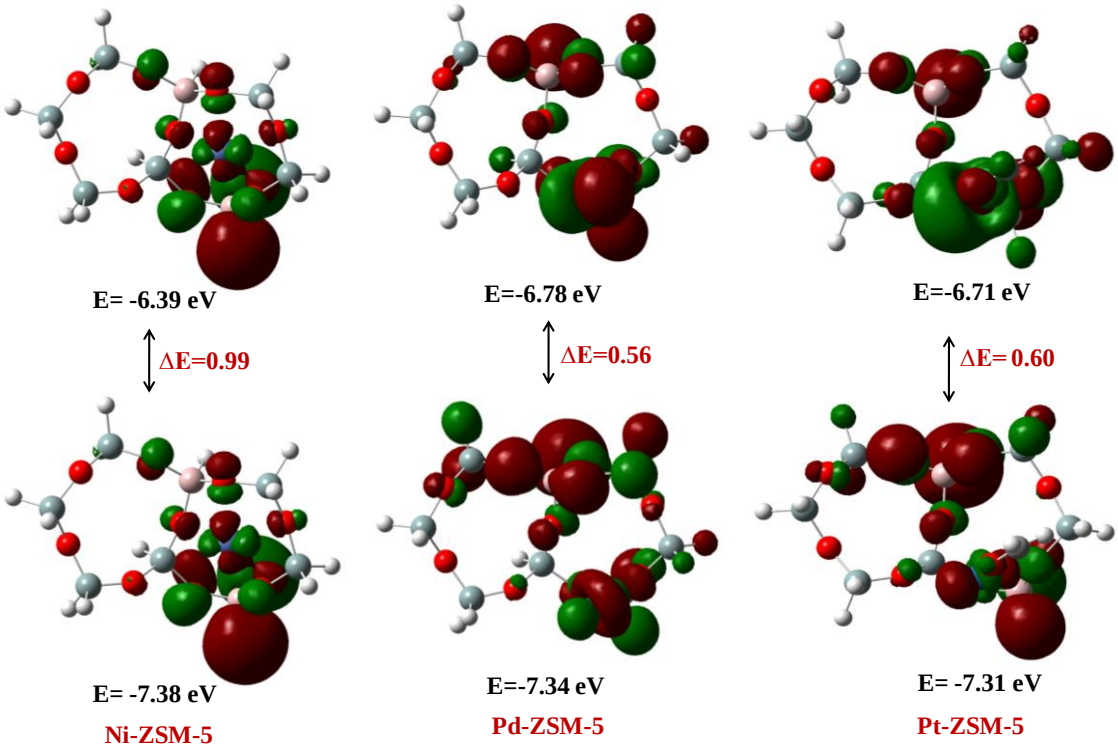

Figure 5.3 Pictorial representations of the HOMO-LUMO orbital energies of M-ZSM-5

Table 5.1 Geometrical parameters of reactants, transition state, and product of the carbonyl-ene reaction between formaldehyde encapsulated in ZSM-5 and propene

Bond Length (Å)	Isolated molecule	Formaldehyde adsorption			Co-adsorption complex			Transition state			Product		
		Ni-ZSM-5	Pd-ZSM-5	Pt-ZSM-5	Ni-ZSM-5	Pd-ZSM-5	Pt-ZSM-5	Ni-ZSM-5	Pd-ZSM-5	Pt-ZSM-5	Ni-ZSM-5	Pd-ZSM-5	Pt-ZSM-5
C-C1								1.593	1.790	1.551	1.542	1.539	1.541
C1-C2	1.333				1.355	1.352	1.358	1.476	1.421	1.484	1.517	1.516	1.519
C2-C3	1.501				1.509	1.512	1.509	1.427	1.468	1.418	1.352	1.349	1.352
C3-H3	1.094				1.098	1.099	1.095	1.173	1.126	1.229	2.632	3.044	2.526
H3-O					4.082	5.539	5.077	2.578	2.064	1.546	0.985	0.983	0.989
C-O	1.207	1.248	1.253	1.257	1.252	1.255	1.269	1.419	1.369	1.479	1.489	1.484	1.498
M-O		2.223	2.094	2.027	2.168	2.088	2.038	1.832	2.042	2.005	2.139	2.109	2.053

5.3.2 Natural Bond Orbital Analysis

Figure 5.2 shows the NBO calculations which reveal the high ionic bonding property of Pt-formaldehyde interaction. The interaction is the outcome of hybridization of 3.82% of 6s orbital corresponding to the platinum atom and 96.17% of 2p orbital corresponding to the oxygen atom with the absence of metal to formaldehyde electron back-donation. While formaldehyde was encapsulated, the total occupancies of Ni and Pd atoms were nearly unchanged, whereas Pt atom received more electrons at 6s orbital after encapsulation of formaldehyde. These observations optimize to the relativistic effect of a bulky metal atom like platinum which transforms formaldehyde molecule to become as an active electrophile in Pt-ZSM-5. As a result, the carbonyl carbon of formaldehyde attached in the Pt-ZSM-5 system favors the nucleophilic attack of propene.

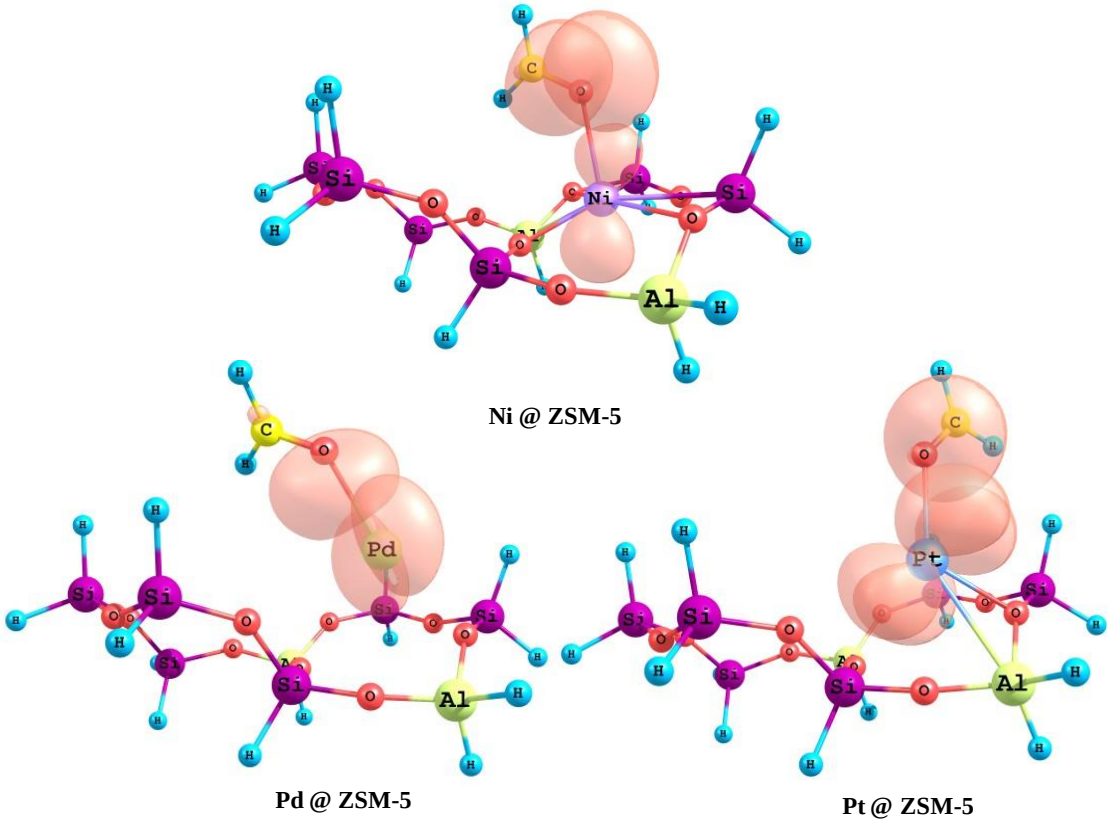

Figure 5.4 Pictorial representation of the M-O bonding character from the NBO calculations using B3LYP/LANLDZ method

The carbonyl (CO) stretch vibrational frequencies of formaldehyde and its complexes with different Ni-, Pd-, and Pt-ZSM-5 zeolites were predicted. The CO vibrational frequencies of metal/ZSM-5complexes were predicted to be 1677, 1637, and 1616 cm^{-1} for Ni-, Pd-, and Pt-ZSM-5 zeolites, respectively. For all the complexes, the carbonyl (CO) stretch vibration is redshifted by 25-86 cm^{-1} in respect to CO vibrational frequency observed at 1702 cm^{-1} in formaldehyde (Table 5.2). The frequency shifts to a lower wave number. From these evidences, it is clear that the reaction between formaldehyde and propene is physical adsorption. They just form co-adsorption complex without any bond formation.

Table 5.2 Vibrational frequencies (cm^{-1}) and frequency shift ($\Delta\upsilon_{CO}$) of the carbonyl bond of the encapsulated formaldehyde on M-ZSM-5

System	Calculated	$\Delta\upsilon_{CO}$
HCHO	1702	-
HCHO@ Ni-ZSM-5	1677	25
HCHO@ Pd-ZSM-5	1637	45
HCHO @Pt-ZSM-5	1616	86

Adsorption energies when metal cations namely Ni^{2+}, Pd^{2+} and Pt^{2+} bind to the formaldehyde molecule are -128.9, -65.6, and -93.7 kcal/mol respectively. At these energies, the corresponding bond length between the oxygen atom of formaldehyde and the metal atom is in order of Ni-O < Pt-O < Pd-O (1.96, 2.03, and 2.06 Å). Charge transfer occurs when metals are adsorbed on the zeolite framework and the amount of charge transfer between metal exchanged zeolite and formaldehyde are exhibited for the Pt-ZSM-5 which reports the highest adsorption energy. After the formaldehyde encapsulation, the reaction is followed by the co-adsorption of propene to the encapsulated complex and then by a concerted transition state.

5.3.3 Carbonyl-ene Reaction between HCHO over Metal–ZSM-5 and Propene

Co-adsorption step has two parts: first, the adsorbed formaldehyde interacts with diffusing propene via a π electron forming the co-adsorption complex with energy lower than formaldehyde adsorption. This co-adsorption complex makes some changes in the geometry. Secondly, it converts into product and M-ZSM-5 via transition state. Propene and the encapsulated formaldehyde forms a concerted transition structure in which new C-C1 and O-H bonds are formed simultaneously with a breaking of the C3-H bond. The C-O bond of formaldehyde is extended from 1.24Å to about 1.25Å for the Ni and Pd systems whereas the platinum system is slightly longer, 1.29Å. This is

compatible with the lowest activation energy of 14.8 kcal/mol, for the reaction in Pt-ZSM-5, compared to 19.3 and 16.5 kcal/mol observed in Ni- and Pd-ZSM-5, respectively. The obtained results associate well with the same reaction studied using Cu(I), Ag(I) and Au(I)-FAU catalysts reported by the researcher.[25]

We also examined the atomic charges of the molecules in the reaction by means of natural population analysis (NPA) method and partial charges are documented in Table 5.4. Table 5.3 represents the electronic configurations of all the systems. It can be seen, metal on the ZSM-5 zeolite bears the positive charge, which is compensated by the surrounding oxygen atoms. The calculated charges were found to be +0.729, +0.587, and + 0.669 e for the Ni, Pd, and Pt atoms respectively. When formaldehyde adsorbs on the metal, it is slightly changing because the formaldehyde carbonyl group dispersed the metal partial positive charge. Simultaneously, the interaction between metal and formaldehyde makes the carbonyl electron cloud deviates from the carbon atom. Thus makes formaldehyde oxygen atom more negative and carbon atom more positive. The concentration of negative charge on oxygen can stabilize the adsorption of formaldehyde. At the TS structure, the O atom becomes more negative than the charge over carbon. The increased negative charge on oxygen enhances the interaction between 3 buten-1-ol and ZSM-5. This shows the compensation between the zeolite oxygen atoms and the metal charges. The charge of the formaldehyde carbon was found to be +0.310, +0.293 and +0.323 e in the Ni, Pd and Pt-ZSM-5 system. This indicates that Pt-ZSM-5 causes the formaldehyde molecule to become an active electrophile. So that the carbon of the formaldehyde adsorbed on Pt-ZSM-5 system favours the nucleophilic attack of another molecule.

Table 5.3 Summarization of the metals electronic configuration and their total occupancy obtained from NBO calculations

Systems	**Electronic configurations**	**Total occupancy**
Ni-ZSM-5	[core]4S(0.21)3d(8.82)4p(0.24)5p(0.01)	27.27
HCHO@ Ni-ZSM-5	[core]4S(0.20)3d(8.74)4p(0.36)5p(0.01)	27.30
CoADS@ Ni-ZSM-5	[core]4S(0.20)3d(8.72)4p(0.25)5p(0.12)	27.30
TS@ Ni-ZSM-5	[core]4S(0.20)3d(8.70)4p(0.14)4d(0.01)5p(0.27)	27.30
Pd-ZSM-5	[core]5S(0.07)4d(9.30)5p(0.04)	45.41
HCHO@ Pd-ZSM-5	[core]5S(0.14)4d(9.09)5p(0.08)	45.31
CoADS@ Pd-ZSM-5	[core]5S(0.14)4d(9.09)5p(0.08)	45.31
TS@Pd-ZSM-5	[core]5S(0.15)4d(9.02)5p(0.10)6p(0.01)	45.28
Pt-ZSM-5	[core]6S(0.28)5d(8.99)6p(0.06)7p(0.01)	77.33
HCHO@ Pt-ZSM-5	[core]6S(0.38)5d(8.73)6p(0.13)6d(0.01)	77.24
CoADS@ Pt-ZSM-5	[core]6S(0.38)5d(8.74)6p(0.13)6d(0.01)	77.24
TS@ Pt-ZSM-5	[core]6S(0.49)5d(8.68)6p(0.14)6d(0.01)	77.19

Table 5.4 Partial electronic charges of the metal atom and the probe molecules

Step		**NPA - charges/e**		
		Ni-ZSM-5	**Pd-ZSM-5**	**Pt-ZSM-5**
Catalysts	Metal	0.729	0.587	0.669
Ads	C	0.310	0.293	0.323
	O	-0.562	-0.567	-0.538
	HCHO	0.095	0.103	0.169
	Metal	0.695	0.683	0.762
CoAds	C	0.311	0.302	0.289
	O	-0.592	-0.568	-0.566
	CoAds	0.078	0.118	0.141
	Metal	0.703	0.687	0.756
TS	C	-0.046	0.023	-0.075
	O	-0.703	-0.687	-0.751
	TS	0.291	0.214	0.374
	Metal	0.699	0.723	0.807

The energetic reaction profile is shown in Figure 5.5. In co-adsorption step, the co-adsorption energy for the propene bound to be encapsulated formaldehyde is increased by ~10 kcal/mol compared to the formaldehyde adsorption energies in all the cases. For carbonyl-ene reaction, it is initiated by co-adsorption of propene and the adsorbed formaldehyde at the active site of the ZSM-5 zeolite. The co-adsorption energy is lower than the formaldehyde adsorption. From Figure 5.5, it can be seen that the required higher energy barrier to generate 3 buten-1-ol from the co-adsorption complex due to an electrostatic field generated by the metal and the zeolite oxygen atoms. In step 3, the adsorbed 3 buten-1-ol product would endothermically desorbs from the zeolite active acid site, which requires 11.9 kcal/mol. The complete reaction is exothermic.

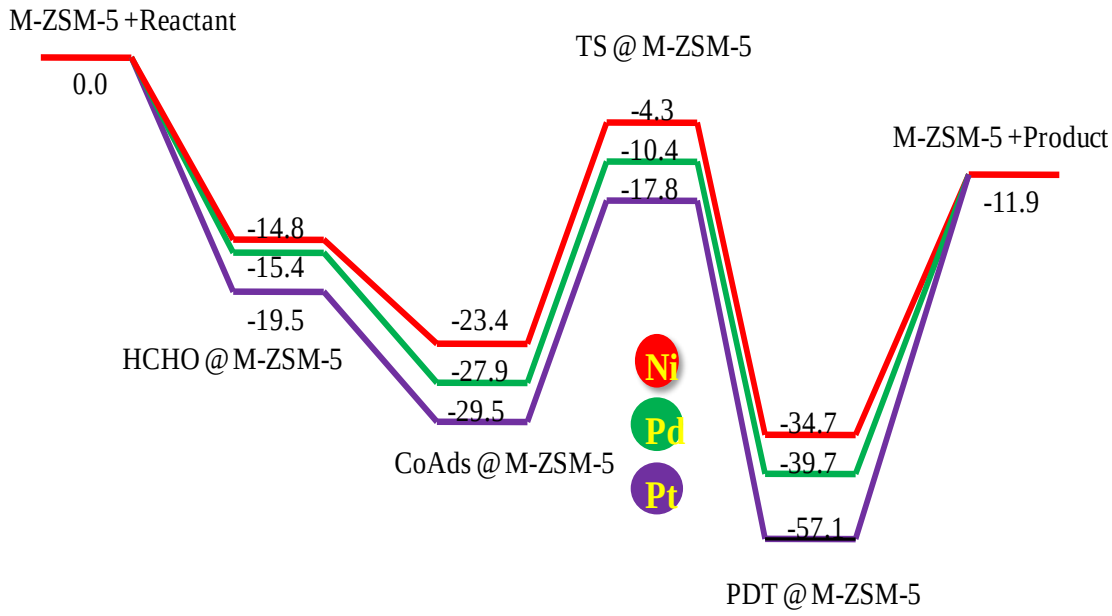

Figure 5.5 The energetic reaction profile calculated by the B3LYP/LANLDZ level of theory (all energies in kcal/mol)

5.4 Conclusion

To conclude, we have demonstrated the carbonyl-ene reaction over Ni-, Pd-, and Pt -exchanged ZSM-5 zeolites. The Pt^{2+} ion shows a high performance in the formaldehyde encapsulation process and exhibits better catalytic activity. By analyzing the electronic configuration, platinum 6s orbital plays a vital role in this high activity. It accepts an electron and induces a significant charge in the probe molecules. This inductive effect is enhanced by the zeolite framework. Although the activity of the Ni- and Pd-ZSM-5 was not as high as that of the Pt-ZSM-5, the zeolite structures are suitable for use as a catalyst for carbonyl-ene reaction. From the obtained results, platinum exchanged ZSM-5 zeolite might be a better candidate for carbonyl-ene reactions.

References

1. Angelo J.; Stork G. *J. Am. Chem. Soc*., **1974**, *96*, 7114.
2. Hajos Z.G.; Parrish D. R. *J. Org. Chem*., **1973**, *38*, 3244.
3. Lucast D. H.; Wemple J., *Synthesis*, **1976**, 724.
4. Stork G.; Isobe M. *J. Am. Chem. Soc.*, **1975**, *97*, 4745.
5. Snider B. B. In *Comprehensive Organic Synthesis*; Trost, B. M., Fleming, I., Eds.; Pergamon Press: Oxford, **1991**, ***2***, 527-561.
6. Okachi T.; Fujimoto K.; Onaka M.; *Org. Lett.,* **2002**, *4,* 1667.
7. Maruoka K.; Concepcion A. B.; Hirayama N.; Yamamoto H. *J. Am. Chem. Soc.*, **1990**, *112*, 7422.
8. Maruoka K.; Concepcion A. B.; Murase N.; Oishi M.; Hirayama N.; Yamamoto H. *J. Am. Chem. Soc.,* **1993**, *115*, 3943.
9. Hoffmann H. M. R. *Angew. Chem., Int. Ed. Engl.*, **1969**, *8*, 556–577.
10. Oppolzer W. *Angew. Chem. Int. Ed. Engl.*, **1984**, *23*, 876.
11. Oppolzer W.; Snieckus V. *Angew. Chem. Int. Ed. Engl.*, **1978**, *17*,476.
12. Vandewalle M.; De Clercq P., *Tetrahedral*, **1985**, *41*, 1767.

13. Duren T.; Sarkisov L.; Yaghi O. M.; Snurr R. Q. *Langmuir*, **2004**, *20*, 2683–2689.

14. Eddaoudi M.; Kim J.; Rosi N.; Vodak D.; Wachter J.; O'Keeffe M.; Yaghi O. M. *Science*, **2002**, *295*, 469–472.

15. Frost H.; Snurr R. Q. *J. Phys. Chem. C.*, **2007**, *111*, 18794–18803.

16. Furukawa H.; Ko N.; Go Y. B.; Aratani N.; Choi S. B.; Choi E.; Yazaydin A. O.; Snurr R. Q.; O'Keeffe M.; Kim J. *Science*, **2010**, *329*, 424–428.

17. Li H.; Eddaoudi M.; O'Keeffe M.; Yaghi O. M. *Nature*, **1999**, *402*, 276–279.

18. Rosi N. L.; Eckert J.; Eddaoudi M.; Vodak D. T.; Kim J.; O'Keeffe M.; Yaghi O. M. *Science*, **2003**, *300*, 1127–1129.

19. Rowsell J. L. C.; Yaghi O. M. *Microporous Mesoporous Mater*., **2004**, *73*, 3–14.

20. Yaghi O. M.; O'Keeffe M.; Ockwig N. W.; Chae H. K.; Eddaoudi M.; Kim J. *Nature*, **2003**, *423*, 705–714.

21. Okachi T.; Onaka M. *J. Am. Chem. Soc.*, **2004**, *126*, 2306–2307.

22. Tomita M.; Masui Y.; Onaka M. *J. Phys. Chem. Lett.*, **2010**,*1*, 652–656.

23. Sangthong W.; Probst M.; Limtrakul J. *J. Mol. Struct.*, **2005**, *748*, 119–127.

24. Choomwattana S.; Maihom T.; Khongpracha P.; Probst M.; Limtrakul J. *J. Phys. Chem. C.*, **2008**, *112*, 10855–10861.

25. Wannakao S.; Khongpracha P.; Limtrakul J. *J. Phys. Chem. A.*, **2011**, *115*, 12486–12492.

26. Frisch M.J., Gaussian 09, Revision B.01; Gaussian, Inc.: Wallingford, CT, 2010.

27. Becke A. D. *Phys. Rev.*, **1988**, *A38*, 3098.

28. Jenkins D.M.; Bernhard S. *Inorg. Chem.*, **2010**, *49*, 11297.

29. Olson D. H.; T.Kokotailo G.; Lawton S. L.; Meier W. M. *J.Chem. Phys.*, **1981**, *85*, 2238.

30. Gonzalez C., Schlegel H. B., *J. Chem. Phys.*, **1989**, *90*, 2154– 2161.

31. Schlegel H. B. *J. Comput. Chem.*, **1982**, *3*, 214–218.

32. Reed A. E.; Curtiss L. A.; Weinhold F. *Chem. Rev*., **1988**, *88*, 899–926.

33. Reed A. E.; Weinhold F. *J. Chem. Phys.*, **1983**, *78*, 4066–4073.

Summary and Conclusion

The thesis deals with density functional theory studies on zeolite encapsulated transition metal complexes. The designed complexes were tested for their possible catalytic activity towards some selective oxidative reactions. These catalysts have proved to be promising catalysts for oxidation of organic substrates. Neat complexes were optimized and their catalytic activity compared with zeolite encapsulated complexes. The work is presented in five chapters. Contents of all the chapters are briefly described as follows:

Chapter 1 deals with a brief introduction about the zeolites and their structures. The second part illustrates some of the general concepts in computational chemistry. The scope of the present investigation is described at the end of this chapter.

Chapter 2 deals with the theoretical interpretation of platinum(II)tetraammine complex encapsulated in various zeolites such as Zeolite Y, MWW and LTL and their catalytic activities were reasoned using density functional theory. The structural changes in the guest platinum(II)tetraammine complex due to the steric and electronic interactions with the host zeolite LTL, MWW and Y frameworks have been investigated using density functional theory (DFT) calculations. Geometrical parameters, HOMO and LUMO energies, global hardness and softness were calculated to understand the distortion in the pores of the zeolite matrix. The most plausible active site of the complex was identified using Fukui functions. It is observed that the square planar geometry of platinum(II)tetraammine complex has been distorted to non-planar geometry when encapsulated in supercage of zeolite framework. After encapsulating in LTL, MWW and Y zeolite, Pt-N bond lengths and bond angles vary. Among the three encapsulated complexes the LTL zeolite experienced more deviation due to the pore

size. These observations support the experimental results. The energies of the frontier orbital of the metal complexes get changed upon encapsulation, leading to a small HOMO-LUMO energy gap. The ionization potential (IP) and electron affinity (EA) values for all the complexes are calculated. The values of the ionization potential of the encapsulated complexes are less than the neat complex. This indicates that the encapsulated complexes will act as a better oxidizing agent. Evaluating the Fukui functions reactivity indexes, the platinum atom is the most prone site for the attack of both nucleophile and electrophile.

Chapter 3 describes the density functional theory studies on the neat and zeolite-encapsulated copper(II)phthalocyanine and tetra-chlorine substituted copper(II)phthalocyanine. This shows that chlorine substituted phthalocyanine complexes undergoes more distortion than unsubstituted phthalocyanine complex. The influence of encapsulation on the geometric properties of the complex is evident by the redshift of TD-DFT spectra and changes in redox properties. The TD-DFT study offers an evidence for the distortion in the encapsulated geometry of zeolite Y. It proves that the complex is effectively encapsulated into the zeolite-Y supercage, and steric hindrance in the supercages distorts the geometry of CuPc-Y and $CuPcCl_4$-Y. The change in the energies of the HOMO and LUMO has also been in agreement with TD-DFT calculations. The electrophilicity index of the encapsulated complexes shows the minimum electrophilicity and maximum hardness which leads to a higher reactivity. The chemical potential value for the encapsulated complexes is found to be greater than the neat complexes. This shows the encapsulated complexes are more actively participate in electron transfer reactions. The chemical potential value for the $CuPcCl_4$-Y is found to be higher than the CuPc-Y. This shows that $CuPcCl_4$-Y can keenly contribute in electron transfer reactions. The central copper atom of the encapsulated

complex showing a minimum Fukui function value, the zeolite framework influences the metal reactivity and enhances the hard–hard interaction. Thus, the zeolite framework influences the metal reactivity and enhances hard–hard interactions. DFT based descriptors are used for scrutinizing the reactivity of the encapsulated complexes and a mechanism of the glycidol formation is proposed based on the energetics involved in the transformation.

Chapter 4 deals with density functional theory studies on zeolite-Y encapsulated ruthenium(III)benzimidazole and 2- ethyl ruthenium(III) benzimidazole. The zeolitic framework integrity is not disturbed by the intrusion of the large guest complex. The geometry of the complexes was optimized using B3LYP hybrid functional with LanL2DZ basis set. The vibrational frequency analysis of the optimized geometry shows all real frequencies and it is confirmed that the optimized geometry corresponded to the minimum potential energy surface. The variation in the bond distances and bond angles on encapsulation is due to the influence of the zeolite framework, the topology of the supercage is expected to impose steric constraints on the complex. Upon encapsulation of the metal complexes, the energies of the frontier orbital get lifted up, leading to a small HOMO-LUMO energy gap. A blue shift in the d–d transition observed in the UV-Visible spectroscopic studies of the zeolite encapsulated complexes and they show a higher catalytic efficiency. Encapsulation in a zeolite matrix makes the metal center more viable to nucleophilic attack and favors the phenol oxidation reaction. Based on the theoretical calculations, transition states and structures of reaction intermediates involved in the catalytic cycles are derived.

Chapter 5 deals with formaldehyde-propene carbonyl-ene reaction on M-ZSM-5 zeolite (M- ZSM-5, M = Ni, Pd, and Pt) using density functional theory with the B3LYP functional. The Pt^{2+} ion shows a high performance in the formaldehyde

encapsulation process and exhibits better catalytic activity. By analyzing the electronic configuration, platinum 6s orbital plays a vital role in this high activity. It accepts an electron and induces a significant charge in the probe molecules. This inductive effect is enhanced by the zeolite framework. Although the activity of the Ni- and Pd-ZSM-5 was not as high as that of the Pt-ZSM-5, the zeolite structures are suitable for use as a catalyst for carbonyl-ene reaction. Platinum exchanged ZSM-5 zeolite might be a better candidate for carbonyl-ene reactions.

List of Publications

Publications in Journals

1. Influence of Different Zeolite Frameworks on the Geometry of Platinum(II)tetraammine Complex, Tamilmani Selvaraj and Rajalingam Renganathan, *ACS Omega* **2018**, *3*, 2558−2563.

2. Theoretical Studies of the Zeolite-Y Encapsulated Chlorine substituted Copper(II) phthalocyanine Complex on the Formation Glycidol from Allyl Alcohol, Tamilmani Selvaraj and Rajalingam Renganathan, *ACS Omega* **2018**, *3*, 9613−9619.

3. Impact of zeolite-Y framework on the geometry and reactivity of Ru (III) benzimidazole complexes – A DFT study, Tamilmani Selvaraj, Renganathan Rajalingam and Viswanathan Balasubramanian, *Applied Surface Science* **2018**, 434, 781–786.

4. Formation of 3-buten-1-ol over metal encapsulated ZSM-5 from formaldehyde and propene: A Density Functional Theory study Selvaraj Tamilmani, Rajalingam Renganathan and Balasubramanian Viswanathan, *Turkish Computational and Theoretical Chemistry*, **2018**, 2(2), 28-35.

Collaborative Papers (*not included in this thesis*)

1. A novel 2-(20 -aminophenyl)benzothiazole derivative displays ESIPT and permits selective detection of Zn^{2+} ions: experimental and theoretical studies, Subramaniyan Janakipriya, Selvaraj Tamilmani and Sathiah Thennarasu, *RSC Advances* **2016**, 6, 71496– 71500.

2. Sensitization of La modified $NaTaO_3$ with cobalt tetra phenyl porphyrin for photo
   catalytic reduction of CO_2 by water with UV–visible light, Velu Jeyalakshmi, Selvaraj Tamilmani, Rajaram Mahalakshmy, Puttaiah Bhyrappa, Konda

Ramasamy Krishnamurthy and Balasubramanian Viswanathan," *Journal of Molecular Catalysis A: Chemical*, **2016**, 420, 200–207.

3. Synthesis, Characterization, Green Catalysis & Computational Studies of a Binuclear Copper(II) Complex Encapsulated in Zeolite Y, M.G.Meera, P.Kamatchi Selvaraj, S.Tamilmani, B.Viswanathan, *International Journal of Advanced Chemical Science and Applications*, **2014**, Volume -2, Issue -2.

4. TiO_2 sensitized by copper complexes as possible catalysts for the photocatalytic reduction of CO_2 and Water, S.Tamilmani, R.Renganathan and B.Viswanathan, *Bulletin of the Catalysis Society of India*, **2013**, 1-2.

List of Papers Presented in National and International Conferences

1. Neat and Zeolite Y encapsulated Cu(II), Zn(II) and Ru(III) complexes containing Imidazole ligands as Catalysts: Structure and Reactivity – A DFT Study, 22nd National Symposium on Catalysis, CSIR-Central Salt & Marine Chemicals Research Institute, Bhavnagar, Gujarat, January 7-9, 2015.

2. DFT studies on Neat and Zeolite Y encapsulated Cu (II) Benzimidazole Complexes, National Conference on Green Chemistry and Sustainable Environment (GCSE-2016), B.S. Abdur Rahman University, Chennai, August 2-3, 2016.

3. Adsorption and Mechanism of an Anionic dye Methyl Orange on $Sr_3Ti_2O_7$/ MMT Composite: A theoretical approach, Fourth International Conference on Advanced Oxidation Processes (AOP-2016), BITS Pilani, K K Birla Goa Campus, December 17-20, 2016.

4. Influence of Zeolite Framework on the Structure, Properties and Reactivity of Ru (III) Benzimidazole Complexes – A Computational Study, 7^{th} Asia-Pacific Congress on Catalysis (APCAT-7), The Lalit Mumbai, Mumbai, January 17-21, 2017.

5. A DFT Approach to the Rapid Transformation of Formaldehyde to But-4-enol via Carbonyl-ene Reaction over Metal Encapsulated ZSM-5 Framework, 23^{rd} National Symposium on Catalysis, Royal Orchid Yelhanka, Bengaluru, January 17-19, 2018.